Order Number 9322435

Investigation of the striation formation in the course of abrasive waterjet cutting

Chao, Jo-fei, Ph.D.

New Jersey Institute of Technology, 1993

U·M·I
300 N. Zeeb Rd.
Ann Arbor, MI 48106

INVESTIGATION OF THE STRIATION FORMATION IN THE COURSE OF ABRASIVE WATERJET CUTTING

by
Jo-fei Chao

A Dissertation
Submitted to the Faculty of
New Jersey Institute of Technology
in Partial Fulfillment of the Requirements for the Degree of
Doctor of Philosophy

Department of Mechanical and Industrial Engineering

January, 1993

APPROVAL PAGE

Investigation of the Striation Formation in the Course of Abrasive Waterjet Cutting

Jo-fei Chao

Dr. Ernest S. Geskin, Dissertation Advisor
Professor of Mechanical Engineering
Department of Mechanical and Industrial Engineering
New Jersey Institute of Technology

Dr. Eugene Gordon, Committee Member
Distinguished Professor of Electrical Engineering
Department of Electrical Engineering
New Jersey Institute of Technology

Dr. Harry Herman, Committee Member
Graduate Advisor and Professor of Mechanical Engineering
Department of Mechanical and Industrial Engineering
New Jersey Institute of Technology

Dr. Ming C. Leu, Committee Member
Professor of Mechanical Engineering
Department of Mechanical and Industrial Engineering
New Jersey Institute of Technology

Dr. Nouri Levy, Committee Member
Associate Professor of Mechanical Engineering
Department of Mechanical and Industrial Engineering
New Jersey Institute of Technology

ABSTRACT

Investigation of the Striation Formation in the Course of Abrasive Waterjet Cutting

by
Jo-fei Chao

The principal defect of the surfaces generated by abrasive waterjet machining is excessive waviness (striation). The existing theories of striation formation are not adequate to explain this phenomenon. The presented study is concerned with the development of an understanding of the mechanism of striation formation.

A spectral analysis of temporal process and spatial surface characteristics demonstrated that the striation is caused by nozzle vibration that is due to the conditions of the motion control of the nozzle. This enabled us to discover a means for improving the surface finish. From a study of the surface spectra, it was found that the amplitudes of the striation marks could be expressed as a second degree polynomial function of the distance from the top of the workpiece.

The effects of the jet pressure, cutting speed, and workpiece material on the surface topography were also investigated. The acquired information was used to construct a model for the simulation of surface topography.

BIOGRAPHICAL SKETCH

Author : Jo-fei Chao

Degree : Doctor of Philosophy in Mechanical Engineering

Date : January, 1993

Undergraduate and Graduate Education:

- Doctor of Philosophy in Mechanical Engineering
  New Jersey Institute of Technology, Newark, New Jersey, 1993

- Master of Science in Mechanical Engineering
  National Central University, Chung-li, Taiwan, R.O.C., 1987

- Bachelor of Science in Mechanical Engineering
  National Chung-hsing University, Taichung, Taiwan, R.O.C., 1982

Major : Mechanical Engineering

Presentations and Publications :

Chao, J. "Optimum Design of the Engine Mounting System." Master Thesis, National Central University, Chung-li, Taiwan, R.O.C., 1987.

Chao, J., E. Geskin, and Y. Chung, "Investigations of the Dynamics of the Surface Topography Formation During Abrasive Waterjet Machining." *Proceedings of the 11th. Int. Symp. on Jet Cutting Technology*, London, England, 1992.

Zhou, G., M. Leu, E. Geskin, Y. Chung, and J. Chao, "Investigation of Topography of Waterjet Generated Surfaces." *Proceedings of 1992 ASME Winter Annual Meeting*, LA, November 1992.

Chao, J., G. Zhou, M. Leu, and E. Geskin, "Characteristics of Abrasive Waterjet Generated Surfaces and Effects of Cutting Parameters and Structure Vibration." Submitted to AMSE Journal of Engineering for Industry.

Chao, J., and E. Geskin, "Experimental Study of the Striation Formation and Spectral Analysis of the Abrasive Waterjet Generated Surfaces." Submitted to the 7th. American Water Jet Technology Conference, Seattle, Washington, 1993.

Chao, J., E. Geskin, and M. Leu, "The Effect of Robotic Traverse System Dynamics on the Surface Generated by Abrasive Waterjet." Submitted to 9th. International Conference on CAD/CAM Robotics and Fractories of the Future, New Jersey, 1993.

This dissertation is dedicated to
my family

ACKNOWLEDGMENT

The author wishes to express his sincere gratitude to his advisor, Professor Ernest S. Geskin, for his guidance, constant encouragement, and patience throughout this investigation.

The author also wishes to thank Dr. M. Leu for his help and provided lots of valuable suggestions during this work. Thanks are also due to Dr. H. Herman for his continued support and friendship. Special thanks to Dr. Gordon, and Dr. Levy for serving as members of the committee. The author are also thankful to Dr. Dave for his interest in this study.

The author appreciates the timely help and suggestions from all the Waterjet Laboratory members. The author would also like to acknowledge the moral support and suggestions of this work of my very good friend, Dr. Y. Chung.

Finally, a grateful thank you to the author's wife, Chiu-ling, and parents for their firm support and encouragement.

TABLE OF CONTENTS

Chapter **Page**

LIST OF TABLES

Table **Page**

LIST OF FIGURES

Figure **Page**

Figure **Page**

Figure **Page**

Figure **Page**

LIST OF SYMBOLS

α	angle of attack
σ	material flow stress
σ_W	variance of white noise
ε	specific energy for the deformation wear mode
ϕ_p	parameter of auto-regressive model
ρ_p	density of the abrasive particle
θ_q	parameter of moving-average model
$\hat{\gamma}(k)$	auto-covariance function at lag k
δv	volume removal rate by a single particle
$\eta(z)$	decreasing function
b_k	coefficient of polynomial
C_K	characteristic velocity
d_m	carbide tube diameter
D_j	jet diameter
e_k	kinetic energy of a single particle
f_c	cut-off frequency
F	traverse rate
$G_x(f)$	auto-spectral density function of the input
$G_y(f)$	auto-spectral density function of the output
h	depth of jet penetration
h_c	depth of cutting wear mode
$h(\tau)$	dynamic characteristic of constant parameter linear system
$H(f)$	frequency response of system
K	degree of polynomial
M_a	abrasive mass flow rate
N	number of sampled data

R_f	roundness coefficient
R_j	jet radius
$R_x(\tau)$	auto-correlation function of input
$u(t)$	sampled data set
$\{u_n\}$	recorded data set
V_0	initial particle velocity
V_y	sideways velocity
$x(t)$	arbitrary input
X_t	sampled data at the instance of time t
$y(t)$	output from constant parameter linear system

CHAPTER 1

INTRODUCTION

Abrasive waterjet (AWJ) machining is a relatively new manufacturing technique. Due to acceptable cutting speed, absence of a heat-affected zone and thermal distortion, and the ability to cut all materials of interest, AWJ is widely used in a number of industrial applications. AWJ has the potential of becoming one of the principal material removal technologies, however, several shortcomings substantially inhibit the use of this technology.

One of the principal deficiencies of AWJ is excessive waviness (striation) of generated side wall surfaces. Usually, the side wall surface generated by AWJ consists of a smooth upper and a wavy bottom zone [1, 2]. The upper smooth zone has a random, moderately isotropic texture, with a height distribution that is nearly Gaussian. The surface quality in this zone is comparable to the quality generated using milling and turning techniques [3]. The depth of the upper zone depends on the specific energy delivered by the jet per unit of workpiece area. Reductions of the cutting speed or increase of the jet velocity results in deepening of the smooth zone. A desirable surface finish can be obtained if the thickness of the workpiece is less than the depth of the smooth zone, otherwise additional finishing operations are required [4, 5]. Obviously, striation phenomenon substantially reduces practical application of AWJ technology and minimization of this problem would constitute a substantial improvement in material shaping.

Striation formation is a phenomenon typical of all existing high energy beam technologies. The general pattern observed on surfaces generated during laser, plasma, and flame cutting is similar to that generated by AWJ. Despite the importance of elimination or minimization of this phenomenon, the knowledge of the mechanism

of striation formation is inadequate. There is no unquestioned general physical theory of this phenomenon. Instead, there are several insufficiently substantiated hypotheses pertinent to various particular cases. Most important, there is no evident solution.

For example, the current explanation of AWJ generated striation is based on the experiment of Hashish [6, 7], involving visualization of AWJ cutting of transparent materials. In this experiment, the author attempted to demonstrate the existence of two modes of jet-workpiece interaction, as well as the periodic character of this interaction. Thus, striation appears at the portion of a workpiece below the level of the transition between the two modes. Using this observation, Hashish suggested that the cause of striation is the change of the mode of material destruction. He also presented a detailed theory based on this hypothesis. This theory was accepted by most of the waterjet research community, and used for an explanation of the factors pertinent to striation formation. A mathematical model of the striation formation based on the Hashish hypothesis was presented by Tan [8].

From Hashish's experiment, it follows that striation is an intrinsic feature of AWJ machining and thus its elimination appears to be impossible. This conclusion is shared by the community of waterjet researchers. Little additional study is being reported and the technology appears to be encumbered by this important practical limitation.

More recently, Hashish [9] hypothesized that striation can be caused by changing operational conditions during cutting. These conditions include water pressure, abrasive flow rate, and traverse rate. During the early phase of our experiments we observed other conditions that influence the formation of striations. For example, the direction of cutting dramatically changes the striation pattern. It was also found that the entire kerf geometry has a periodic character. This observation together with the general formation of striation with all beam machining techniques enabled us to suggest that motion control and robot vibration might contribute at least partially to the striation formation.

This hypothesis formed the basis for the work in this study. In the experiments to be described, we studied the dynamic motion of the cutting head, water pressure variation, and different materials, and attempted to correlate with the observed striation. The study of the robot dynamics showed that the vibration in the nozzle guidance system is the main cause of the normally observed striation formation. This information makes imperative the development of means for vibration reduction, which would lead to suppression of striations, or at least greatly extend the depth of the smooth zone.

In the dissertation that follows, we describe the investigation technique developed to prove the hypothesis as well as the results of its application. In Chapter 2, previous studies of the striation phenomena in laser and AWJ cutting are discussed. The material in this chapter includes also preliminary observations which have been used for the design of the experimental procedure. The experimental setup and methods used for the study of the striation formation are presented in Chapter 3. The application of a routine signal processing procedure suitable for the studies of the cutting head vibration spectrum to the examination of conditions is discussed in Chapter 4. The results of the experimental study are presented in Chapter 5. The use of the resulting information for process modeling is discussed in Chapter 6. Finally, recommended process improvements are given in Chapter 7.

CHAPTER 2

PHENOMENA OF THE STRIATION MARKS IN HIGH ENERGY BEAM CUTTING

The formation of striation marks on the kerf edge are a common feature of all high energy beam techniques, including laser gas, flame, waterjet (WJ) and abrasive waterjet cutting. These techniques are based on different mechanisms of material removal. For example, laser gas machining utilizes the energy of the coherent beams of monochromatic lights to melt, vaporize, or thermally modify materials, while AWJ machining uses a high pressure abrasive waterjet to erode the target material. Nevertheless, a similar striation phenomenon is observed in all of these processes. The striation formation in the course of laser gas cutting has been the subject of a number of comprehensive and detailed studies. The similarity between the waviness of the laser and AWJ generated surfaces enables one to utilize the data acquired in these studies in the analysis of the AWJ machining. This chapter is concerned with such an analysis.

2.1 Laser Gas Cutting

The dynamics of laser gas cutting was investigated by Arata et al. [10] in 1979. Two continuous wave CO_2 lasers were used in this study. In order to acquire the information about the appearance of the cuts, high speed color films of the cutting were obtained, power density distribution of the focused laser beam, and temperature distribution at the cutting front were recorded. It was found that at low cutting speed the rate of the oxidation reaction (self-burning) is higher than the cutting rate and self-burning results in the generation of irregularly spaced holes with a diameter much larger than the beam spot size. It was suggested that this results in the periodic

change cutting of the pattern. At a higher cutting speed, the cutting phenomenon becomes steady and a high power beam elevates the temperature at the beam-workpiece interface so that a high rate of material removal is achieved.

Powell et al. [11] proposed the use of laser pulsing to improve the cut edge quality. A continuous wave CO_2 laser was used in a pulsed output mode. The range of the laser pulse repetition frequency (PRF) was chosen to be between 100 and 1000 Hz because the observed "natural striation frequency" (calculated from the speed of cutting and the wavelength of striation produced during continuous wave cutting) was approximately 250 Hz. In the high PRF range (800 to 1000 Hz), the surface profile shows a striation frequency slightly higher than the "natural striation frequency". It appears that the material being cut responds to the incident energy as if it were a continuous input. In the intermediate frequency range (400 to 700 Hz), the striation frequency is determined by the laser pulse frequency. At the low end of the frequency range, the striation frequency is also dominated by the laser pulse frequency and may cause an unacceptable surface finish.

The experiments reported in [12] showed that similar striation marks occur on thin plates and at the top of the cut edge on thick plates. For thick plates, the striation frequency generated at the bottom of the cut has a close correlation to the natural striation frequency.

A theoretical analysis of the laser cutting process based upon experimental work were reported by Olsen [13]. The balance of thermal energy and the balance of momentum for a finite element of the melt surface were used in order to examine the factors that can cause oscillation in the melt surface, such as gas flow and friction in-between the gas and melt, fluctuations in laser beam intensity distribution, fluctuations in cutting gas flow as well as the vibrations of the positioning system. These correlation between the oscillations in the melt front propagation and striation was investigated.

The studies above show that pulsation of the energy supply as well as the way of beam guiding are the primary sources of the striation formation in the course of laser cutting.

2.2 Striation Phenomena in Abrasive Waterjet Cutting

Mechanisms of the material removal by AWJ and laser are quite different, however, the similarity in striation pattern enables us to expect the similarity in the striation formation. We can seek the cause of AWJ generated striation in the peculiarity of energy supply and vibration of the positioning system. Similar to the fluctuations of the laser beam power, the fluctuation in the jet pressure and the abrasive flow rate determined the variation of the jet energy. It is also expected that the vibration of the positioning system is one of the factors effecting the surface topography. The understanding of the material removal by AWJ is necessary for identification and comparative evaluation of various causes of striation formation.

2.2.1 Erosion by Solid Particles

AWJ machining is mainly due to the material erosion by the impinging particles. The theory of erosion was introduced by Finnie [14] in 1958; who explained many aspects of the erosion of ductile materials under the action of particle stream. It is assumed in the theory that the particles, impinging upon a smooth surface at an angle of attack α will cut into the surface like a sharp tool. Three equations of motion according to Newton's law are used to describe the trajectory of an individual particle during cutting. Then the volume removal is calculated by integrating of the contact area along the particle trajectory over the period of impact. The theoretical results strongly correlated with experimental data for ductile materials at shallow angles of attack, but are almost irrelevant for erosion under normal attack on the same material. The plot relating the volume removal to the angle of attack is shown in Figure 2.1.

Bitter [15, 16] carried out a theoretical study of particle erosion. In his work, the erosion analyzed by Finnie is classified as cutting wear which is accompanied by plastic deformation of the surface material. The erosion by particles under conditions of normal attack on ductile materials is classified as deformation wear. This phenomenon was not accounted for in Finnie's analysis. Bitter's approach is based on the computation of the plastic energy dissipation from the impact parameters of a single erosive particle. The wear is defined as the amount of energy needed to remove a unit volume of material. The total volume removal W_t is the superposition of the volume removal by cutting wear W_c and deformation wear W_d. The results show good agreement with the experimental measurements for both ductile and brittle materials. A plot relating volume removal with the angle of attack is shown in Figure 2.2.

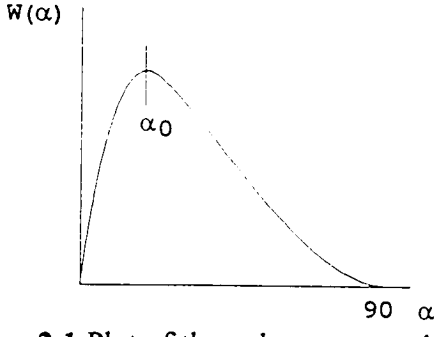

Figure 2.1 Plot of the volume removal w(α) of ductile material versus the angle of attack α.

All other works on the erosion theory are basically extended from Finnie's and Bitter's work. In the following section, the previous studies on the striation formation during AWJ cutting are explained using the theory of erosion.

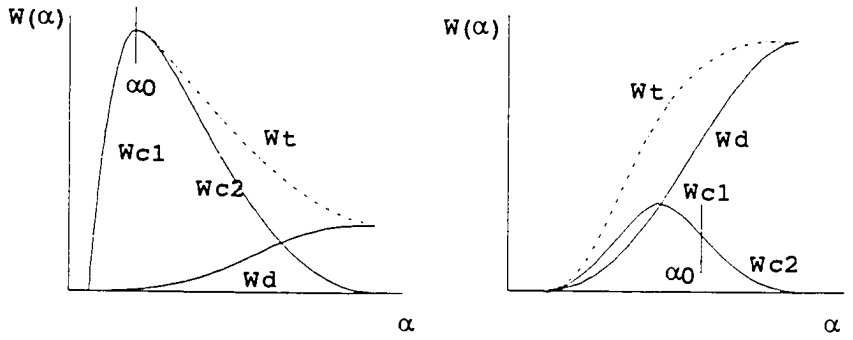

Figure 2.2 Total volume removal *Wt* versus the angle of attack α of (a) ductile material and (b) brittle material.

2.2.2 Previous Study of Striation Phenomena During AWJ Machining

The Striation phenomenon has been studied by Hashish since 1984 [6, 7]. Several experiments had been carried out by the use of a high speed movie camera recording the non-through cutting of transparent materials. According to his observation, Hashish suggested that the erosion mode changes as the jet penetrates during the cutting and that this change causes the striation marks at the bottom part of the kerf edge, as in the surface shown in the Figure 2.3. The upper portion of the kerf edge is generated by the particles impacting the workpiece at a shallow angle which is the *cutting wear mode*. In this zone the cutting process is a steady-state process. Because the material removal rate decreases as the depth of penetration increases, the jet-workpiece interface starts to bend and the steady-state process terminates at the depth of h_c [17, 18] (h_c is the range of the cutting wear mode from the top of the kerf and it can be roughly determined by the depth of the uncut material in the exit cutting stage). The value of h_c is given as follows:

$$\frac{h_c}{d_j} = \frac{C}{2.5}\left(\frac{14\dot{m}}{\pi\rho_p u d_j^2}\right)^{2/5}\left(\frac{V_0}{C_K}\right) \qquad (2.1)$$

where

d_j is the jet diameter.

C is a fraction to account for the case when the cutting wear mode terminates with only partial involvement of the total jet diameter.

$\dot{m}$ is the abrasive mass flow rate.

ρ_p is the density of the abrasive particle. (3.4-4.3)

V_0 is the initial particle velocity.

C_K is characteristic velocity defined by $\sqrt{\frac{3\sigma R_f^{3/5}}{\rho_p}}$

σ is material flow stress.

R_f is the ratio of the abrasive particle corner's average diameter to the diameter of the inscribed circle. (For #80 garnet R_f is 0.4.)

At the depth h_c, the curvature of the jet-workpiece interface changes abruptly. The jet attack angle increases so that the erosion becomes dominated by the *deformation wear mode*. As the penetration depth increases, significant striation marks start to develop due to the way a particle impacts the workpiece at a large angle of attack, in the mean time the jet effective diameter changes. This means that the striation starts to develop from the depth of h_c until the maximum depth of cut. The whole cutting process is cyclic in nature. Every cutting cycle corresponds to a traverse distance that equals to the effective jet diameter. The frequency of the striation marks is equal to F / D_j, where F is the traverse rate, D_j is the jet diameter, because each cutting cycle corresponds to the traverse distance of the jet diameter. This kind of striation caused by the erosion mode changes along the jet penetration direction is called *jet induced waviness*.

In the later work [9], Hashish suggested that the striation marks that appear at the top of the kerf edge are induced by the traverse system, so called the *traverse*

induced waviness. He also suggested that the waviness could also be caused by the variation of the jet pressure, abrasive flow rate and the traverse rate. The relationships among the traverse rate, abrasive flow rate, and the surface waviness were presented. Hashish also pointed out that the cross vibration has a critical effect. These factors, however, have relatively small effects on the surface waviness of hard-to-machine materials. For these materials the *jet induced waviness* is paramount.

Tan [8] proposed a theoretical model to describe the striated surface formation based on the kinematics and geometry of the cutting process rather than any dynamic factors of the process. The assumption used for model construction was based on the observations of Hashish's visualization experiment [7]. Two first-order differential equations were derived to describe the cutting process, as follows :

$$\frac{dh}{dt} = f(h) \tag{2.2}$$

$$\frac{dD_j}{dt} = f(D_j, h, F) \tag{2.3}$$

where the h is the depth of penetration, D_j is the effective cutting diameter of the jet (i.e. the kerf width at the depth of h) and F is the traverse rate. The first equation expressed the energy dissipation during the jet penetration. The penetration rate decreases as the depth of cut increases. The second equation represents the relations among the effective jet diameter, depth of penetration and the cutting parameters. This equation was derived on the basis of the peculiarities of the bottom kerf geometry. At the depth h, the effective jet diameter D_j increases as the traverse velocity decreases. The jet diameter varies cyclically along the traverse direction from 0 to Dm (the maximum effective jet diameter). These assumptions were made in accordance with the discontinuous phenomenon at the bottom kerf width and the visualization experiment given in [7].

In [19], a physical model for describing the striation phenomenon was proposed. This model shows good *qualitative* agreement with the experimental results. The geometry at the bottom of the cut and the volume removal caused by the deformation wear were the two major factors in this model. The model is as follows:

$$\frac{2R_w}{d_m} = 1 - \sqrt{1 - (\pi/4)^2 \left[\frac{u d_m (h - h_c)\varepsilon}{0.5 m_a V_a^2} \right]^2} \qquad (2.4)$$

where ε is the specific energy for the deformation wear mode, d_m is the carbide tube diameter, h is the penetration depth.

A new experimental result pictorially represented the effect of the operating pressure on the surface striation. The fluctuation of the jet pressure, however, constitutes 20% to 25% of the mean operating pressure. Such fluctuation is not a normal cutting condition.

2.2.3 Summary of Previous Results

The description of the striation formation given in the previous works can be summarized as follows:

1. At the upper portion of the kerf edge, the cutting process is dominated by the cutting wear mode until the depth of h_c is reached .
2. Every cutting cycle corresponds to a traverse distance that equals the jet diameter and the mathematical expression is u / d_j.
3. The jet induced waviness is periodic in space.
4. A model of the surface waviness as shown in Equation 2.4.

2.3 Experiment Observations

The typical striation marks generated by the AWJ are shown in Figures 2.3 - 2.4. In Figure 2.3, the upper portion of the kerf edge shows a fairly smooth surface. Only a few striation marks can be observed and their amplitude very small. With increase in penetration depth, the amplitude of the striation marks increases and severe striation marks dominate at the lower portion of the kerf edge. The spaces between the marks and the amplitudes of the marks are quite random. We can roughly classify these two zones as the *smooth zone* and the *striated zone* [1, 2, 20, 21, 3]. In Figure 2.4, the striation marks can be observed in all regions of the surface. The striation marks show more regular and larger amplitude than the striation marks shown in Figure 2.3. The only difference between two samples shown in the Figures 2.3 and 2.4 is that the samples were cut in the perpendicular direction of the same waterjet cutting system. All other cutting parameters are identical.

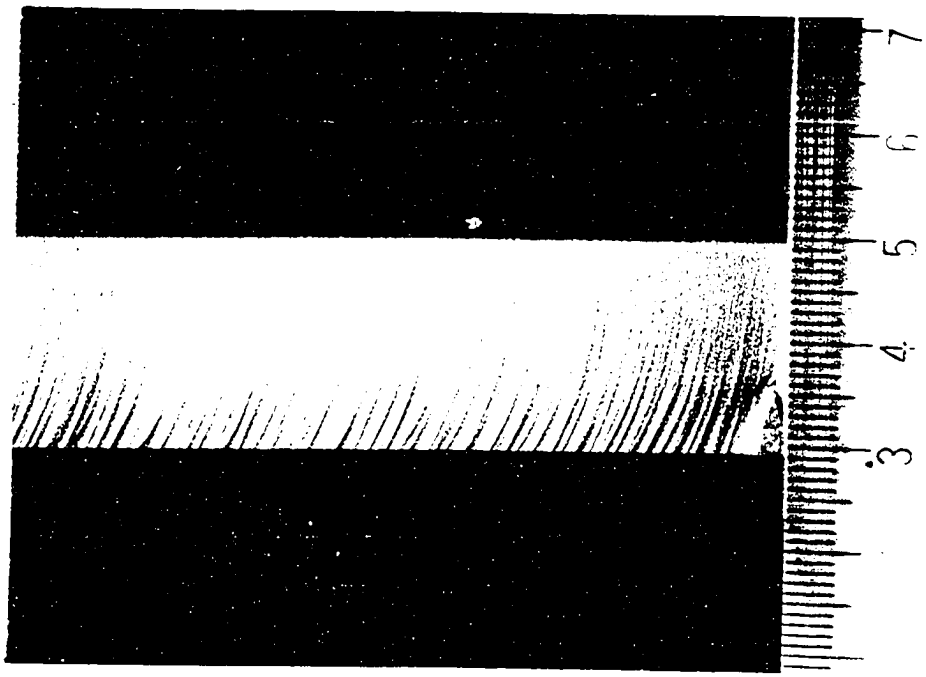

Figure 2.3 Surface generated by cutting a titanium sample in X-direction of the 5-axis machine.

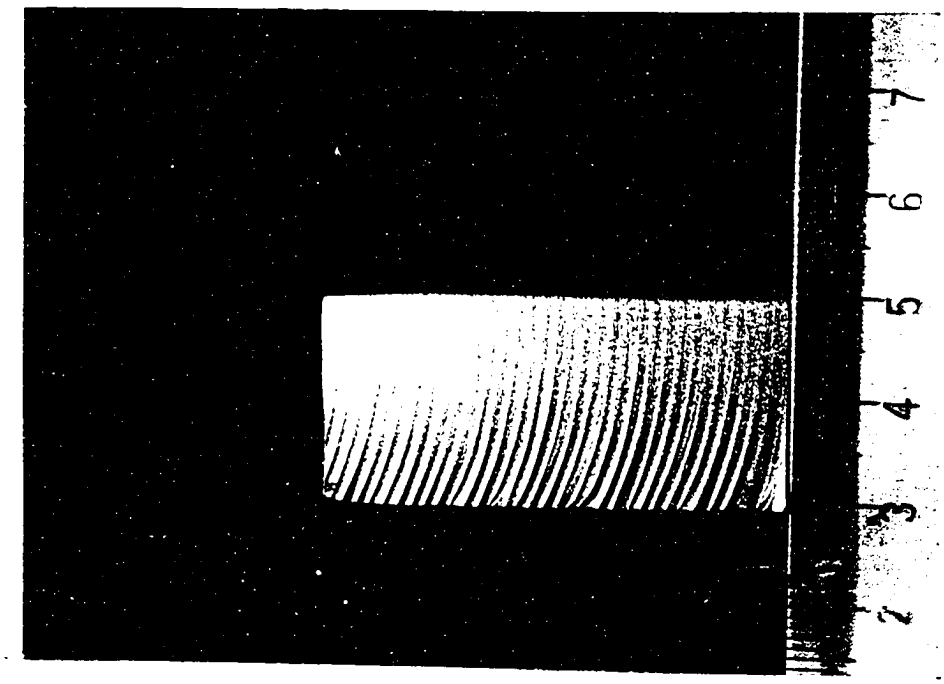

Figure 2.4 Surface generated by cutting titanium sample in Y-direction of the 5-axis machine.

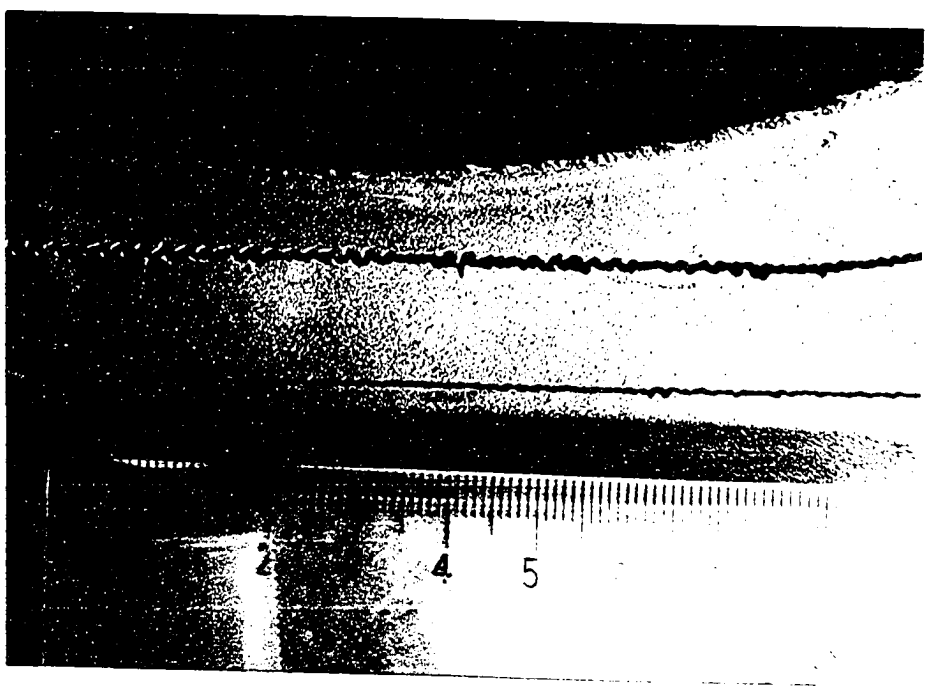

Figure 2.5 Saw-like kerfs at the bottom of the titanium plate generated at different cutting speeds.

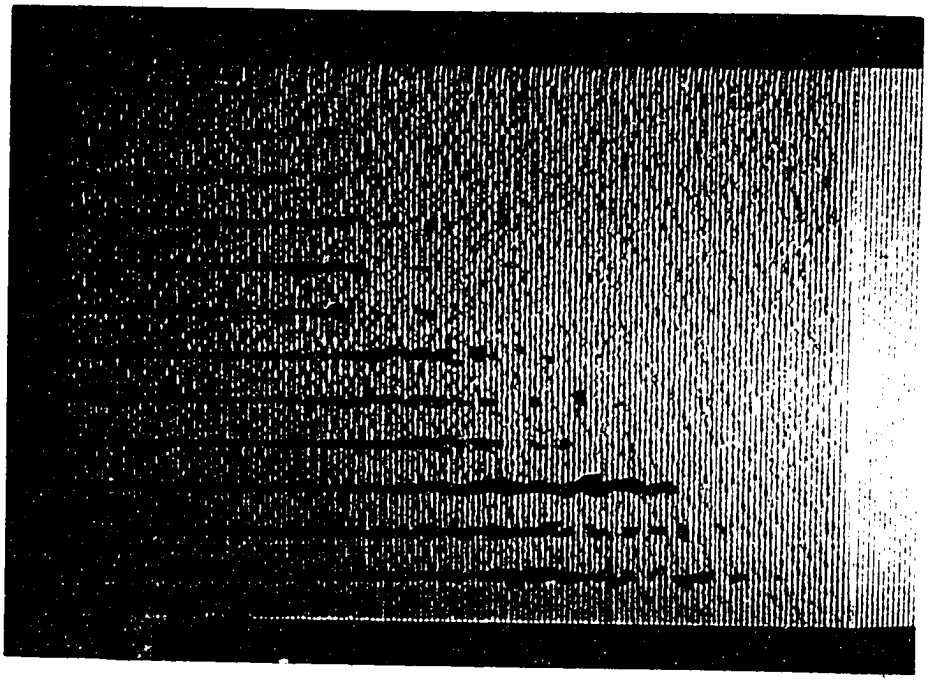

Figure 2.6 Discontinuous holes at the bottom of cut.

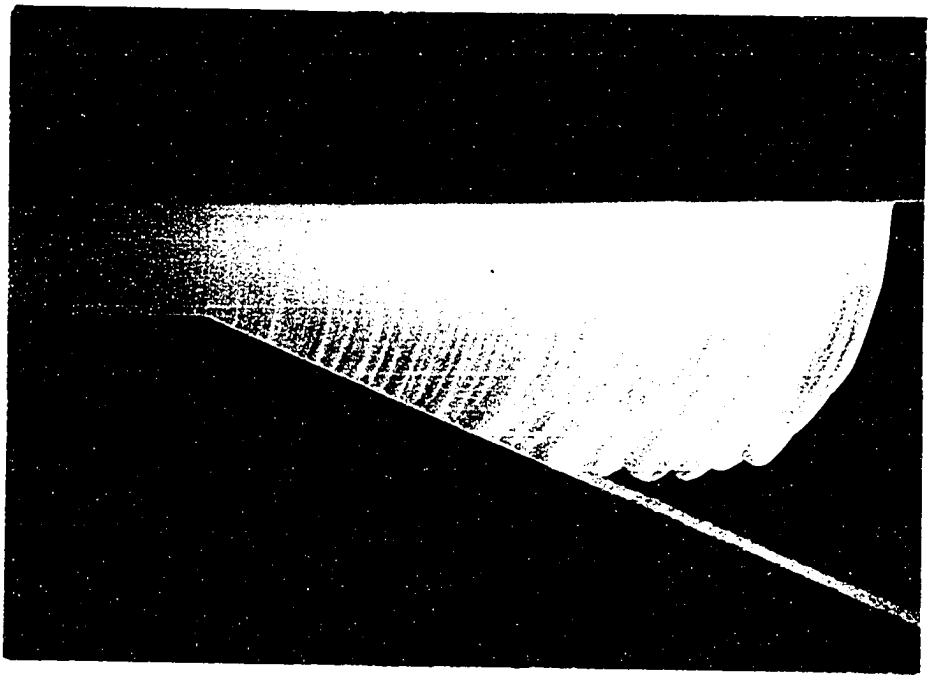

Figure 2.7 Striation marks of a glass sample.

Figure 2.5 shows the saw-like bottom surfaces of the kerfs generated at different cutting speeds. The upper ones used a slower cutting speed than the lower one. The amplitude of the striation on the upper kerf can be seen as much larger than the amplitude on the lower kerf. Figure 2.6 shows the discontinuous holes at the bottom of the workpiece. This only happens at the critical cutting conditions when the cutting speed is too high or the abrasive flow rate is too low or the water pressure is too low to penetrate the work-piece.

Figure 2.7 shows the striation marks on a glass sample. The h_c can be easily identified according to [7]. Below the depth of h_c, the jet-workpiece interface curvature changes significantly. It can be noticed that the striation marks do not develop below the depth h_c but develop from the top of the kerf edge.

2.4 Discussions

Figures 2.3 - 2.7 show the appearance of the striation marks under normal cutting conditions. Several features observed in these pictures can not be explained by the existing theories of striation formation. For example, under the same cutting conditions, a totally different striation patterns are observed when cutting is carried out in different directions. According to the existing notions, it should not have happened.

A frequency of jet induced striation equal to the ratio of the cutting speed to the jet diameter [7], has not been observed in our study. The h_c is also questionable parameter in the definition of the striation formation. This suggests that there are reasons for the striation formation during AWJ machining which have not been reported yet.

CHAPTER 3

EXPERIMENTAL SETUP AND METHODS

3.1 Abrasive Waterjet Cutting System

Two waterjet cutting systems developed by Ingersoll-Rand company were used in this study. The first system is based on (Figure 3.1) a 5-axis gantry robot. The cutting head is mounted on this gantry. The translation along the X-axis is controlled by a rack and pinion system. For translations along the Y- and Z-axes are controlled by two motorized ball-screws. Two rotary axes, perpendicular to each other, one in the horizontal (i.e. the pitch motion) and the other one in the vertical direction respectively (i.e. the roll motion), permit angular displacements within 200 and 360 degrees. The 5-axis motion of the cutting head is controlled by an Allen Bradley 8200 series CNC controller.

In the second waterjet cutting system (Figure 3.2) the cutting head is mounted on a 3-axis gantry robot. The motion along the X-axis and Y-axis is controlled by a rack pinion system and a motorized ball-screw, respectively. An Allen Bradley 8400 series CNC controller allows programmable and manual motion of the cutting head along the X- and Y-axes; the position of the cutting head along Z-axis can be controlled manually.

The high pressure water supply system includes a water softener, a booster pump, and an intensifier as shown in Figure 3.3. The water softener is used to remove the iron and calcium dissolved solids that will cause damage to the sapphire nozzle. Then softened water is fed to the booster pump which produces the pressure of 1,500 psi. This water goes to the intensifier which uses a hydraulically driven, double-acting, reciprocating plunger pump, which increases the water pressure from 1,500 psi to as high as 60,000 psi. For safety reasons, the maximum operating pressure of the

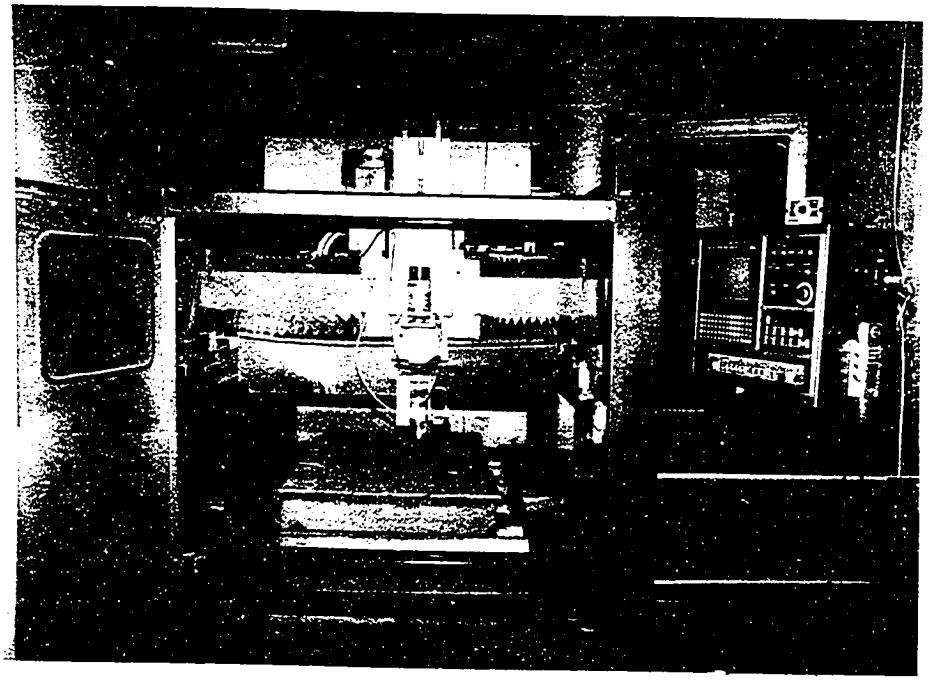

Figure 3.1 5-axis waterjet cutting system.

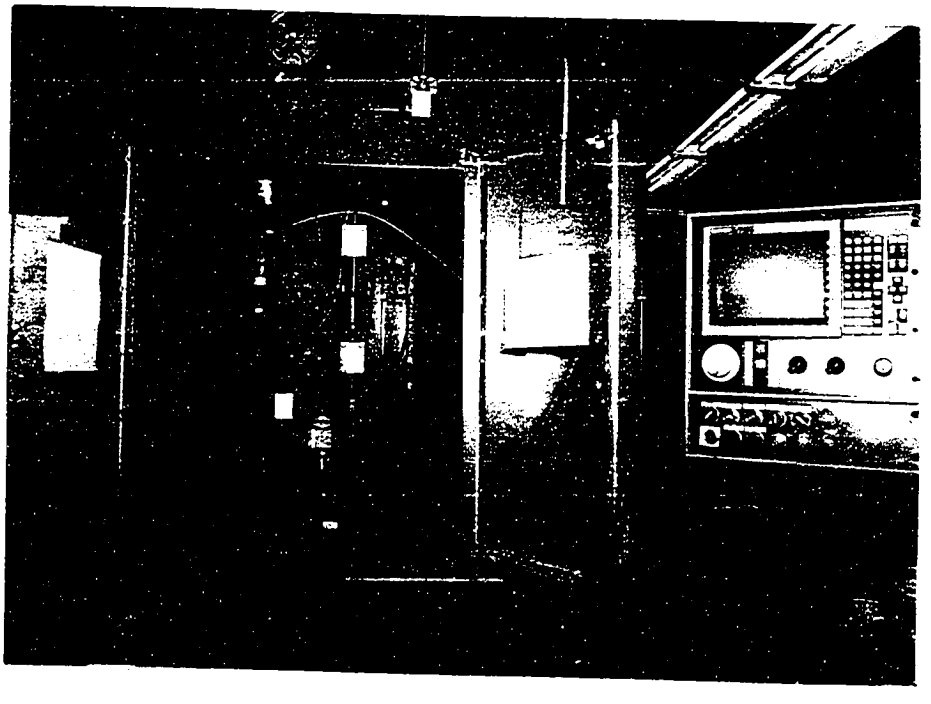

Figure 3.2 2½-axis waterjet cutting system.

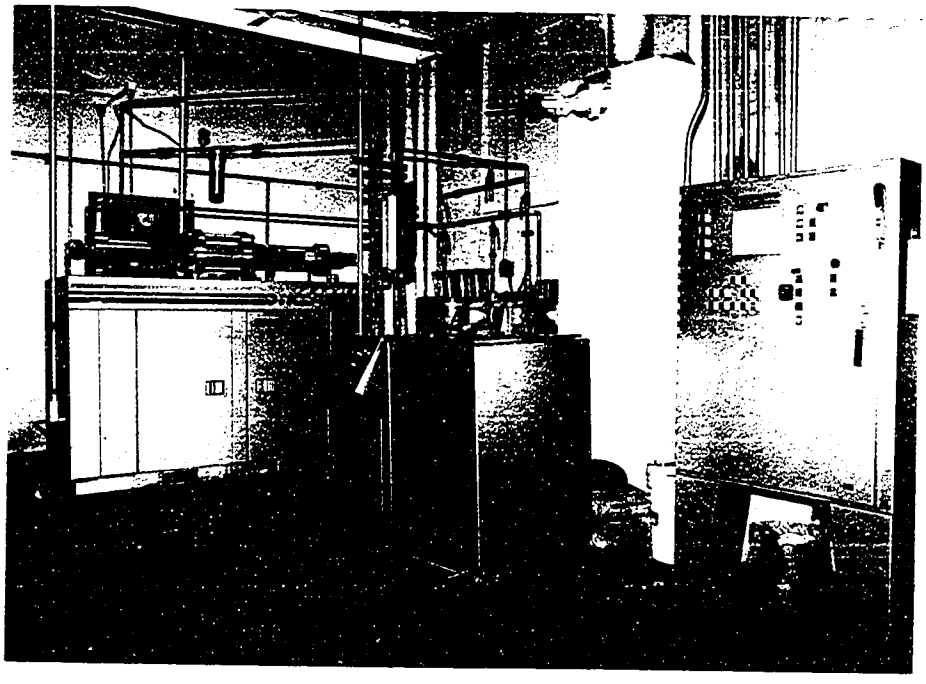

Figure 3.3 High pressure water supply system.

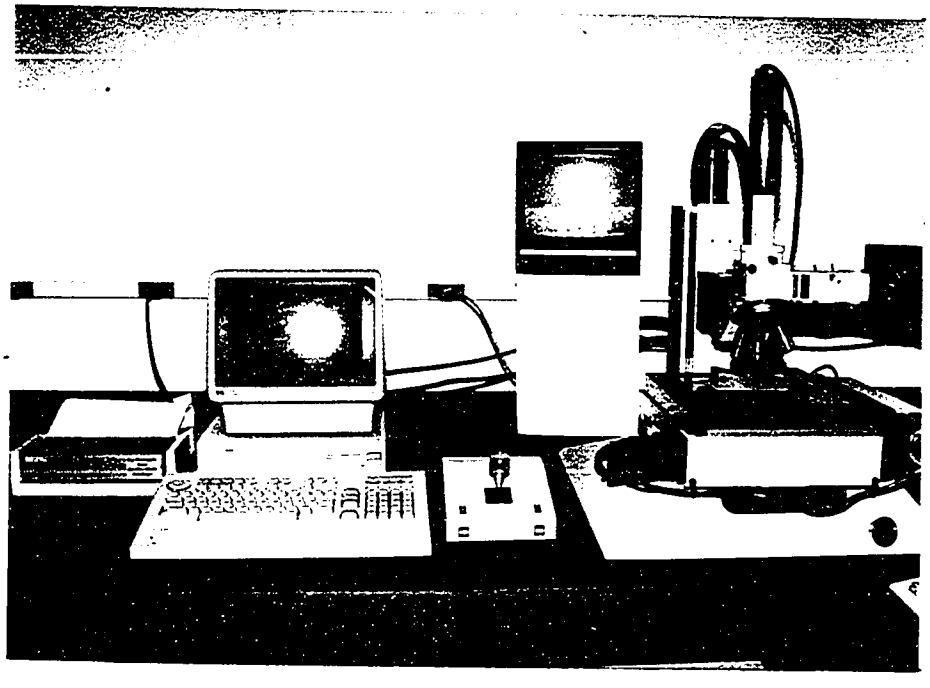

Figure 3.4 Matrix Videometrix Econoscope.

intensifier is maintained at 50,000 psi. The intensifier system also contains a water accumulator that is used to reduce pressure pulsation at the nozzle.

The abrasive delivery system includes a vibrator feeder, catch hopper and a flexible tube. A rate selector on the control panel is used to control the vibration amplitude of the feeder, thus changes the abrasive flow rate. The abrasives flows through the pipe and is sucked into the mixing chamber of the nozzle body.

3.2 Surface Profile Measurement System

The surface topographies of all the samples are measured by the Matrix Videometrix Econoscope shown in Figure 3.4. The Econoscope uses non-contact techniques to provide rapid dimensional verification of complete parts or specified features of a part. It comprises a general purpose computer (HP-9000 series), a 3-axis positioning control system, and a digital image processor and part monitor section. The software is divided into six major functions. The *topo* function is the module that we used in this study. In this module, the points to be measured, size of the measurement matrix, magnification lenses and the light intensity can be specified by the user; and then they executed automatically. The data representing the surface profiles include the X, Y, and Z coordinates of the measured points. They are stored in the computer and then downloaded to a 80386 based personal computer via the RS-232 port for further analysis.

The surface profile data matrix in our measurement were equally spaced. The distance between two points depended on the cutting speed. For example, if the cutting speed is 60 *mm/min.* and the sampling rate is 10 Hz (points/sec.) then the space between two neighboring points, δx, is,

$$\delta x = \frac{60(mm/\min)}{60(\sec/\min)\times 10(pts/\sec)} = 0.1(mm/pts) \qquad (3.1)$$

If one thousand points were measured from one surface profile then the sampled data length is 100 *mm* and the sampling rate is 10 Hz.

3.3 Vibration Measurement

The characteristics of the cutting head vibration enabled us to monitor the dynamics of the cutting head under different process conditions. These were compared with the characteristics of surface profiles. An accelerometer and a laser displacement meter were used to measure the vibration signal.

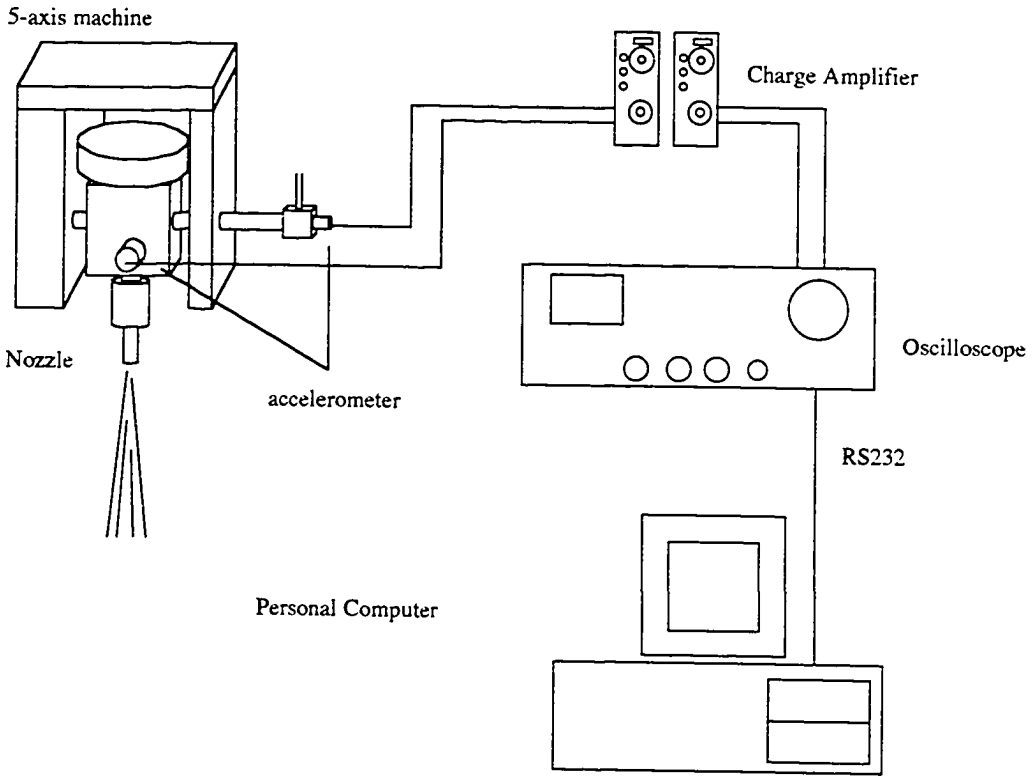

Figure 3.5 Schematic of the test and data acquisition setup.

3.3.1 Acceleration Measurement

The schematic of the data acquisition system is shown in Figure 3.5. Two Kistler 8002 accelerometers were used to measure the vibrations in both X- and Y-directions. The transducers were mounted as close as possible to the nozzle to acquire accurate vibration signals. In order to reduce the noise level from the machine ground circuit, the accelerometers were mounted on a glass plate. The Nicolet digital oscilloscope was used for data collection. Digital data were then transmitted to a personal computer (PC) via the RS-232 port for further processing. The schematic of the acceleration measurement from the nozzle body during cutting is shown in Figure 3.6.

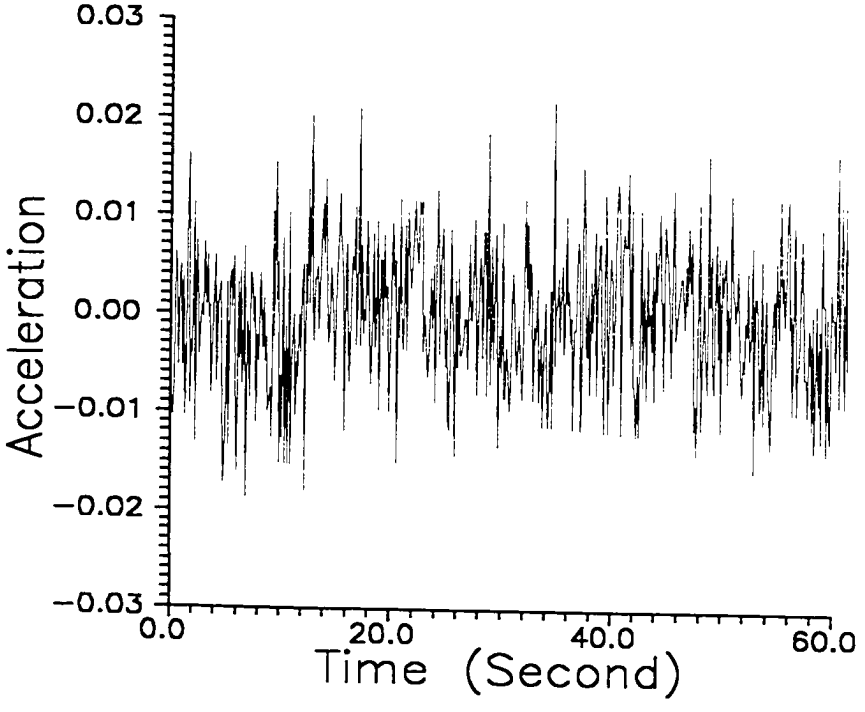

Figure 3.6 Acceleration of the nozzle body during cutting. (traverse rate = 127 mm/min.)

3.3.2 Displacement Measurement

A non-contact laser displacement meter (LDM) LC-2010 made by Keyence Corp. was used to measure the vibration displacement. The LDM was held by a vise and placed on the top of the catcher. The laser beam was pointed to a flat surface on the cutting head. Due to the limited space on the cutting head, the displacement signals were taken within the 50 mm length. The analog output data of the LC-2000 controller was displayed on a Nicolet digital oscilloscope and then downloaded to a PC via the RS-232 port for further processing. The measured displacement of the cutting head during cutting is shown in Figure 3.7.

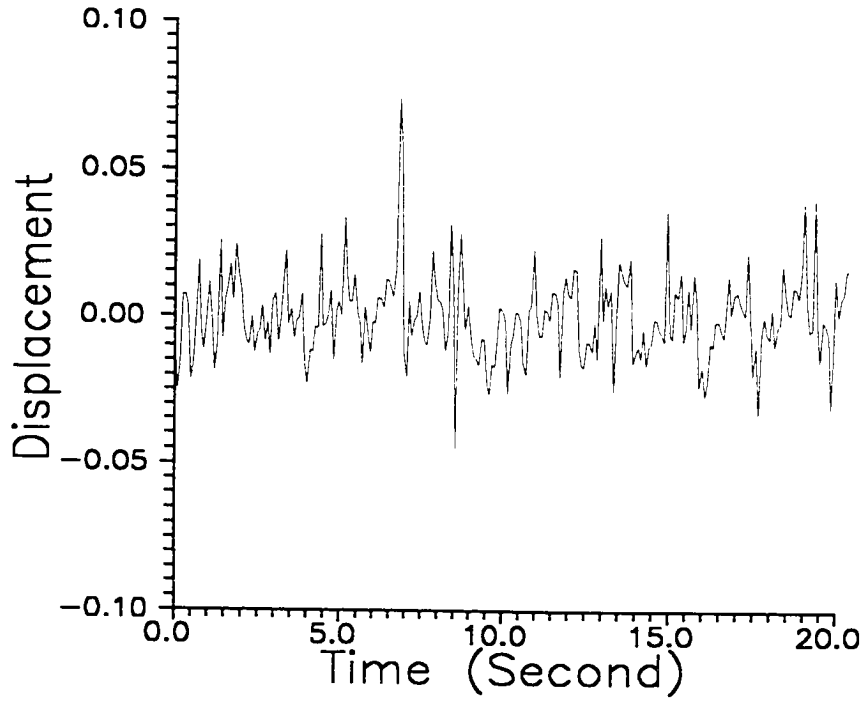

Figure 3.7 Displacement measured from the nozzle body during cutting. (traverse rate = 60 mm/min.)

3.4 Compliance Measurement

Compliance is the ratio of the displacement to the input force. In robotics, it represents the flexibility of the robot in the force-applied direction. The compliance is an inherent characteristic of the controlled robot [22]. In the waterjet cutting system, the cutting head is mounted on the frame of the gantry robot. The robot structure is subjected to the force induced by the jet. If the robot structure is not rigid enough, it is possible that the robot structure resonance is excited when the jet is on. The compliance was measured at four locations as shown in Figure 3.8 by using a force transducer to push the robot. The displacement at the corresponding position was measured by LDM. The force versus displacement plot is depicted in Figures 3.9 - 3.12. It can be noted that the location marked by "*a*" is the highest. At the other three locations, the compliance is much lower than that in location "*a*". This is due to the soft wrist element in the rotational joint A.

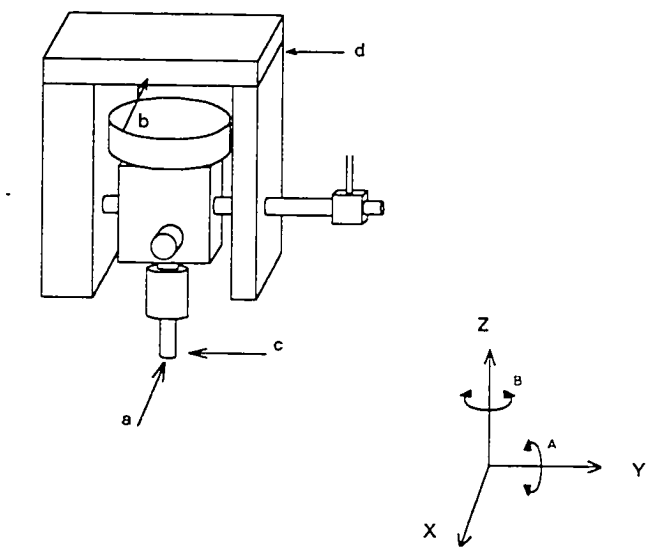

Figure 3.8 Schematic of the end-effector showing four locations where measurements were made.

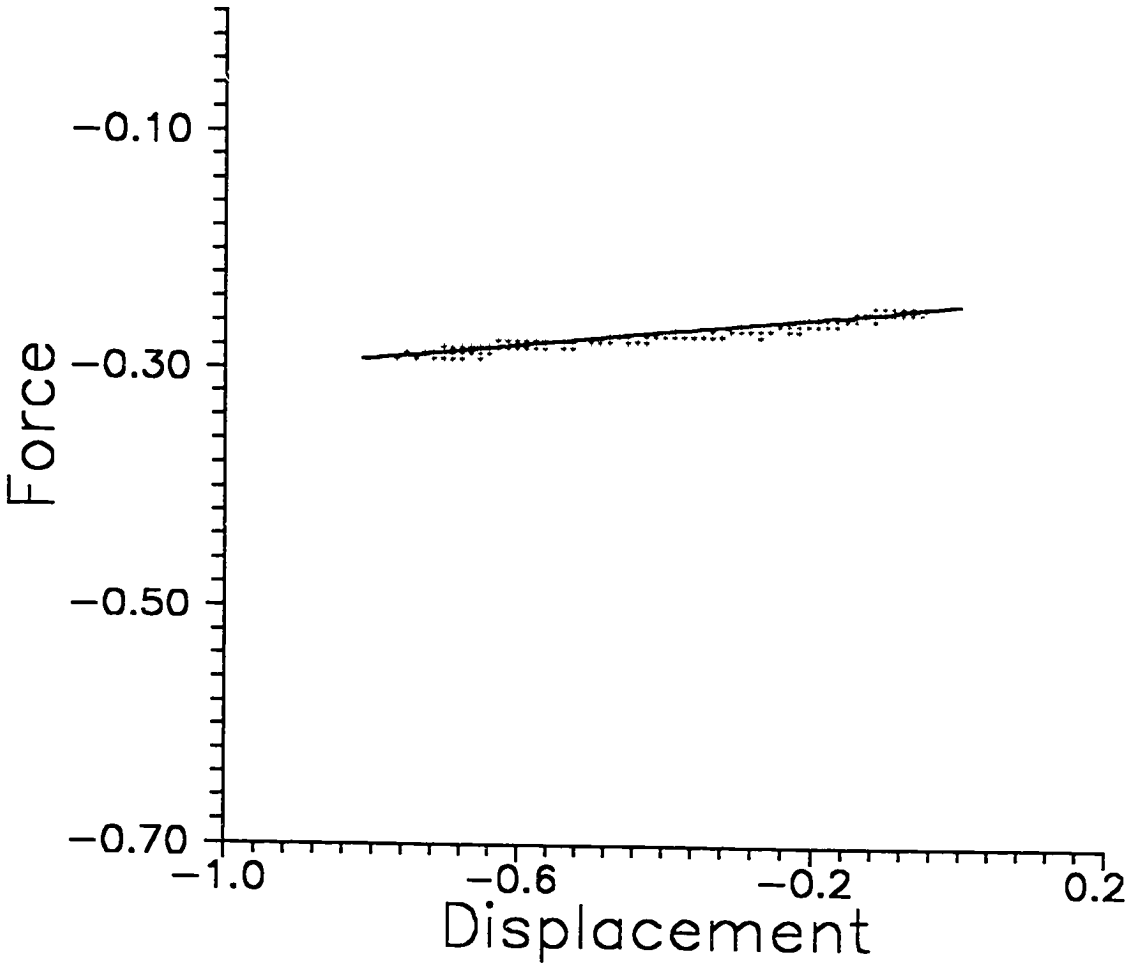

Figure 3.9 Plot of force versus displacement. (force applied to location *a* of Figure 3.8.)

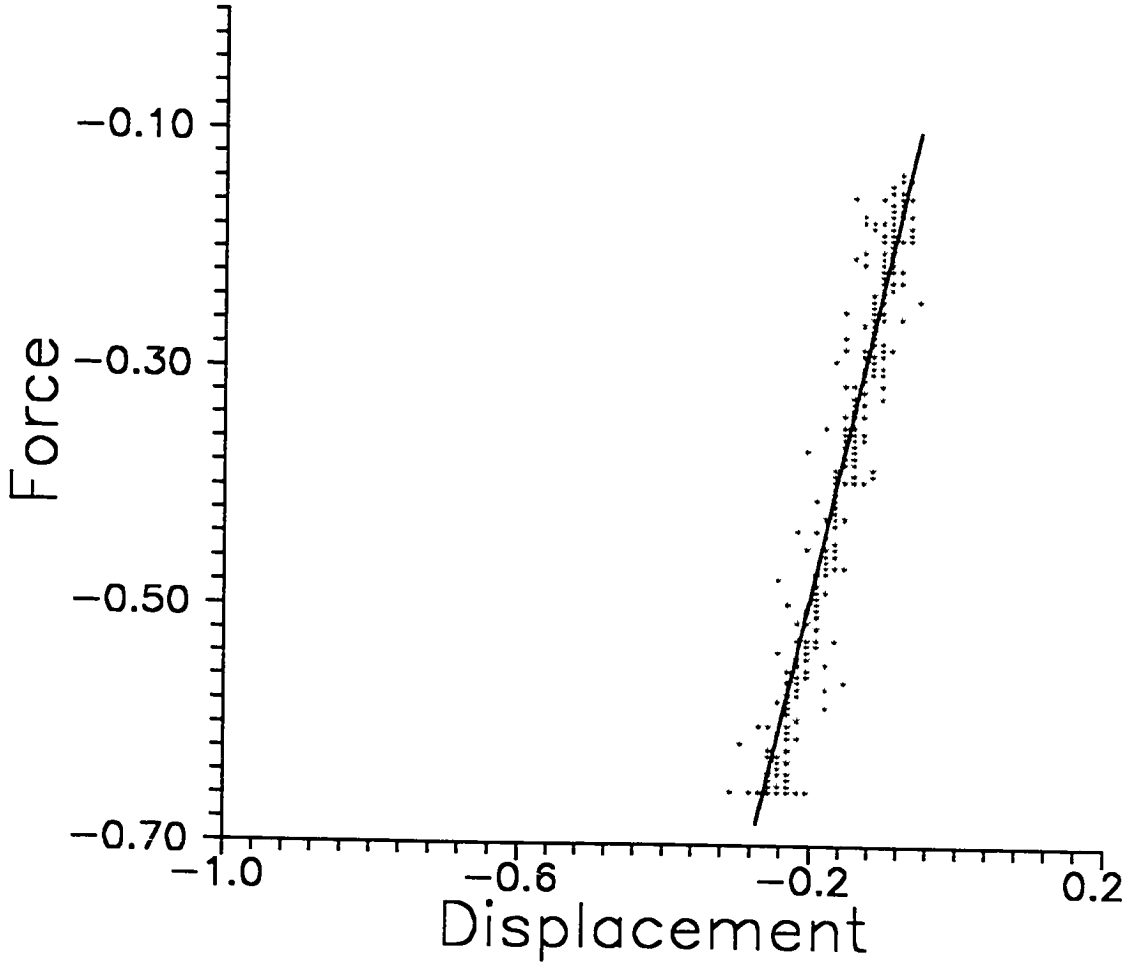

Figure 3.10 Plot of force versus displacement. (force applied to location *b* of Figure 3.8.)

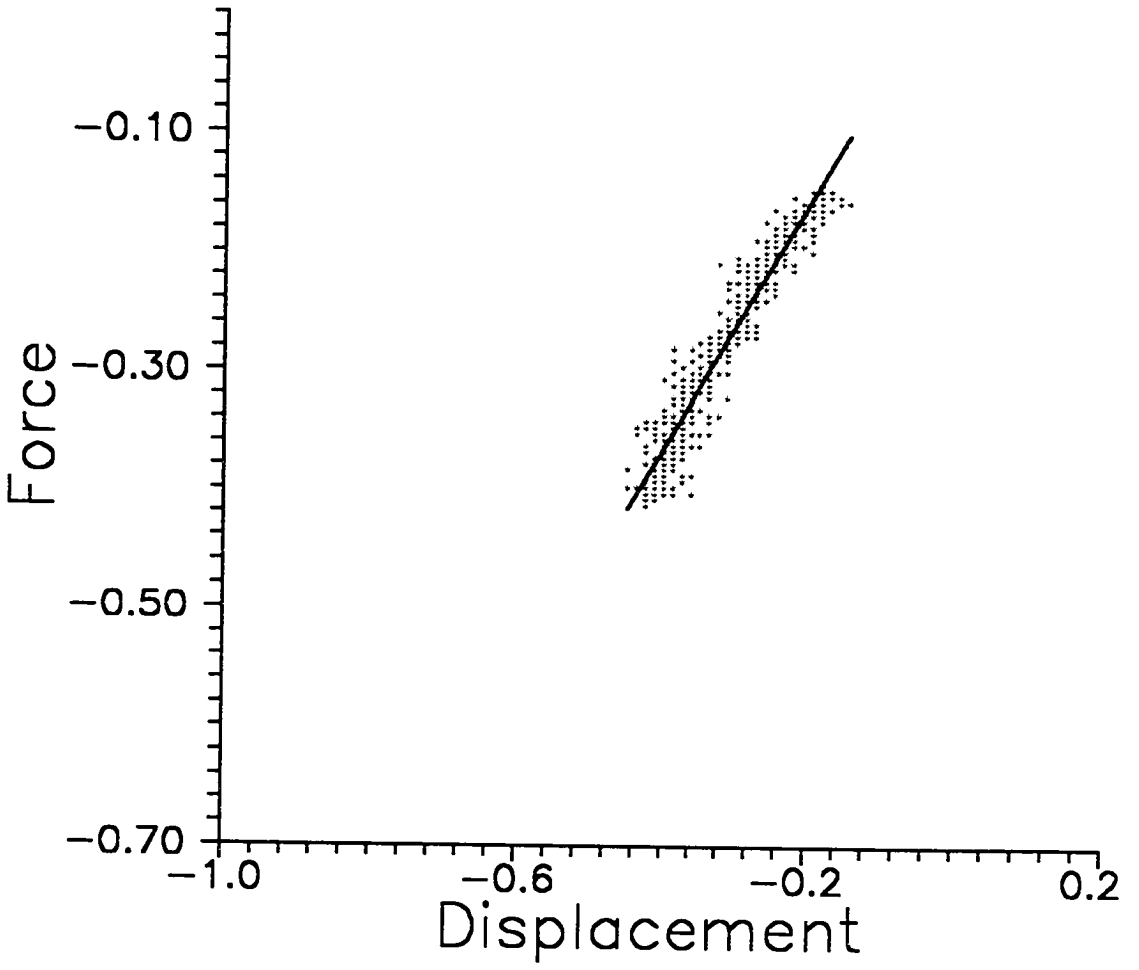

Figure 3.11 Plot of force versus displacement. (force applied to location *c* of Figure 3.8.)

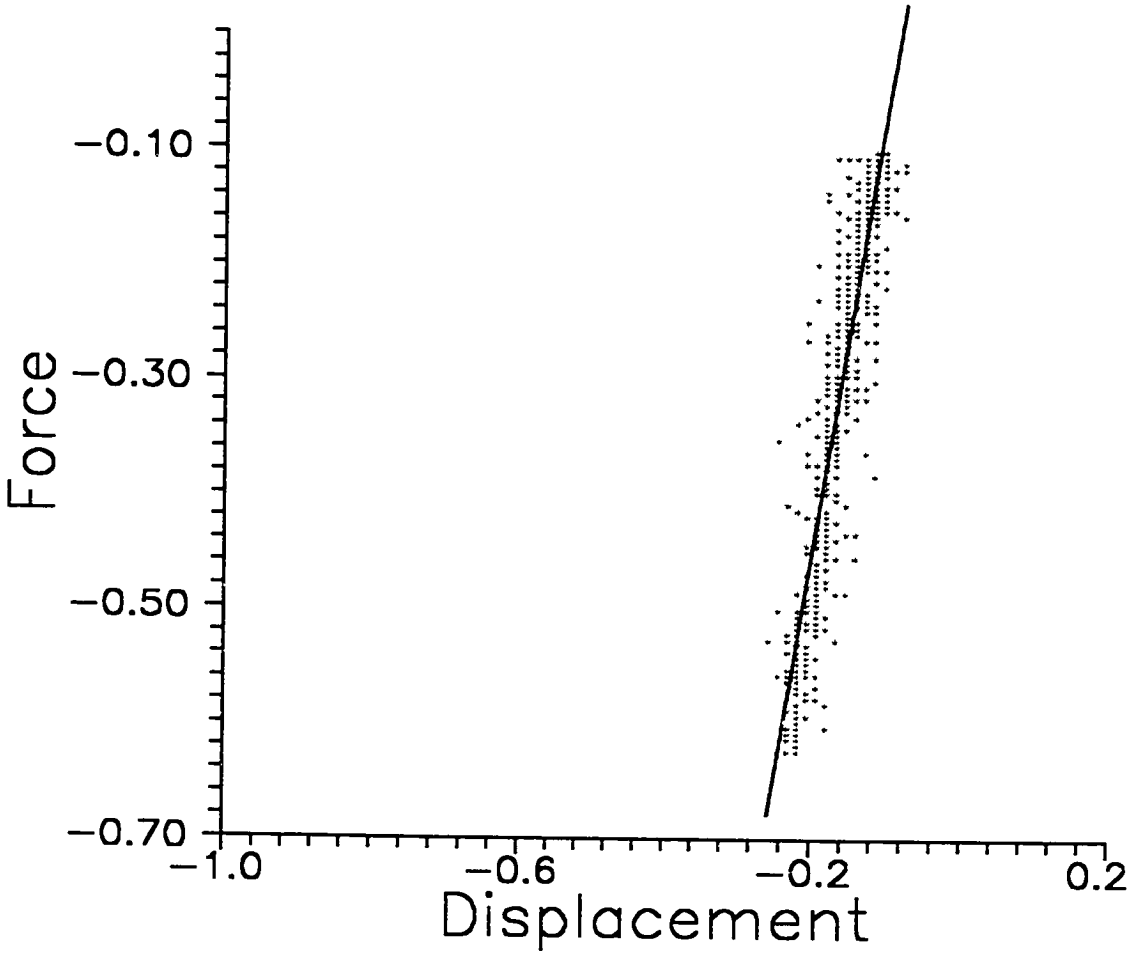

Figure 3.12 Plot of force versus displacement. (force applied to location *d* of Figure 3.8.)

3.5 Modal Testing

The compliance represents the static characteristic of the structure. The values were used to evaluate the flexibility of the structure in the direction in which a semi-static force was applied. The dynamic characteristics of the structure can be determined experimentally or theoretically. For a simple system such as a single mass-spring-damper system, mathematical description of the vibration behavior is readily available. For a complex system such as the 5-axis robot, theoretical construction of a mathematical model is difficult. An experimental technique is used to identify the vibration behavior of this system.

The experimental determination of the study of vibration behavior is termed modal testing. For a constant parameter, linear system [23], the input/output relationship can be expressed by the equation,

$$y(t) = \int_{-\infty}^{\infty} h(\tau) \cdot x(t-\tau) \cdot d\tau \tag{3.2}$$

where $h(\tau)$ is dynamic characteristic of a constant parameter linear system; $h(\tau)$ is defined as the output of the system at any time in response to a unit impulse input applied a time interval earlier. In equation 3.2 $x(t)$ is an arbitrary input while $y(t)$ is the output. This expression in the frequency domain is given by

$$G_y(f) = |H(f)|^2 \cdot G_x(f) \tag{3.3}$$

where $G_y(f)$ is the auto-spectral density function of the system output, $H(f)$ is the frequency response function of the system, and $G_x(f)$ is the auto-spectral density function of the input. The basic input/output relationship can be expressed by the following block diagram [24]:

Figure 3.13 Block diagram of the input/output relationship.

Only two out of three items on this diagram need to be measured to define completely the vibrations of the test structure. Theoretically, an impulse function is a white noise in the frequency domain; thus to obtain the characteristic of the system in the frequency domain divides the output function by a constant which is the area under the impulse function. In our experiment, the input signal was generated by an impulsive force hammer made by PCB PIEZOTRONICS, INC. The output signal was measured by LDM. The plots of the natural frequency of the robot in X and Y directions are shown in Figure 3.14 and 3.15. These frequencies are 20 and 26 Hz, respectively. Due to high compliance and a high damping coefficient in the pitch joint, an experimental study of this point was carried out by the use of a soft stick to excite the cutting head. Frequencies of 1 Hz and 3.5 Hz were observed. The result is shown in Figure 3.16.

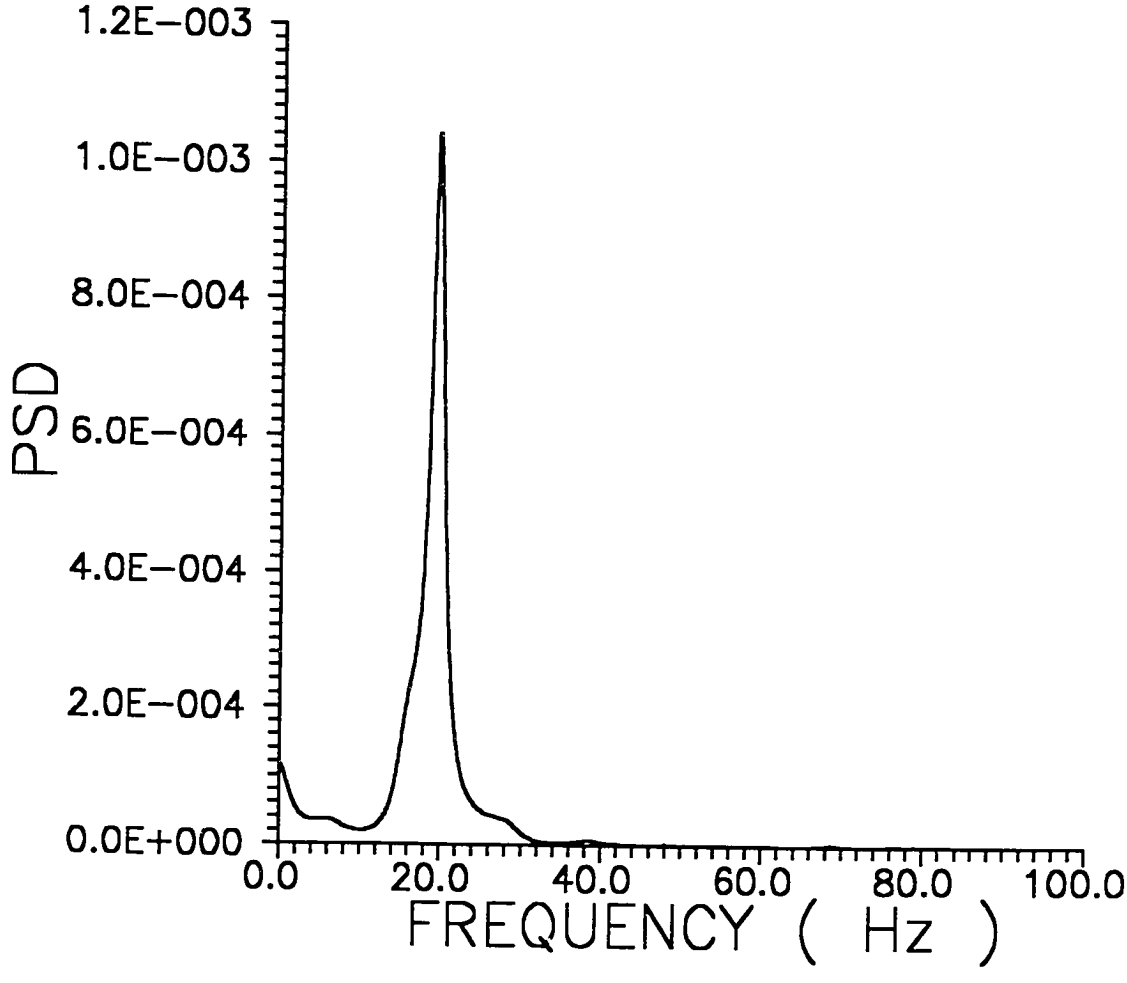

Figure 3.14 Power spectra of structure vibration measured at cutting head in X direction.

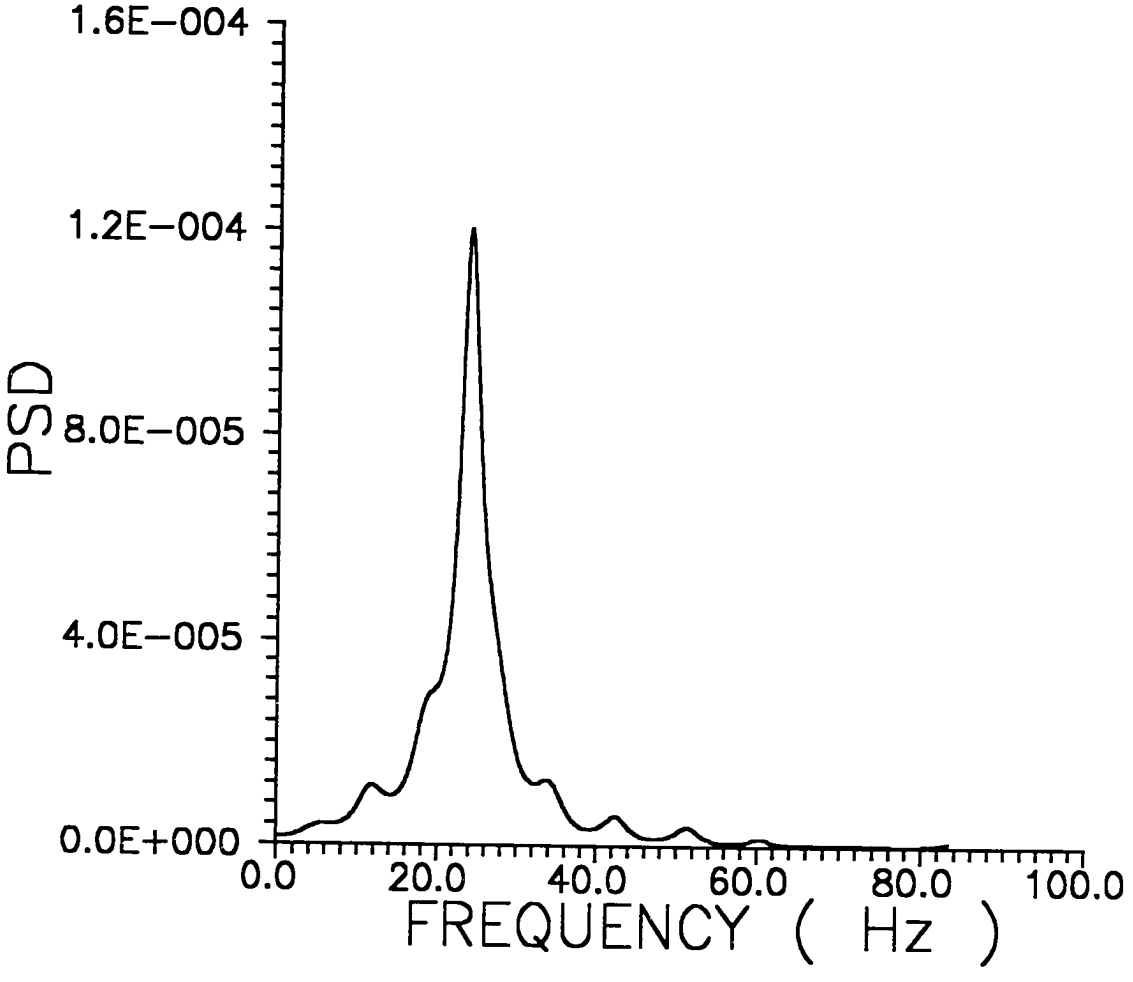

Figure 3.15 Power spectra of structure vibration measured at cutting head in Y direction.

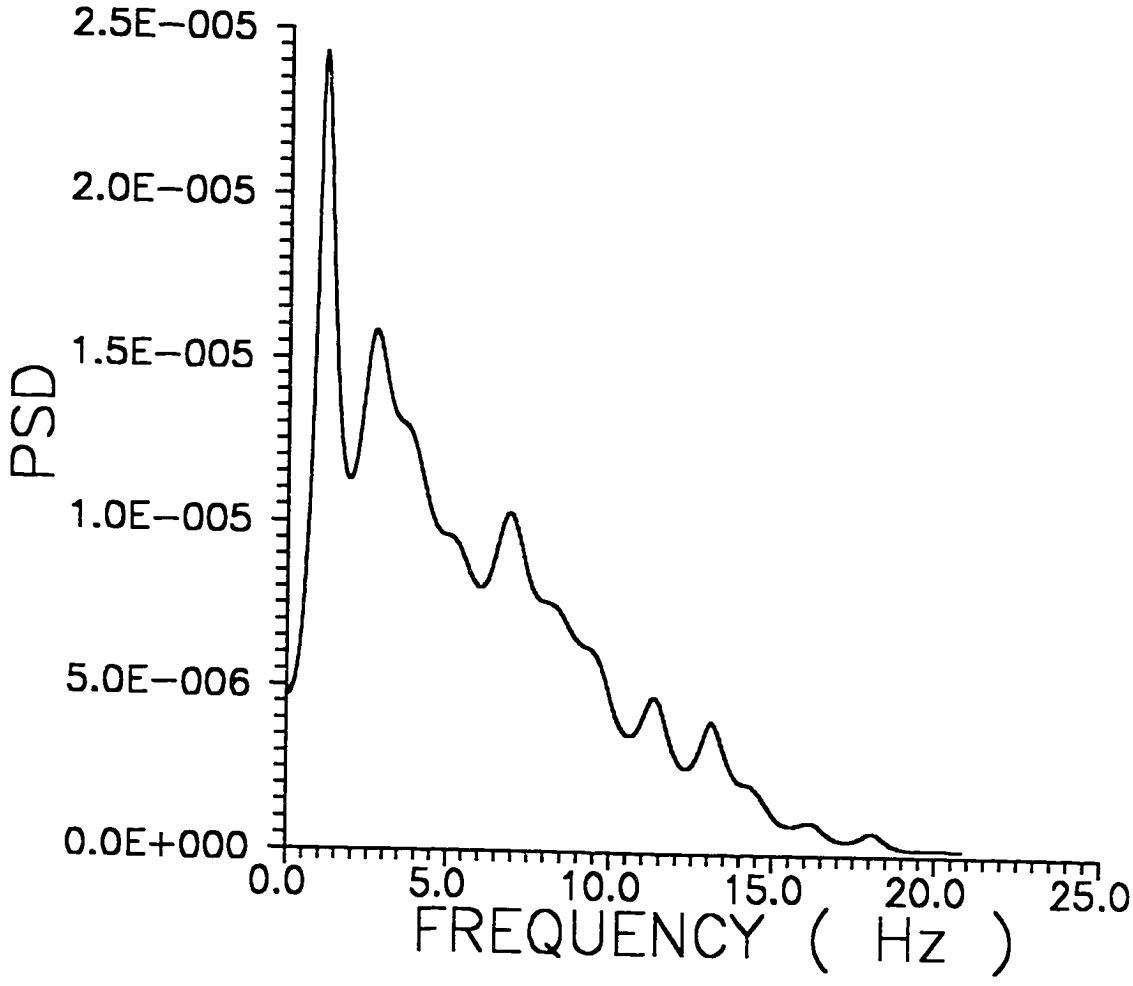

Figure 3.16 Power spectra of the cutting head vibration measured in X direction.

CHAPTER 4

DATA ANALYSIS METHODS AND PROCEDURES

The data representing the surface profiles and the vibration signals were recorded in the space and time domain, respectively. In order to determine the correlation between these two data, a quantity that represents the identical characteristic of variables should be used. The *power spectral density function* (PSD) is used to represent the frequency composition of physical data [23].

Two methods were used in our study to estimate the PSD function. For a large data set, the classical method is the most effective way. Wide-sense stationary (i.e. the mean and variance of the data at all time indices are constant) is the only assumption made for the data set. The application of this method to the surface spectral analysis is shown in [25].

The non classical methods usually require additional assumptions [26]. The accuracy of the estimated spectra depends on the accuracy of selected models as well as on the kind of selected spectral estimator. In our study, the auto regressive moving average (ARMA) model was selected as the process model [27]. The model had been applied to the surface characterization in the past [28] rather successfully. The transfer function which defines the input-output relationship is also discussed in this chapter.

The vibration signal was used as the input while the surface profile is the system output. The transfer function represents the integrated effect of such parameters as the stability of the waterjet, the mixing of the water and abrasive, the penetration depth, and the material properties. The following sections introduce the classical spectral estimation techniques, including data pre-processing, and the parametric method for the estimation of the transfer function.

4.1 Classical Spectral Estimation

The power spectral density function describes the frequency composition of a physical data in terms of the spectral density of its mean square values. The mathematical expression of the power spectral density function is given as

$$G_x(f) = 2 \cdot \int_{-\infty}^{\infty} R_x(\tau) \cdot e^{-j2\pi f\tau} \cdot d\tau \tag{4.1}$$

where $R_x(\tau)$ is the auto correlation function of the sample function $x(t)$. From this equation, we can see that the auto correlation function and power spectral density function are the Fourier transform pairs. The auto correlation function and the power spectral density function display similar information in the time and frequency domains, respectively. Before calculation of the power spectral density function, the following pre-processing operations should be carried out.

4.1.1 Sampling Considerations

Conventionally, the signal measured in the course of an experiment is in discrete form because the discrete data has a lower noise level than the continuous and also it is easy to manipulate this set of data by the digital computer. In practice, the signal can not be infinitely long and additional treatment should be carried out before calculating the spectra.

Let us consider a signal $u(t)$ sampled at points $\Delta t = h$ apart. The value of h determines a Nyquist folding frequency f_c (also call the cut-off frequency) given by

$$f_c = \frac{1}{2\Delta t} = \frac{1}{2h} \tag{4.2}$$

It is necessary then to determine an appropriate sampling interval. If sampling points are too close, the processing will include highly redundant data. That will

unnecessarily increase the labor and cost of calculations. On the other hand, sampling at points too far apart will lead to confusion between low and high frequency components, the so called *aliasing*, in the original data. Figure 4.1 shows the aliasing problem for two sine waves of different frequencies sampled at the same interval h. The sampling rate is then $1/h$. It should be noticed that if we sampled these two signals at the time instants $x_1, x_2, x_3,....,x_6$, we will get same sampled functions for these two sine waves. In practice, in order to define a frequency component in the original data, at least two samples per cycle are necessary. It means that the highest frequency which can be defined by a sampling rate $1/h$ is $1/2h$. The frequencies above $1/2h$ fold back into the frequency range from 0 to $1/2h$. This aliasing problem can be seen by using a cosine function where all the data at frequencies $2nf_c \pm f$ have the same cosine function values as the data at frequency f when sampled at $1/f_c$. At the time $t=1/f_c$

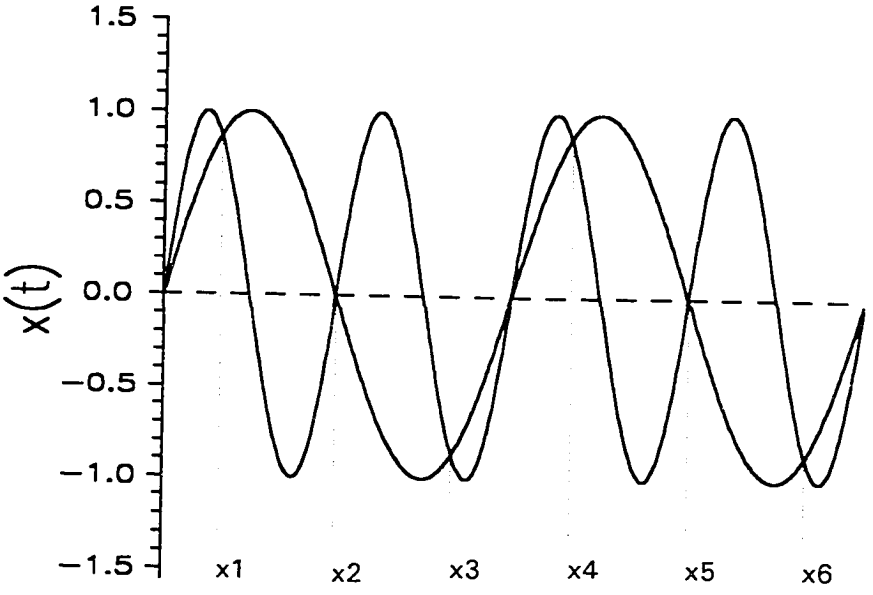

Figure 4.1 Illustration of aliasing problem.

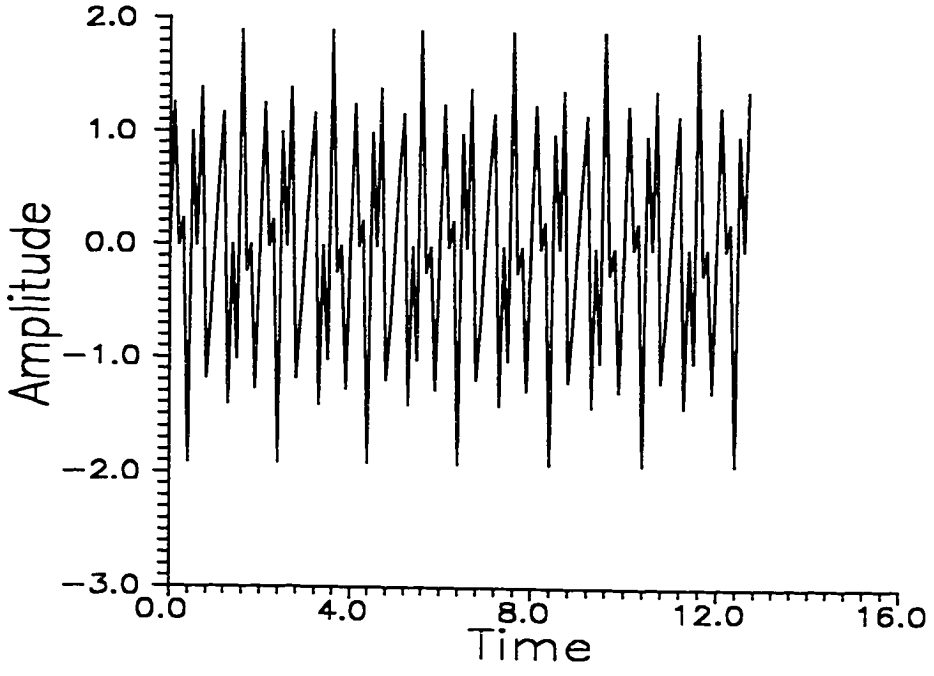

(a)

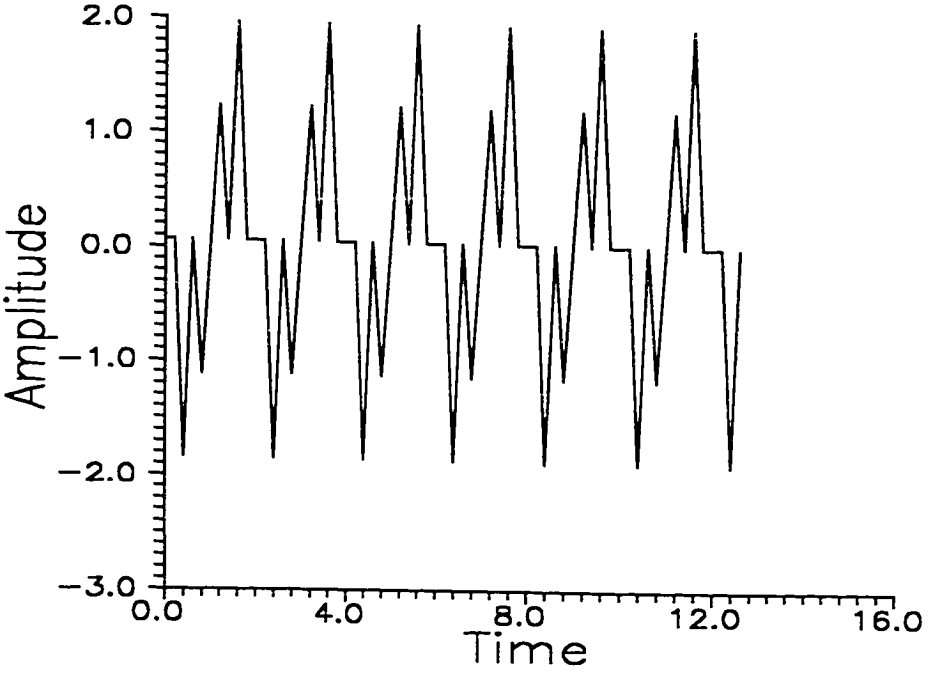

(b)

Figure 4.2 Superposition of two sine waves (f1= 2 Hz, f2=4.5 Hz),sampled at (a) 5 Hz (b) 2.5 Hz.

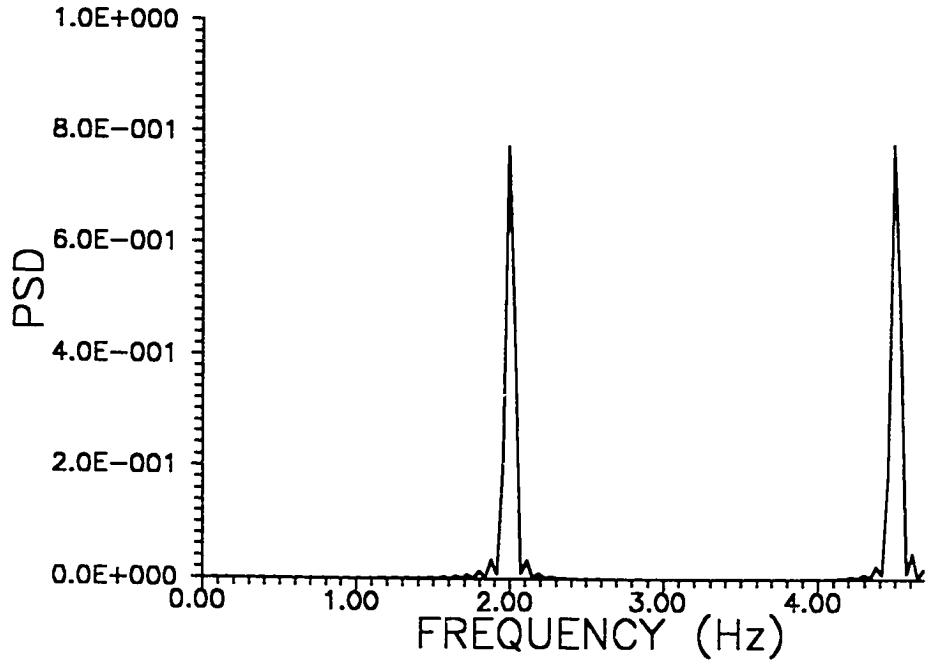

(a)

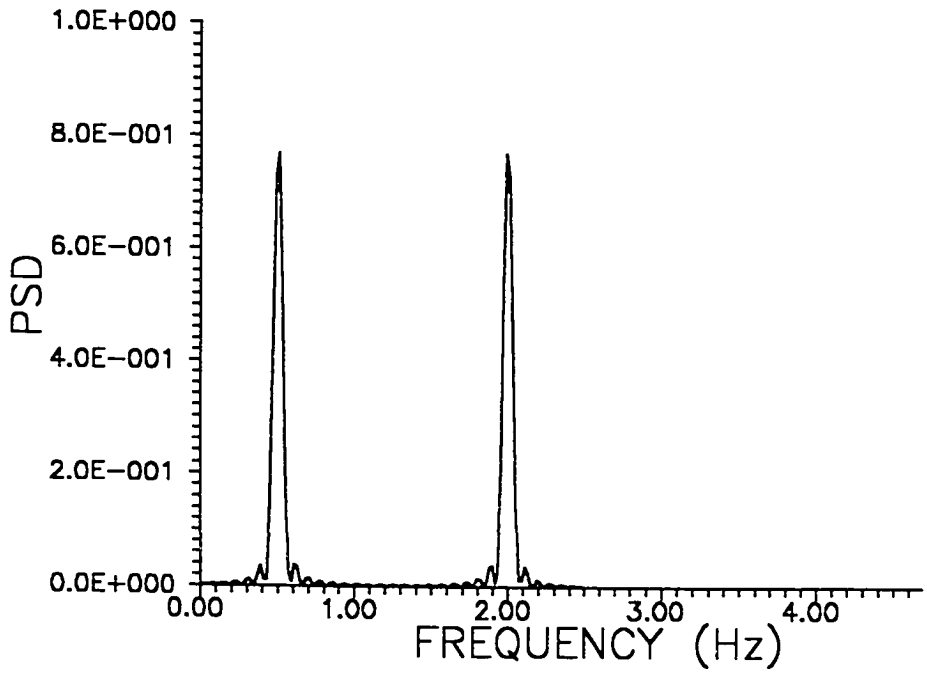

(b)

Figure 4.3 (a) True spectrum, sampled at 5 Hz, and (b) aliased spectrum, sampled at 2.5 Hz.

$$\cos 2\pi(2nf_c \pm f)t = \cos 2\pi n \cdot \cos 2\pi ft \mp \sin 2\pi n \cdot \sin 2\pi ft = \cos 2\pi ft \qquad (4.3)$$

Figure 4.2 shows the superposition of two sine waves (f_1=2 Hz, and f_2=4.5 Hz), sampled at 5 and 2.5 Hz respectively. Figure 4.3 shows the power spectral density functions of these two sampled functions, where (a) is the true spectrum and (b) is the aliased spectrum. To avoid aliasing, the cut-off frequency should be higher than the highest frequency in the original data or the original data should be filtered to remove information in the frequency range above the cut-off frequency.

4.1.2 Detrend

During the surface profile measurement, the surface to be measured can not be readily adjusted to a level parallel to the X-Y stage of a measuring device. A linear trend is thus superimposed on all the surface profiles during the measurement. This trend has to be removed from the recorded data, otherwise large distortions can occur in the later processing of spectral quantities. Another error is induced by the insufficient straightness of a commercial gantry robot which affects the straightness of the kerf edge. Figure 4.4 shows the magnified kerf edge. Both sides of the kerf edge have the same s-shape trend. This is a low-frequency component of the surface topography. The period of this component which is a cutting error is longer than the length of the recorded surface profile. The trend removal can be accomplished by the use of the least square method to fit the recorded data $\{u_n\}$ with a polynomial of degree K defined as

$$\hat{u}_n = \sum_{k=0}^{K} b_k (nh)^k \qquad n = 1,2,\ldots\ldots,N \qquad (4.4)$$

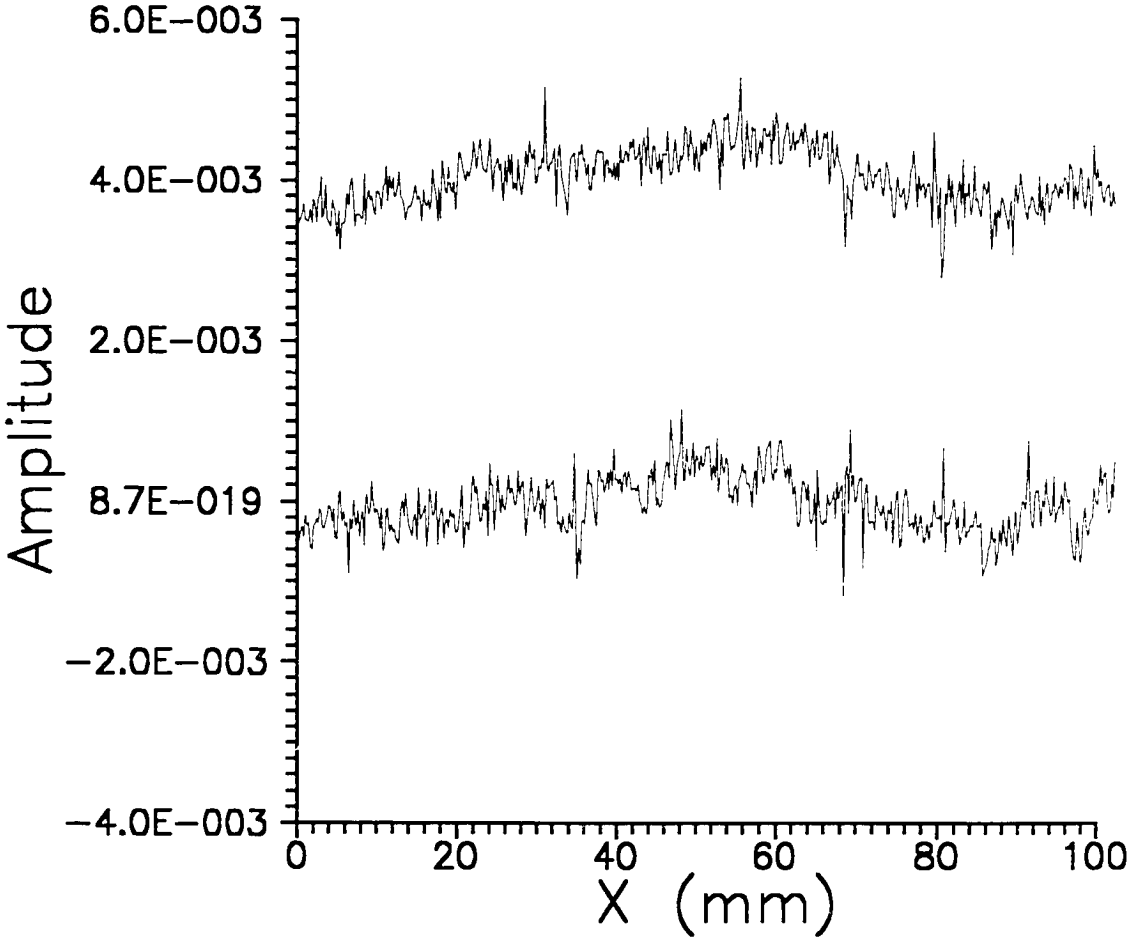

Figure 4.4 Magnified kerf edge.

where b_k is the coefficient of the polynomial, h is the sampling interval and N is the total number of samples. A least square fit is obtained by minimizing the squared discrepancies between the data values and the polynomial of degree K.

$$Q(b) = \sum_{n=1}^{N} (u_n - \hat{u}_n)^2 = \sum_{n=1}^{N} [u_n - \sum_{k=0}^{K} b_k (nh)^k]^2 \tag{4.5}$$

Taking the partial derivatives of $Q(b)$ with respect to b_k and setting them to zero yields K+1 equations of the form

$$\sum_{k=0}^{K} b_k \sum_{n=1}^{N} (nh)^{k+l} = \sum_{n=1}^{N} u_n (nh)^l \qquad l = 0,1,2,\ldots\ldots,K \tag{4.6}$$

which can be solved for the desired coefficients $\{b_k\}$.

The 9th-degree polynomial was chosen to fit the recorded data. Figure 4.5 shows the polynomial and the sampled data after detrend.

4.1.3 Fourier Transform

The Fourier transform is used to develop a frequency domain description for a time domain non-periodic function. The definition of the Fourier transform is given as

$$X(f) = \int_{-\infty}^{\infty} x(t) e^{-j2\pi ft} dt \tag{4.7}$$

In practice, the function $x(t)$ only exists in a finite time interval (0, T), so the finite-range Fourier transform will exist as defined by

$$X(f) = \int_{0}^{T} x(t) e^{-j2\pi ft} dt \tag{4.8}$$

The discrete version of the finite-range Fourier transform is

$$X(f,T) = h\sum_{n=0}^{N-1} x_n \exp[-j2\pi fnh] \tag{4.9}$$

At the frequency f_k, the transformed values give the Fourier components defined by

$$X_k = \frac{X(f_k,T)}{h} = \sum_{n=0}^{N-1} x_n \exp[-j\frac{2\pi kn}{N}] \qquad k = 0,1,2,.....,N-1 \tag{4.10}$$

where $f_k = kf = \frac{k}{T} = \frac{k}{Nh}$. To simplify the notation further, let

$$W(u) = \exp[-j\frac{2\pi u}{N}] \tag{4.11}$$

Because $W(N)$=1, thus for all u and v

$$W(u+v) = W(u)\cdot W(v) \tag{4.12}$$

Let

$$X(k) = X_k \qquad \text{and} \qquad x(n) = x_n \tag{4.13}$$

Then

$$X(k) = \sum_{n=0}^{N-1} x(n)\cdot W(kn) \qquad k = 0,1,2,.....,N-1 \tag{4.14}$$

The fast algorithm to calculate the power spectral density function is shown in the [23].

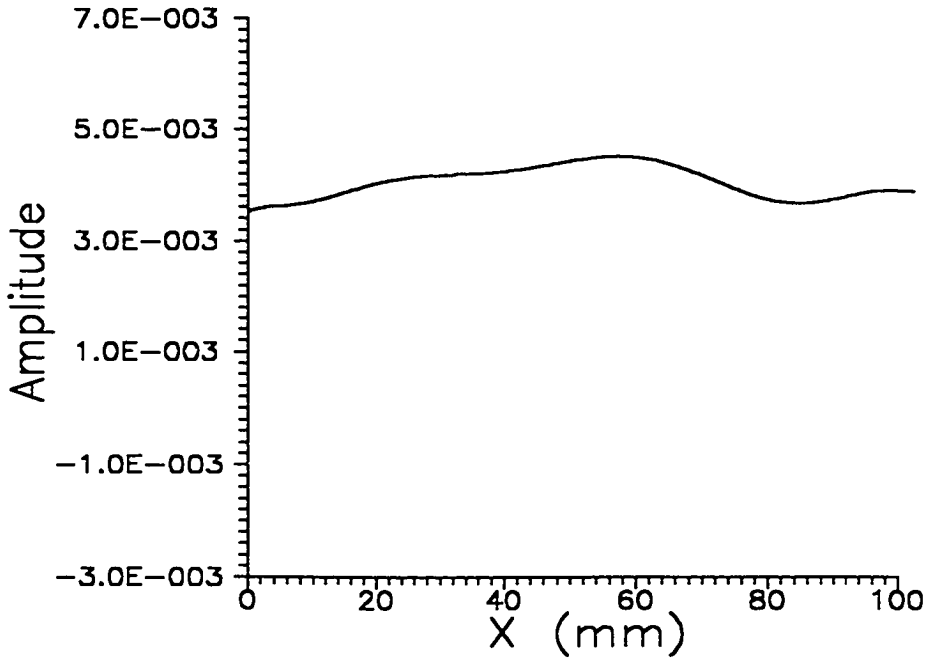

(a)

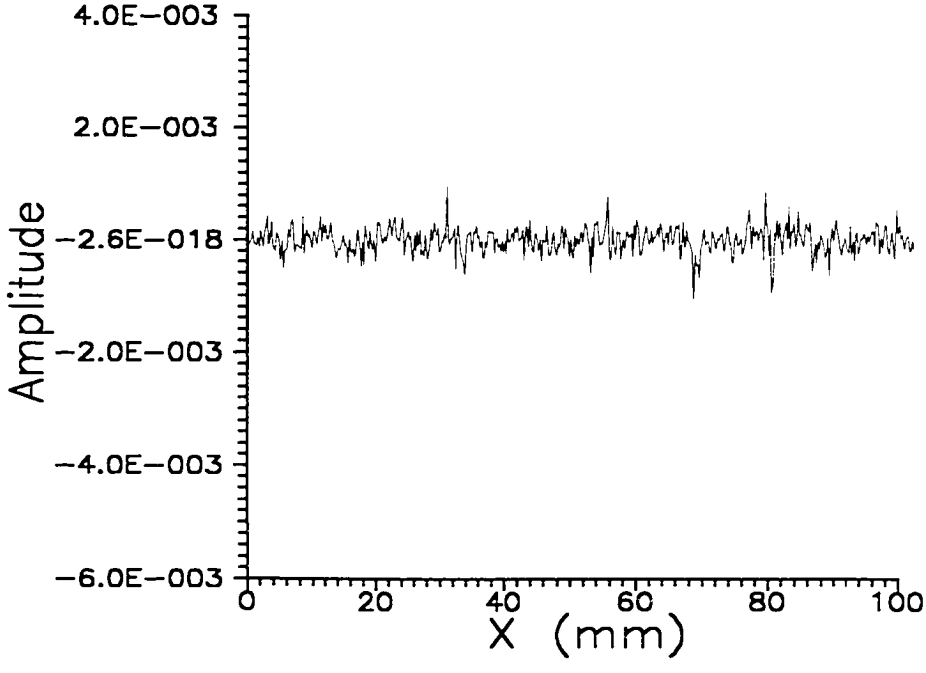

(b)

Figure 4.5 Illustration of the trend removal. (a) Polynomial of 9th degree, and (b) surface profile after trend removed.

4.1.4 Power Spectral Density Function

The data sequence used to estimate the power spectral density is defined over the interval (0, T). In practice, it is convenient to define this data sequence over the interval (-T/2, T/2). The finite length Fourier transform equation of Equation 4.8 can be viewed as a transform of an infinite length record $y(t)$ multiplied by a boxcar function $u_{T/2}(t)$.

$$\begin{aligned} X(f,T) &= \int_{-T/2}^{T/2} x(t)\cdot e^{-j2\pi ft}dt \\ &= \int_{-\infty}^{\infty} y(t)\cdot u_{T/2}(t)\cdot e^{-j2\pi ft}\cdot dt \end{aligned} \tag{4.15}$$

where $y(t)$ is the same as $x(t)$ in the range (-T/2, T/2) and

$$\begin{aligned} u_{T/2}(t) &= 0 \qquad t<-T/2 \\ &= 1 \qquad -T/2<t<T/2 \\ &= 0 \qquad t>T/2 \end{aligned} \tag{4.16}$$

The leakage error occurs mainly due to the existence of this boxcar filter, as illustrated by the side lode shown in Figure 4.3. To reduce this leakage, a smooth filter shape for FFT estimates can be obtained by tapering the original data set at each end.

The sampled data usually contains only a small amount of data, and thus the resolution of the obtained spectra is very low. To increase the spectra resolution, zeros can be added to the original data set. In our study, the amount of sampled data is 512 points. To double the spectra resolution, 512 zeros are addeded to the original recorded to make it 1024 points.

The power spectral density function of a finite length discrete data record can be expressed as:

$$\tilde{G}_x(f) = \frac{2}{T}|X(f,T)|^2 \tag{4.17}$$

where

$$X(f,T) = h \cdot \sum_{n=0}^{N-1} x_n \cdot \exp[-j2\pi fnh] \tag{4.18}$$

The FORTRAN program that calculates the power spectral density function is given in Appendix I.

4.2 Time Series Analysis

The time series analysis is a statistical method that deals with the analysis of a sequence of observed data. The observed data are usually ordered in time or space. This method is used to model the dependence of the observed data. The dependence of the data observed from a dynamic system is the *memory* of the system. This memory or dependence of the system enables us to predict the future values of the system from the past values once we quantify the dependence. The auto regressive moving average (ARMA) model is used to express the data dependence in this study. The auto regressive parameters determine the correlation between the signal at a given instants of time and the same signals at the n previous instant. The moving average part can be thought of as the output from a linear filter when the input is the white noise.

4.2.1 ARMA Process

The ARMA model can be expressed in the form as follows,

$$X_t - \phi_1 X_{t-1} - \phi_2 X_{t-2} - \cdots\cdots - \phi_p X_{t-p} = W_t - \theta_1 W_{t-1} - \theta_2 W_{t-2} - \cdots\cdots - \theta_q W_{t-q} \tag{4.19}$$

where X_t is the sampled data at the instance of time t. W_t is the white noise input with zero mean and a constant but unknown variance σ_W^2. ϕ_p and θ_q are the unknown parameters to be calculated from the ARMA model.

It is convenient to express the model by using the *back shift operator B* defined by

$$BX_t = X_{t-1} \tag{4.20}$$

and,

$$B^j X_t = X_{t-j} \tag{4.21}$$

Thus the ARMA(p,q) model can be written as

$$\Phi(B)X_t = \Theta(B)W_t \tag{4.22}$$

where

$$\Phi(B) = 1 - \phi_1 B - \phi_2 B^2 - \cdots - \phi_p B^p \tag{4.23}$$

$$\Theta(B) = 1 - \theta_1 B - \theta_2 B^2 - \cdots - \theta_q B^q \tag{4.24}$$

An alternative way to express this ARMA process is

$$X_t = \frac{\Theta(B)}{\Phi(B)} \cdot W_t \tag{4.25}$$

A procedure for selecting the appropriate order p and q of the ARMA process is needed. In this study, the Baysian information criterion (BIC) introduced by Schwarz

[29] is used. The values of p and q are selected from the consideration of minimization of the quantity:

$$BIC = (N-p-q)\cdot \ln[N\cdot \hat{\sigma}_W / (N-p-q)] + (p+q)\cdot \ln[N\cdot(\hat{\gamma}(0)-\hat{\sigma}_W)/(p+q)] \tag{4.26}$$

The value of the auto covariance function at lag k is $\hat{\gamma}(k)$ is given by:

$$\hat{\gamma}(k) = (N-k)^{-1}\cdot \sum_{t=1}^{N-k}(X_t - \overline{X})\cdot(X_{t+k} - \overline{X}) \tag{4.27}$$

where k= 0,.....,N-1, $\overline{X}_N$ is the mean value of the data, and $\hat{\gamma}(0) = n^{-1}\cdot \sum_{t=1}^{n}(X_t - \overline{X}_n)^2$.

The $\hat{\sigma}_W$ is the maximum likelihood estimate of the white noise variance given by:

$$\hat{\sigma}_W{}^2 = N^{-1}\cdot \sum_{t=1}^{N}\left|X_t - \hat{X}_t\right|^2 = N^{-1}\cdot \sum_{t=1}^{N}\left|\Phi(B)\cdot X_t + [1-\Theta(B)]\cdot W_t\right|^2 \tag{4.28}$$

The power spectral density function of an ARMA(p, q) process is

$$P_{ARMA}(f) = h\cdot \hat{\sigma}_W{}^2 \cdot \left| \frac{1-\sum_{k=1}^{q}\theta_k \cdot \exp(-j2\pi fkh)}{1-\sum_{t=1}^{p}\phi_t \cdot \exp(-j2\pi fkh)} \right|^2 \qquad -\frac{1}{2h} < f < \frac{1}{2h} \tag{4.29}$$

which is the Fourier transform of the auto covariance function.

4.2.2 Transfer Function

In the previous section, we were concerned with a single series of data, considered as a realization of a stationary stochastic system. Such data can always be represented by an ARMA model. The ARMA model can be extended to multiple series of data. In this section, we will show the single-input/single-output system model.

For a system with the input X_t and output Y_t, the output Y_t does not only depend on its past values but also depends on the input X_t. We can write the simple input-output equation as

$$Y_t = \Phi_{21}(B)X_{t-1} + \Phi_{22}(B)Y_{t-1} + \Theta_2(B)W_{2t} \tag{4.30}$$

Rewrite (4.30) to

$$Y_t = \frac{B\Phi_{21}(B)}{(1-\Phi_{22}(B))}X_t + \frac{\Theta_2(B)}{(1-\Phi_{22}(B))}W_{2t} \tag{4.31}$$

The input X_t can also be represented by the ARMA model

$$X_t = \Phi_{11}X_{t-1} + \Theta_1(B)W_{1t} \tag{4.32}$$

It can be seen that the first term on the right hand side of the equal sign in (4.31) is the transfer function. The block diagram for the transfer function is shown in Figure 4.6.

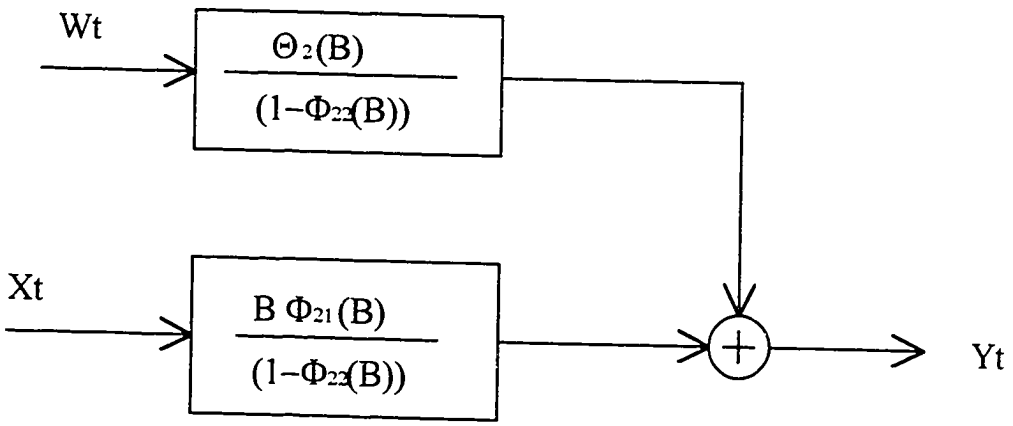

Figure 4.6 Block diagram of transfer function

CHAPTER 5

RESULTS AND DISCUSSION

5.1 Spectral Analysis of Surface Profile

The surfaces shown in Figures 2.3 and 2.4 are titanium samples of 20 mm thick that were generated at identical process parameters but at the different directions of the nozzle motion. The patterns of the striation marks are different. The surface profiles were measured from 2 mm (at the top of the cut) to 16 mm (almost at the bottom of the cut) from the top of the sample. The power spectral density functions of the surface profiles are depicted in Figure 5.1 and 5.2, respectively.

Figure 5.1 shows the surface spectra of the sample that was cut in the X-direction. At the depths 14 mm and 16 mm multi-peaks distributed in the frequency range from 0 to 2 Hz are observed while at the frequency above 2 Hz and the surface spectra of depths 2 mm to 12 mm, no clear peak can be identified. The sample that was cut in the Y-direction shows only a single peak at the frequency of 1 Hz for all depths, as shown in Figure 5.2. It can be readily noticed that the amplitude of the power spectral density functions of the sample cut in the Y-direction is much larger than that of the sample cut in the X-direction.

5.2 Effects of Cutting Speed on Surface Waviness

One significant observation is that the amplitude of the striation marks increases with the cutting speed. Figure 5.3 shows the effect of the cutting speed on the striation amplitude. The ½" steel plate was cut at different speeds from 40 mm/min. to 100 mm/min in the Y-direction by the 5-axis robot. Surface spectra similar to the spectra shown in Figure 5.2 were observed. The dominant surface frequency of the surfaces generated at these four different cutting speeds is 1 Hz. The mean square root of the

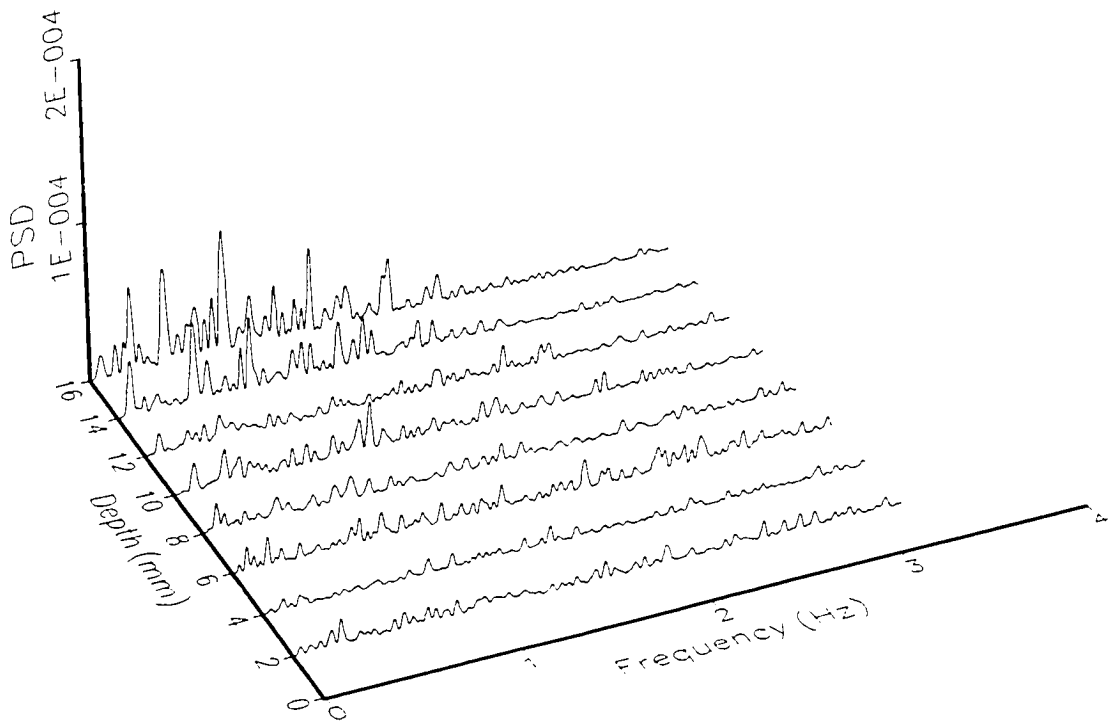

Figure 5.1 Power spectral densities measured from different depths (TI-GR2, cutting speed 80 mm/min., X-direction.)

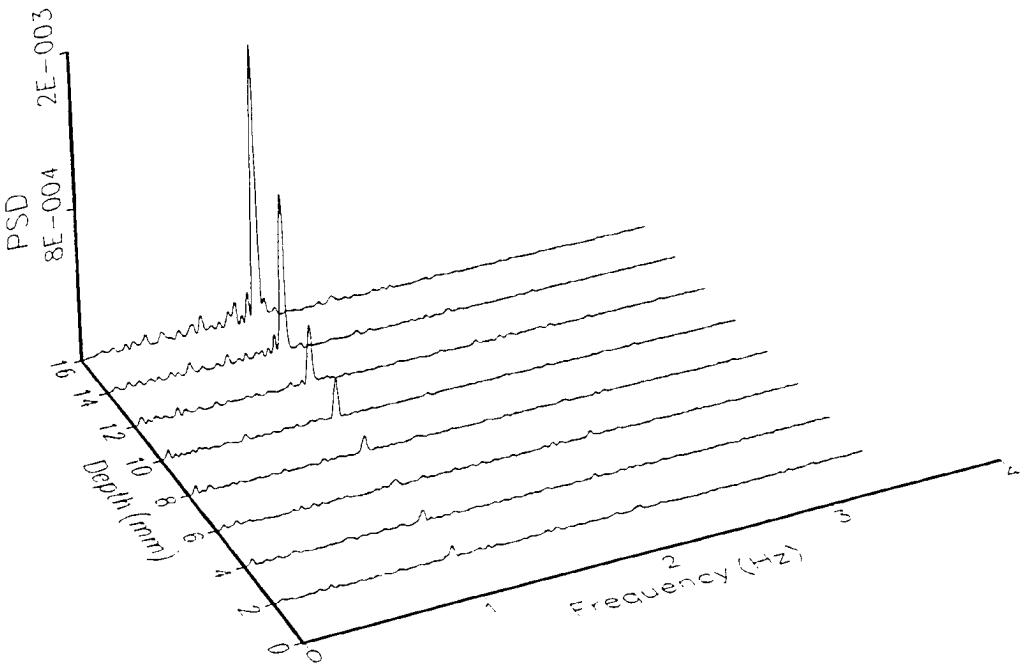

Figure 5.2 Power spectral densities measured from different depths (TI-GR2, cutting speed 80 mm/min., Y-direction.)

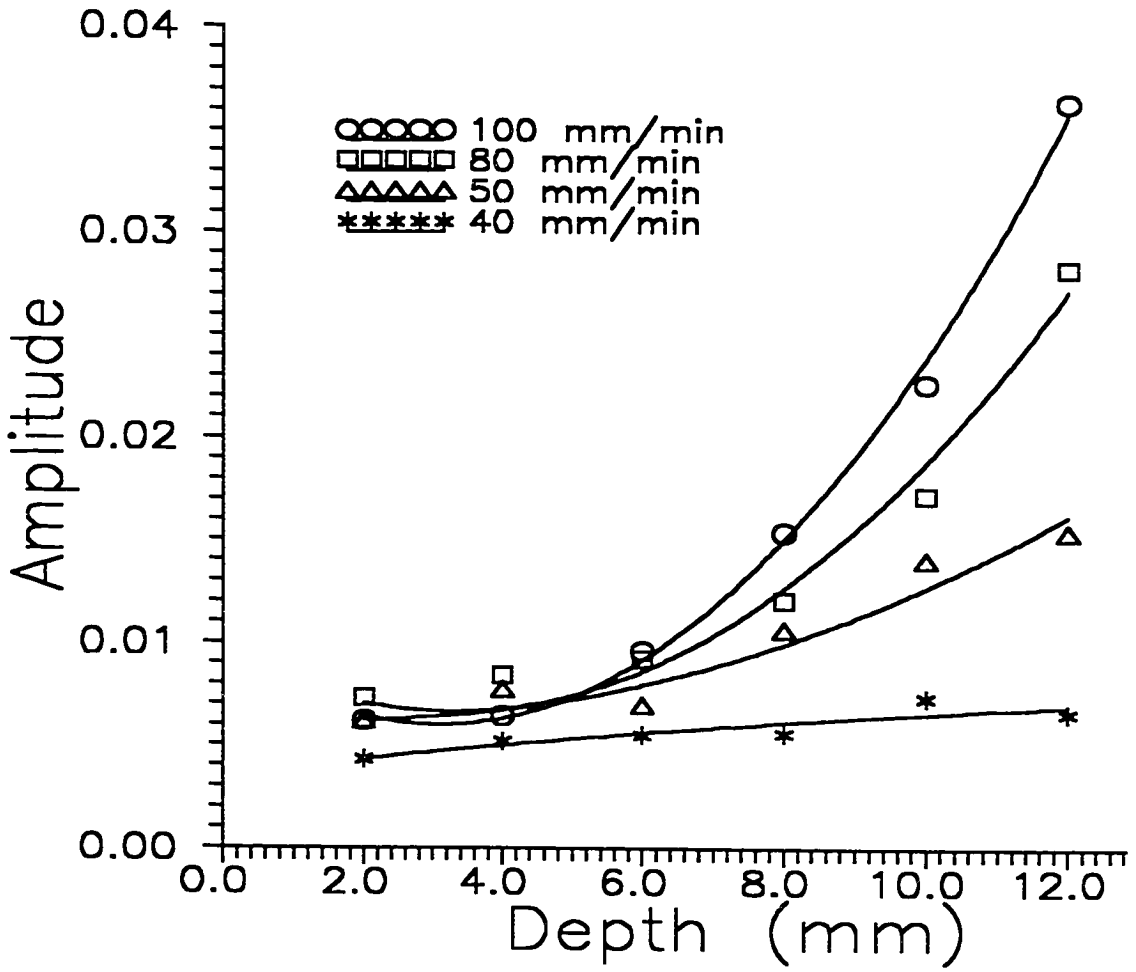

Figure 5.3 Plot of the amplitude of dominant striation versus depth of cut at different cutting speeds.

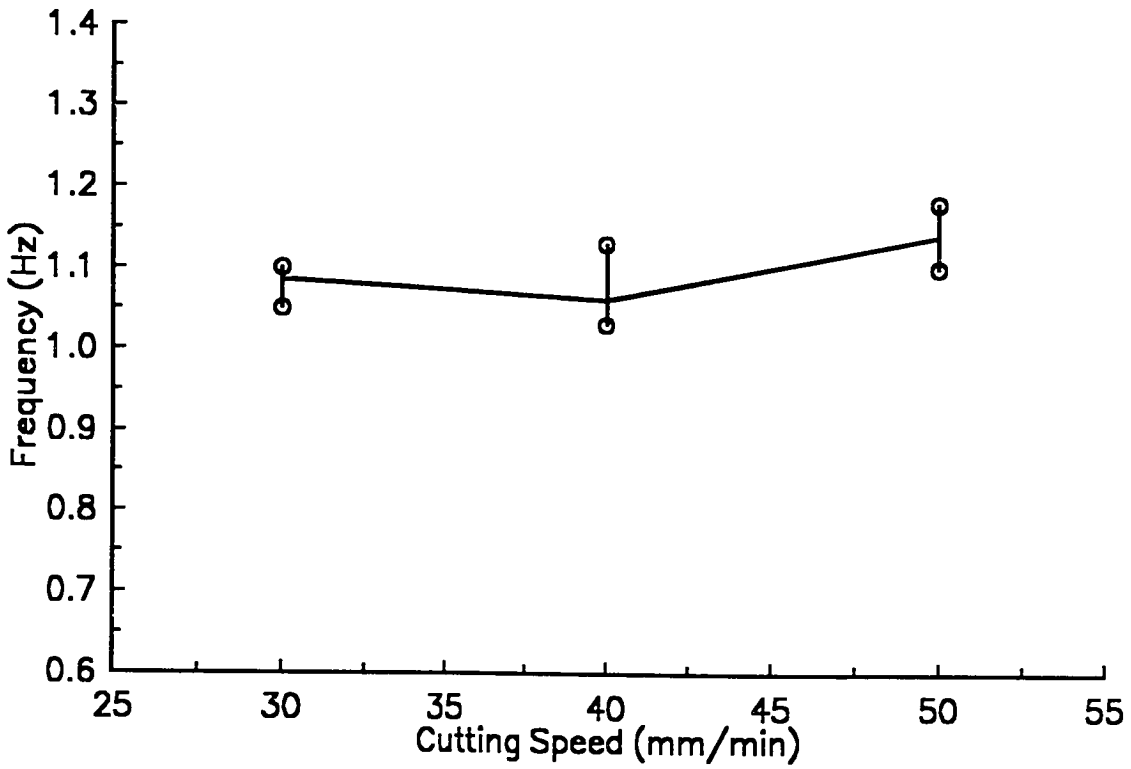

Figure 5.4 The dominant frequency of surface spectra generate at different cutting speeds at same location.

dominant frequency amplitudes shows that this amplitude is a second order polynomial of the distance from the top of cut (i.e. the depth.). The amplitude of the dominant frequency increases not only with the depth from the top of cut but also with the cutting speed. The relationship between the amplitude and the depth is similar for all cutting speeds.

5.3 Effects of Vibration on Surface Waviness

Due to the different striation patterns generated when cutting was done in the different directions, experiments of cutting steel sample with different speeds at the same location and with the same cutting speed but at the different locations were carried out to determine the effects of the structural dynamics on the surface topography. Figure 5.4 shows the plot of the surface dominant frequencies versus the cutting speeds, for samples cut at the same time and same location of the 5-axis waterjet machine. Figure 5.4 illustrates that the surface dominant frequency is subject to small changes when cut with different speeds. Table 5.1 shows the dominant frequencies of samples cut with same cutting speed, but at different locations. It can be noticed that except for the first cut which shows a higher dominant surface frequency, the dominant surface frequencies are almost the same when cutting is done at the same location, but the frequency change is significant with change of location.

Because the dominant striation frequency is independent of the cutting speed and because the compliance shows joint A (rotation about Y-axis) has the highest compliance we can suggest that the periodicity of the striation marks is due to the jet exciting, the pitch resonance of the end-effector. The different dominant frequencies generated at different locations are probably caused by the different dynamic characteristics of the gantry at various locations. To prove this hypothesis, the natural frequencies of the waterjet cutting system in X and Y directions were determined by the modal testing as described in Section 3.5. From Figure 5.2 it is apparent that 1 Hz

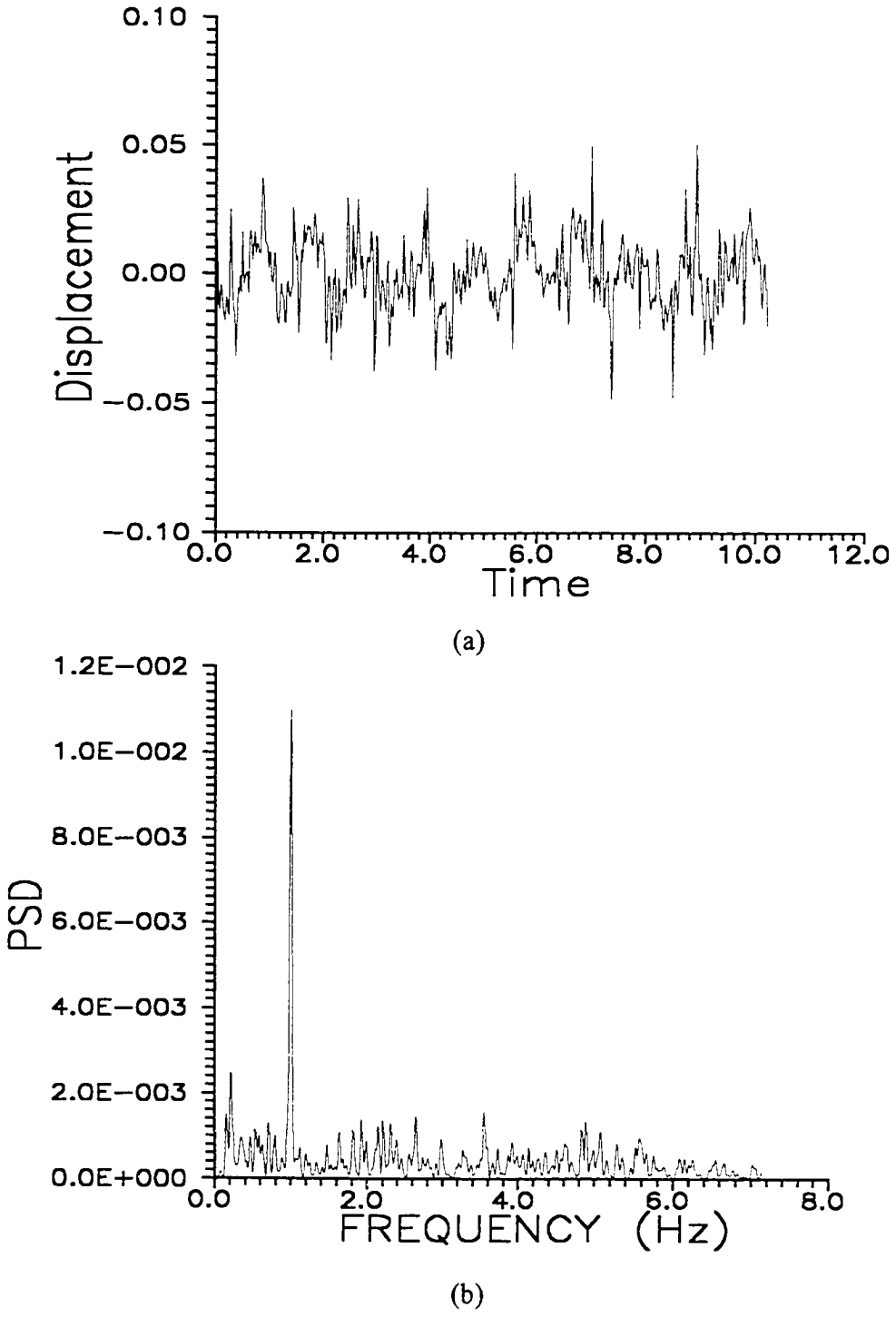

Figure 5.5 (a) Displacement at location *a* in Figure 3.8 and (b) its spectra measured when the machining system is turned on but without movements.

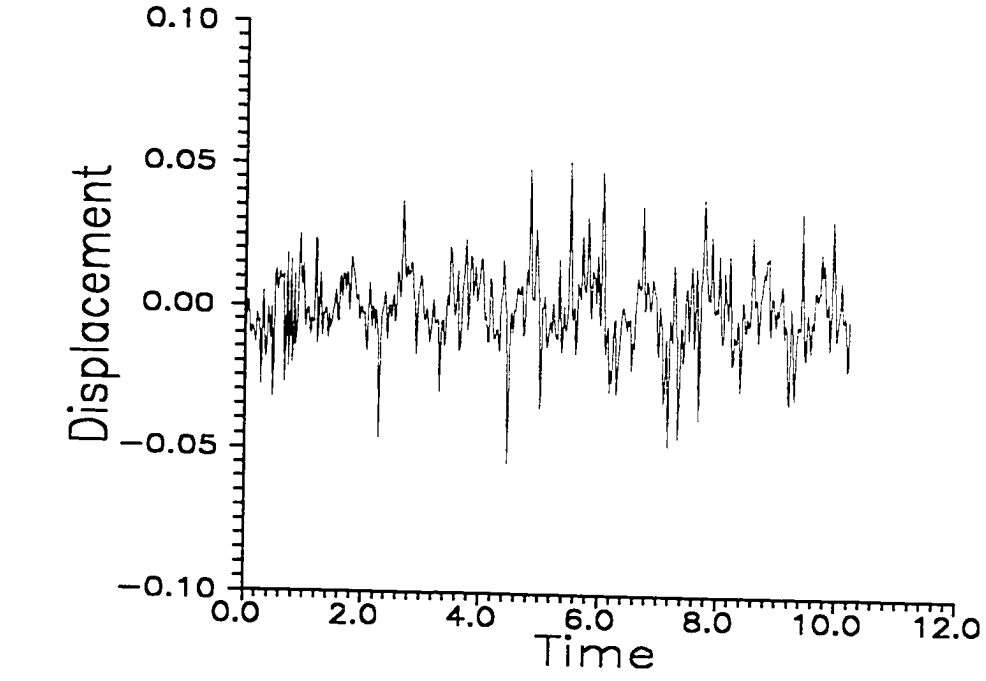

(a)

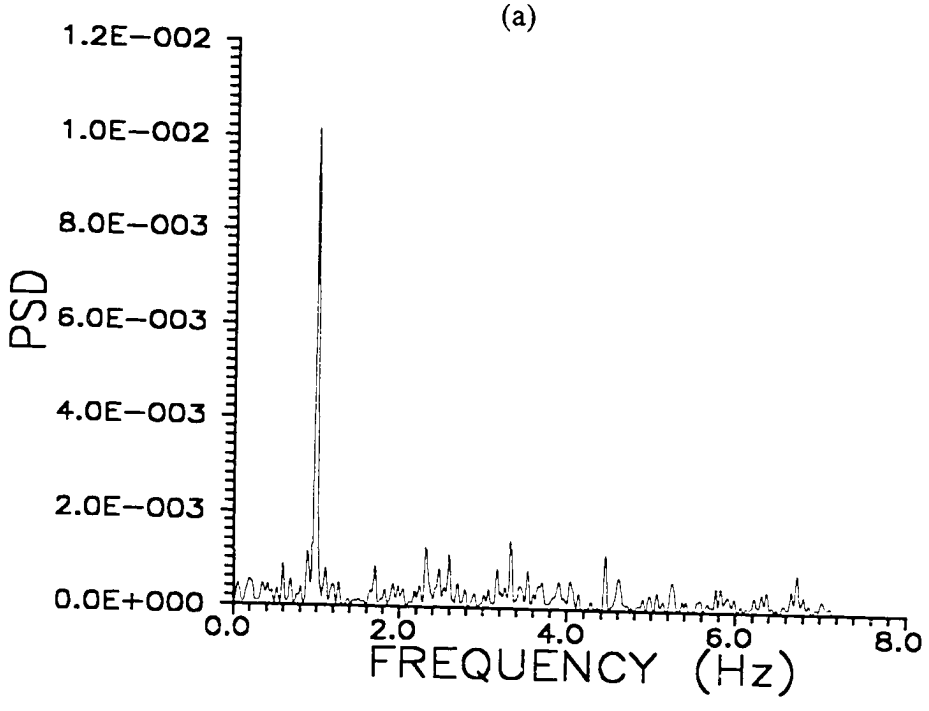

(b)

Figure 5.6 (a) Displacement at location *b* in Figure 3.8 and (b) its spectra measured when the machining system is turned on but without movements.

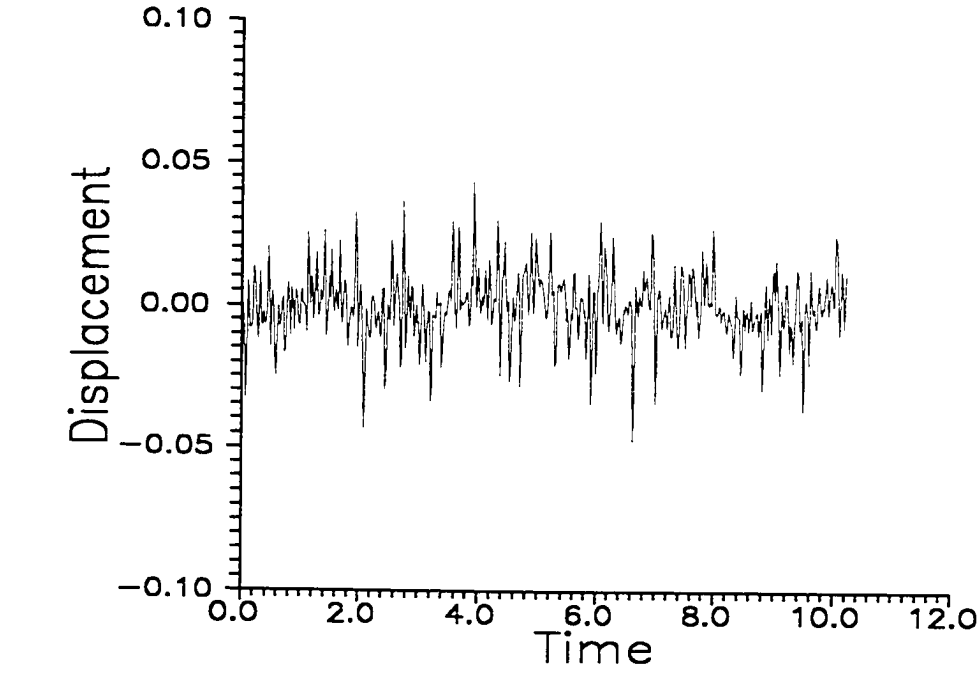

(a)

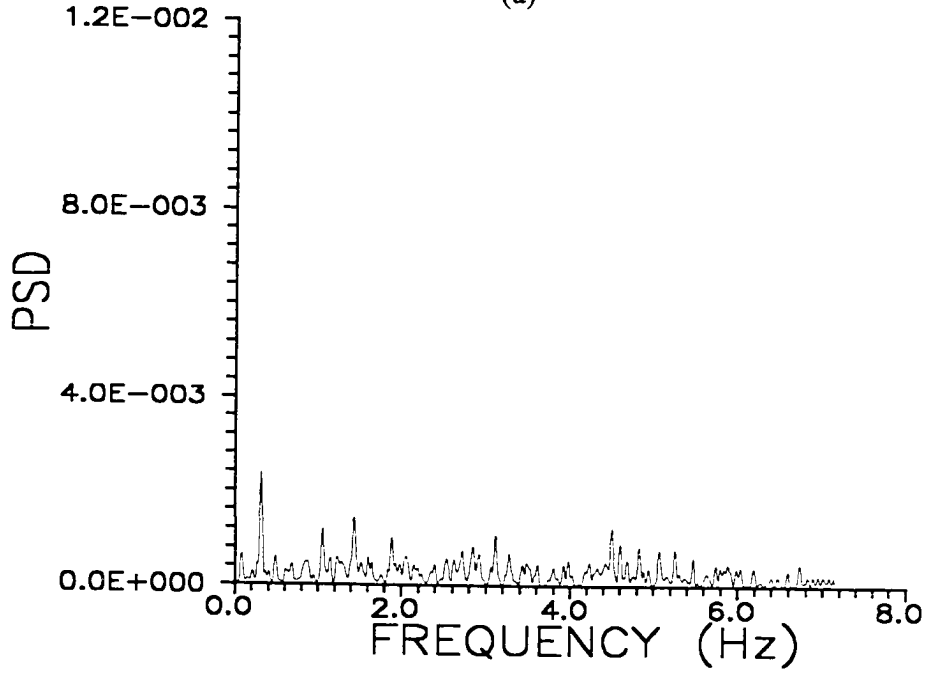

(b)

Figure 5.7 (a) Displacement at location *c* in Figure 3.8 and (b) its spectra measured when the machining system is turned on but without movements.

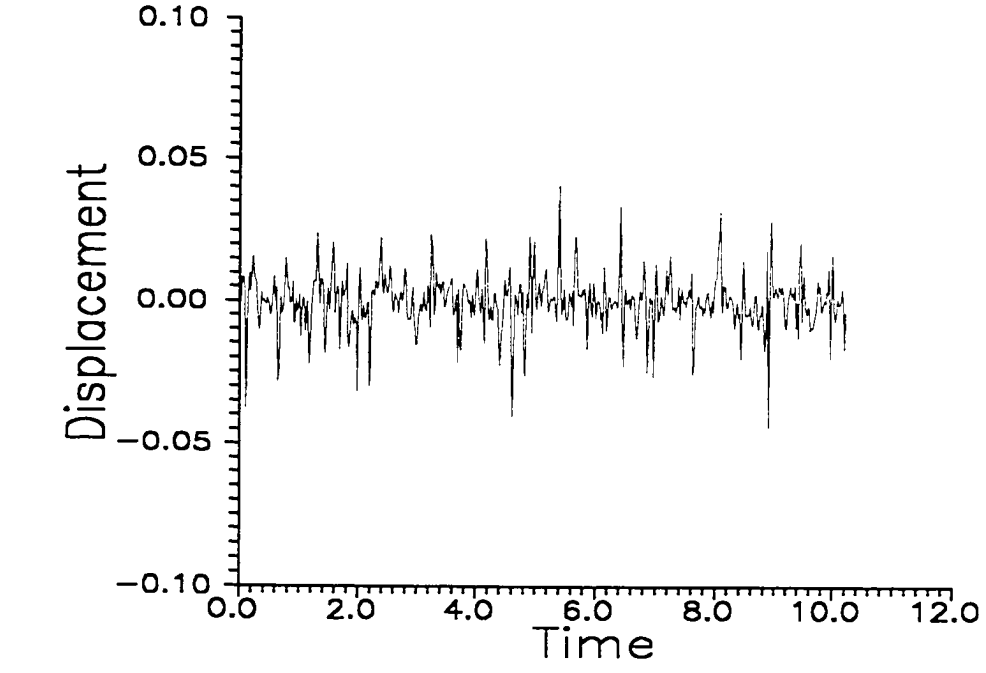

(a)

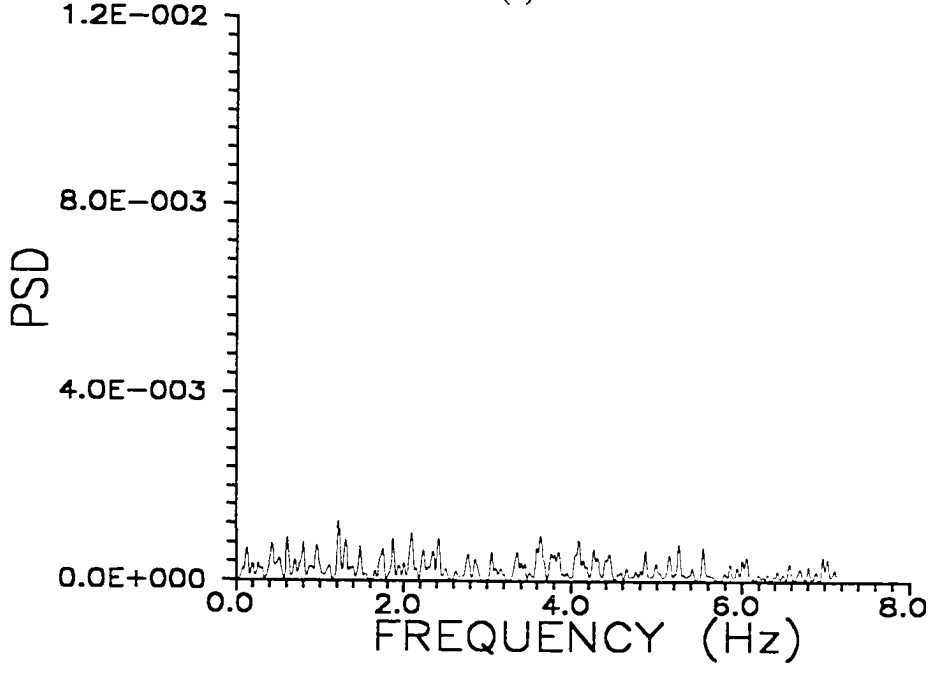

(b)

Figure 5.8 (a) Displacement at location *d* in Figure 3.8 and (b) its spectra measured when the machining system is turned on but without movements.

frequency of vibration matches the surface dominant frequency and is the main cause of the striation marks when cutting is done in the Y-direction. The 3.5 Hz frequency does not appear in the surface spectra as shown in Figure 5.2. This is probably due to the jet excitation that is orthogonal to this vibration mode.

Table 5.1 Dominant frequencies of surface spectra cut in different locations of the waterjet cutting system. Case I cut at the location (x, y, z, A, B) = (135,387,-180.71,-0.5,-180). Case II cut at the location (x, y, z, A, B) = (858,387,-179,-0.5,-180).

	Dominant Frequency (Hz)	
No.	I	II
1	1.0173	0.7452
2	0.9157	0.6112
3	0.9137	0.6173
4	0.8995	
5	0.9299	
6	0.9035	
Average	0.9124 (Hz)	0.6143 (Hz)

The vibration signal measured at the nozzle tip under machine dwell conditions was also investigated. This signal was believed to be noise in the beginning, but after turning off the drive of the traverse system the signal disappeared immediately. It was then suggested that there is a small but measurable vibration, which appears once the drive is turned on without the robot movement and without the jet flow. It was noticed also from the read-out of the LDM controller that the vibration in the X-direction has a larger amplitude (about 20 μm.) than in Y-derection and it is periodic, as shown in Figure 5.5a. It was found also that the 1 Hz frequency of the vibration signal is the dominant frequency of the vibration measured at the nozzle tip in the X-direction which matched the 1 Hz frequency measured from the modal testing as well as the surface dominant frequency, as shown in Figure 5.5b. Thus we can assume that the 1 Hz frequency measured in the modal testing experiment is not a natural

frequency of the end-effector but was some other cause and the 3.5 Hz frequency is the lowest mode of the end-effector.

Further experiments involved measuring the vibrations at three other locations with the machine in a dwell status (*b*, *c*, *d* in Figure 3.8). The plots of the displacement and the corresponding spectrum are depicted in Figures 5.6 - 5.8. The vibration that was measured at location "*b*" (Figure 5.6) shows the same dominant frequency and about the same amplitude as the vibration measured at the location "*a*" (Figure 5.5). The vibrations measured at the locations "*c*" and "*d*" (Figure 5.7 - 5.8) show much smaller amplitudes than the vibrations in locations "*a*" and "*b*" and do not have single dominant frequencies as do the vibrations in locations "*a*" and "*b*". Thus the dominant frequencies measured at locations "*a*" and "*b*" matched the dominant striation frequency when the cutting was done in the Y-direction of the waterjet machine. The power spectra of the vibration measured at locations "*c*" and "*d*" had multi-peaks. The characteristic agrees with that of the surface spectra generated when the cutting was done in the X-direction of the waterjet machine. These results clearly indicate that the cutting head vibration of force type is the main cause of striations in the waterjet machining studied.

To identify the source of the forced vibration, we examined the driving mechanism of the waterjet machining system. As shown in Figure 5.9, the motors that enabled manipulating the end-effector in X- and Y-directions were mounted on the support frame of the gantry robot, with their axes along Y-direction. The translation of the cutting head in Y direction is activated by the motor Y through a ball-screw. The cutting head translation in the X direction is activated by the motor X through a pinion-rack mechanism. The vibratory motion of the cutting head was not due to the pitch motor (which rotates the cutting head about a horizontal axis as shown in Figure 5.10) because the vibrations measured at location "*a*" and at location "*b*" were almost

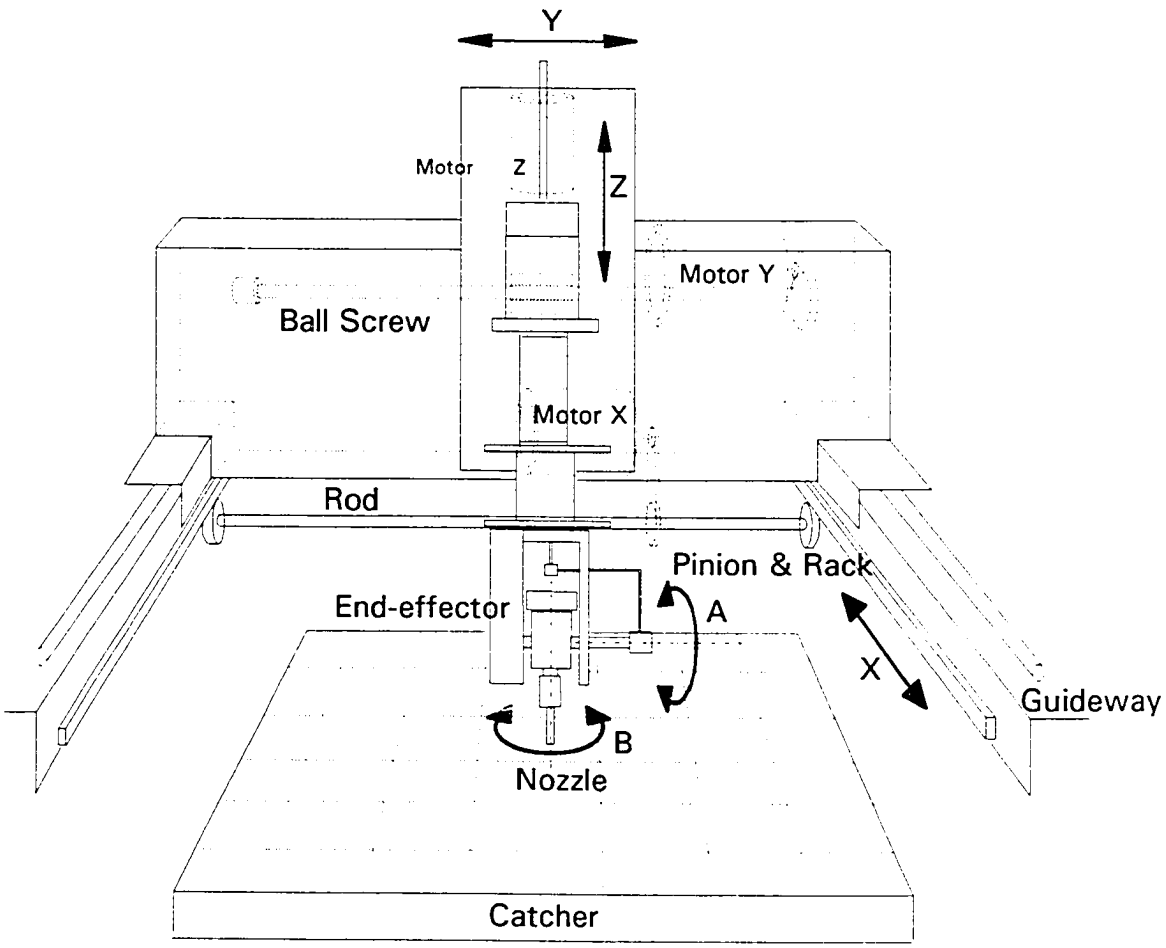

Figure 5.9 Schematic of the 5-axis robotic machining system.

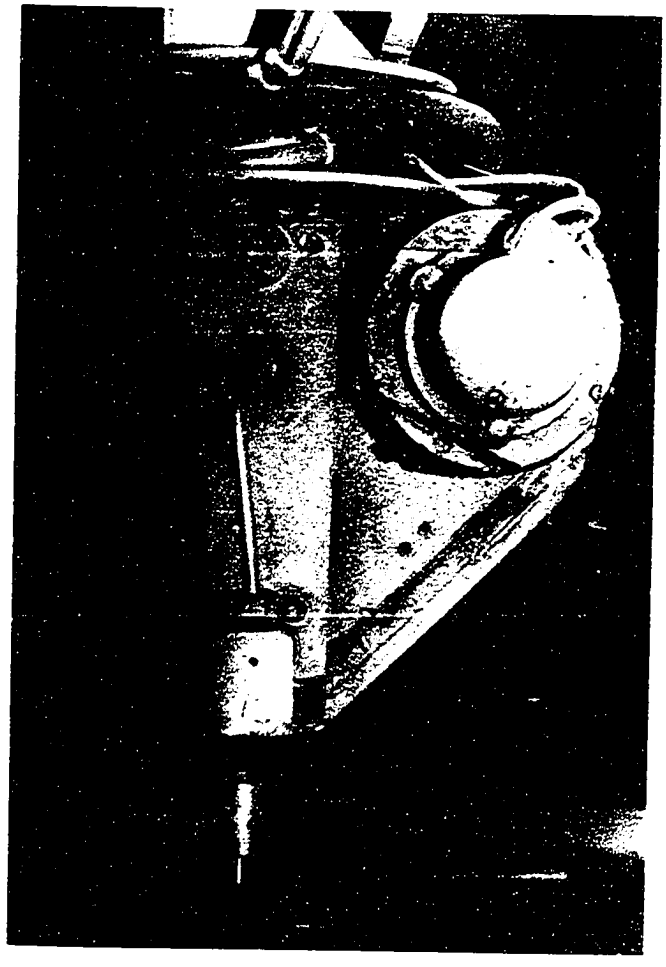

Figure 5.10 Photograph of pitch motor.

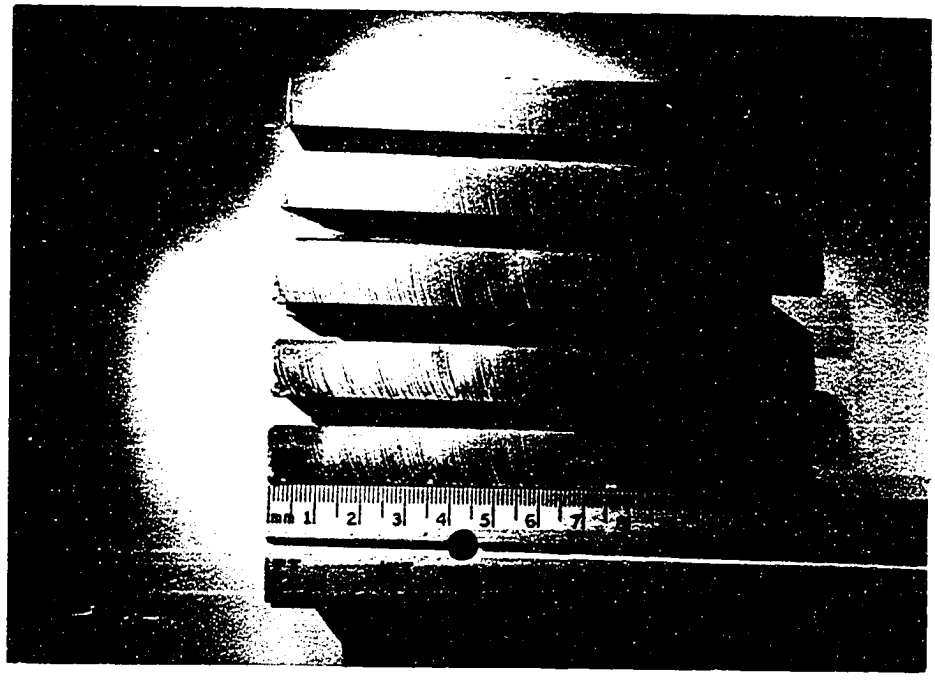

Figure 5.11 The surfaces were generated at different speeds show the striation marks with same distance apart (8 mm).

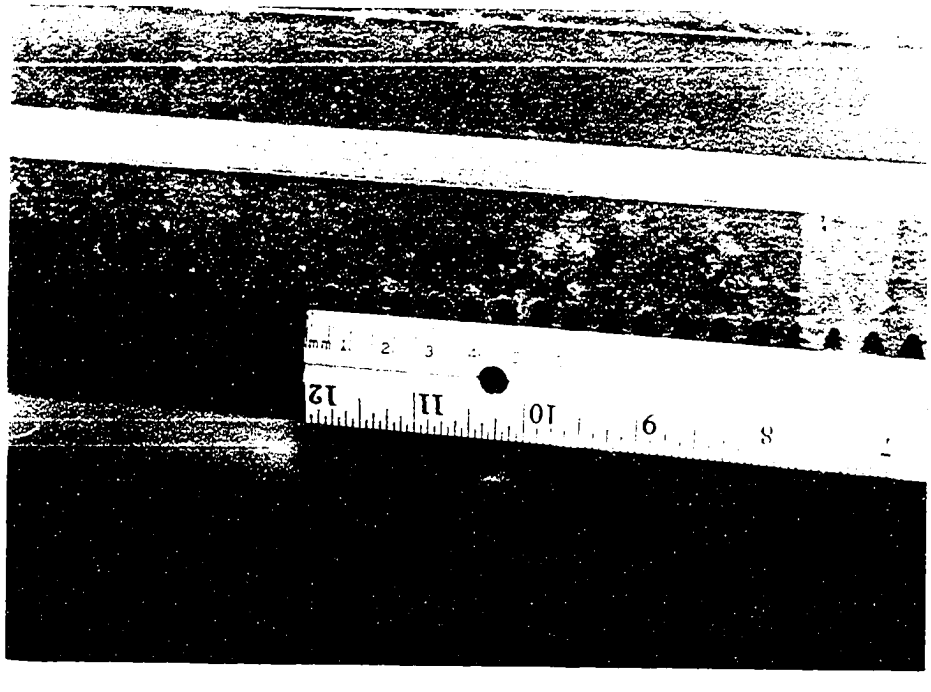

Figure 5.12 Photograph of the rack with circular pitch equal to 8 mm.

the same in magnitude. The vibration displacement at location "*a*" should have been much larger than that at location "*b*" if the pitch motor had been a main source of vibration. The roll motor (which rotates the cutting head about a vertical axis marked by B in Figure 5.9) was not a cause of the cutting head vibration for the same reason. Motor Z was not the main cause because if this were the case, then the vibration spectra measured at locations "*a*", "*b*", "*c*" and "*d*" should all have had a high degree of similarity due to the Z direction of this motor's axis. It can be concluded that motor X and motor Y are the main sources of mechanical structure vibration in the waterjet machining system used in our study. The excitations from these two motors could be due to the motor vibration in the direction perpendicular to the motor axis and/or due to the motor rotation wandering an amount corresponding to one bit of encoder measurement or digital quantization in the servo control. This knowledge of sources of the cutting head vibration is necessary in order to develop means for vibration reduction which in turn would lead to suppression of striations and improvement of surface quality.

The striation marks have the same distance apart even when cut in X-direction at different operating conditions including different workpiece materials. Figure 5.11 shows the samples cut at different speeds. All surfaces depicted in Figure 5.11 exhibit striation marks with separation equal to 8 mm. Examination of the waterjet machine showed that the pinion and rack have a circular pitch of 8 mm (Figure 5.12) which is equal to the distance between the striation marks. We can conclude now that the smoothness of the traverse system is an important factor of striation mark formation during the abrasive waterjet machining.

Figure 5.13 shows (a) the spectrum of vibration measured during cutting, (b) the surface spectrum, and (c) the frequency response function. Figures 5.14 and 5.15 shows the spectrum of vibrations and surface profiles when cutting is done in X-

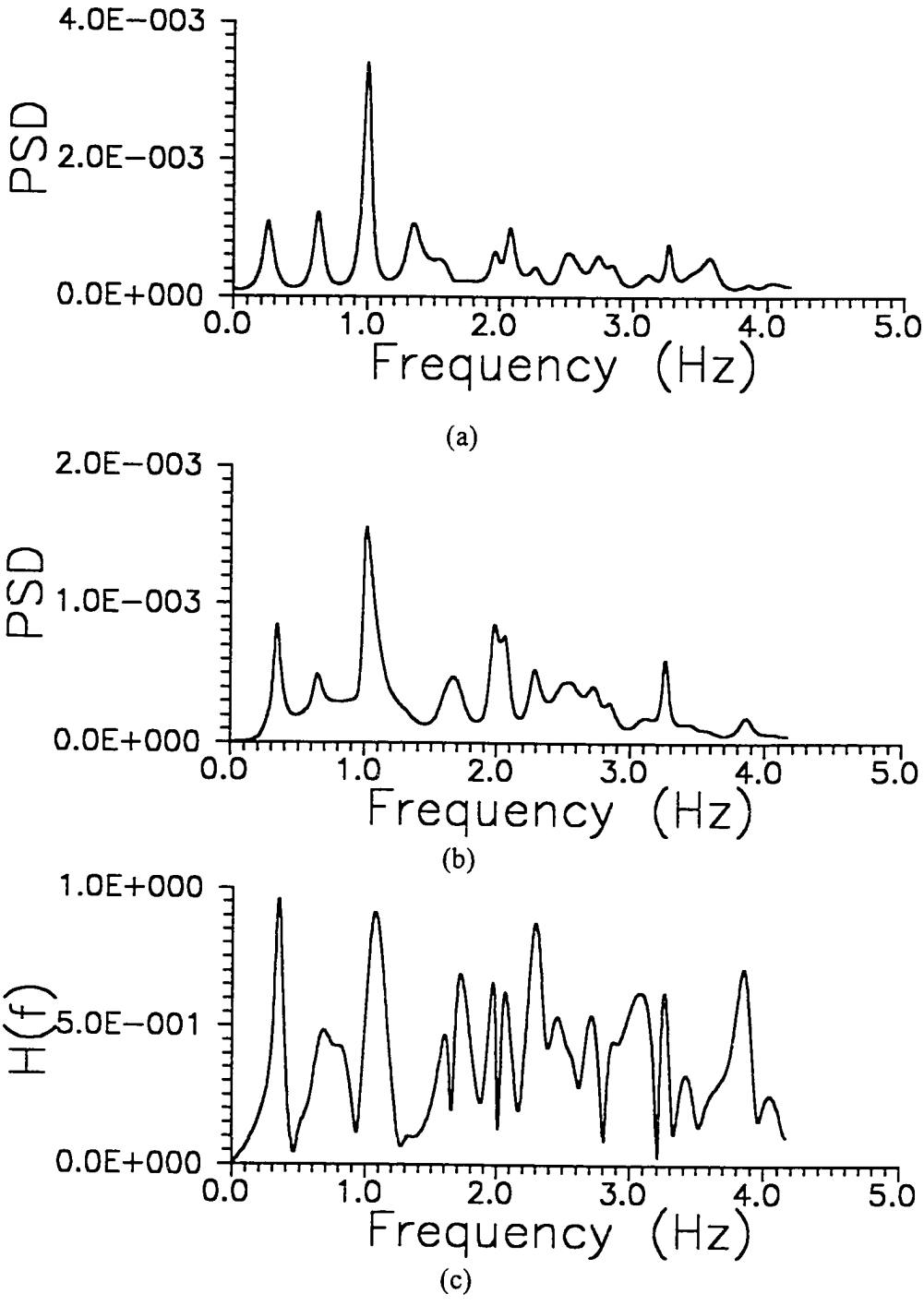

Figure 5.13 Power spectral density functions of (a) nozzle vibration, (b) surface profile, and (c) the frequency response function cut (Y-direction of the 5-axis machine).

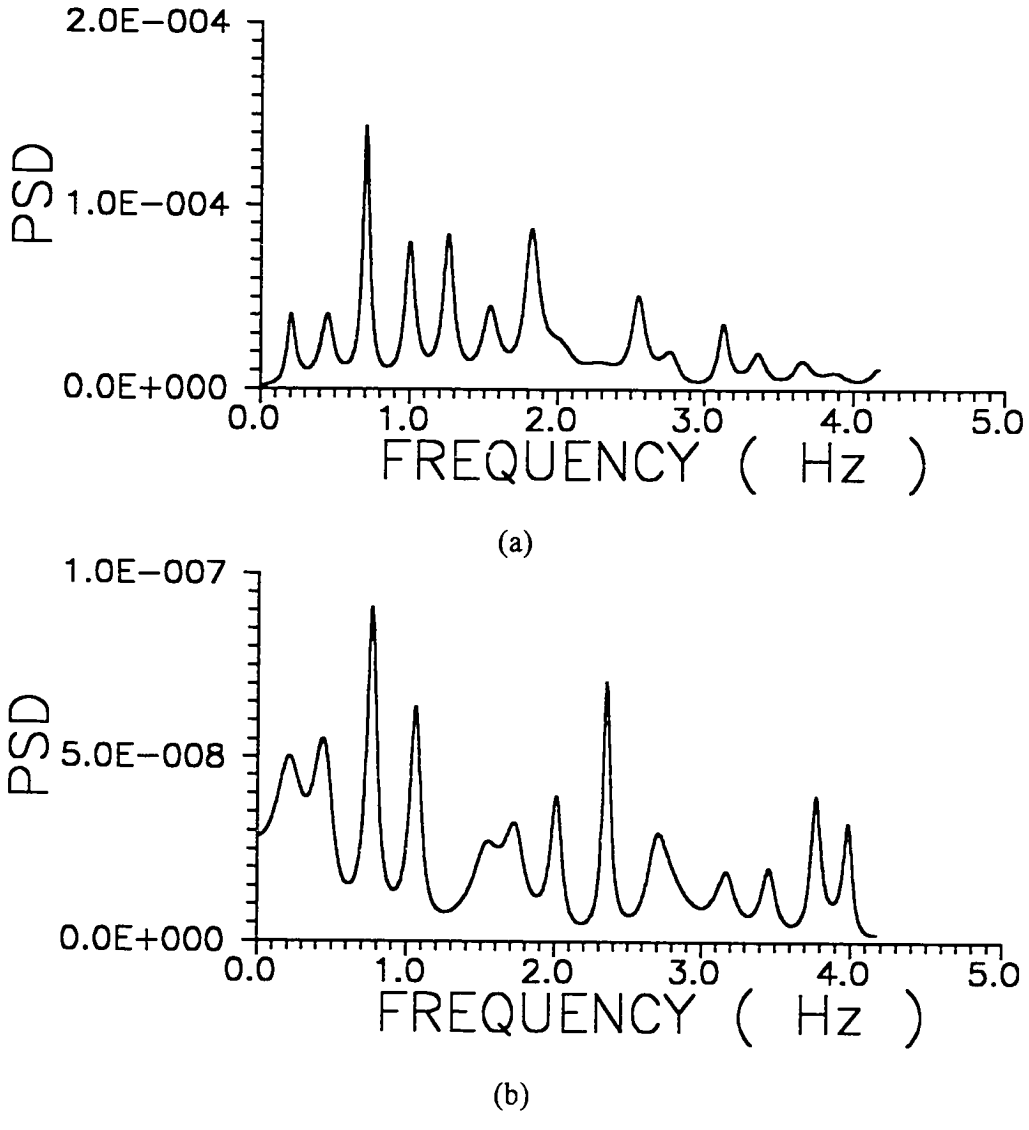

Figure 5.14 Power spectral density functions of (a) nozzle vibration, (b) surface profile, and (c) the frequency response function cut (X-direction of the 5-axis machine).

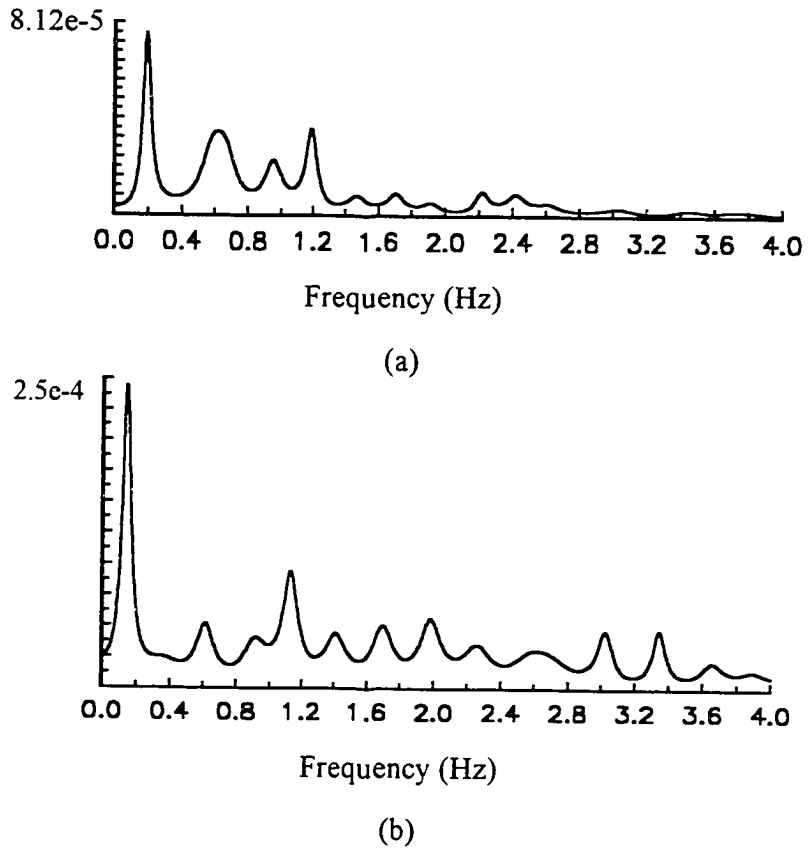

Figure 5.15 Power-spectral density of (a) nozzle vibration, and (b) surface profile, (2½ axis machine).

direction of the 5-axis and 2½-axis machine. The similarity of the surface and vibration spectra shows the strong correlation between (a) and (b).

5.4 Effect of Jet Pressure Variation on Surface Waviness

The kinetic energy of the jet, which is one of the dominant elements of cutting, is determined by the velocity of the jet and the abrasive mass flow rate [30, 31, 32]. Thus fluctuation of the jet pressure changes the jet kinetic energy with time and eventually affects the depth of cut. Figure 5.16 shows a sample that was not cut through. The frequency of variation at the bottom of cut shows a similar frequency to the jet pressure fluctuation (around 0.6 Hz). A sample shown in Figure 5.17 was cut

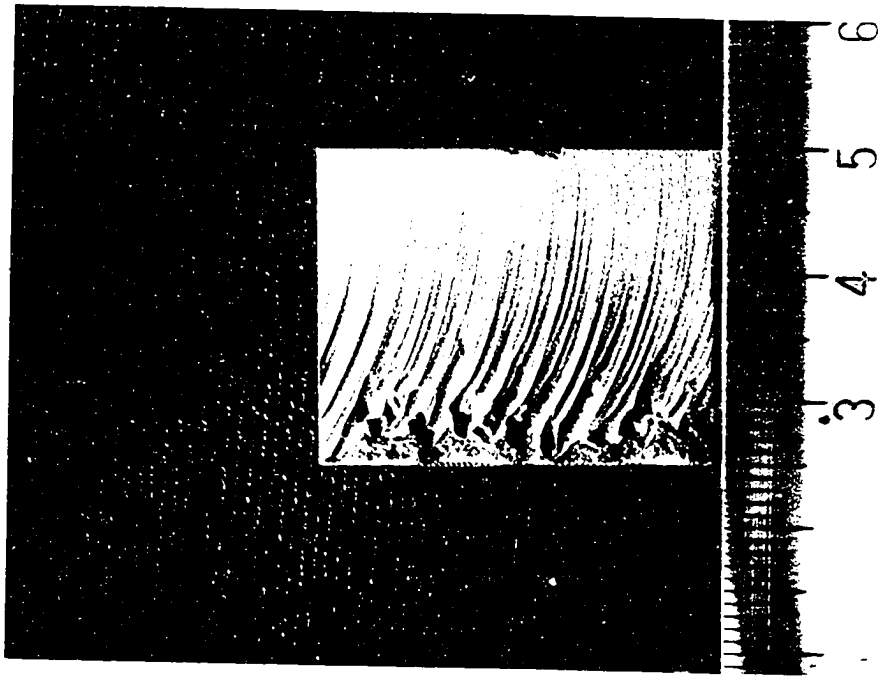

Figure 5.16 Bottom kerf geometry of a non-through cut sample.

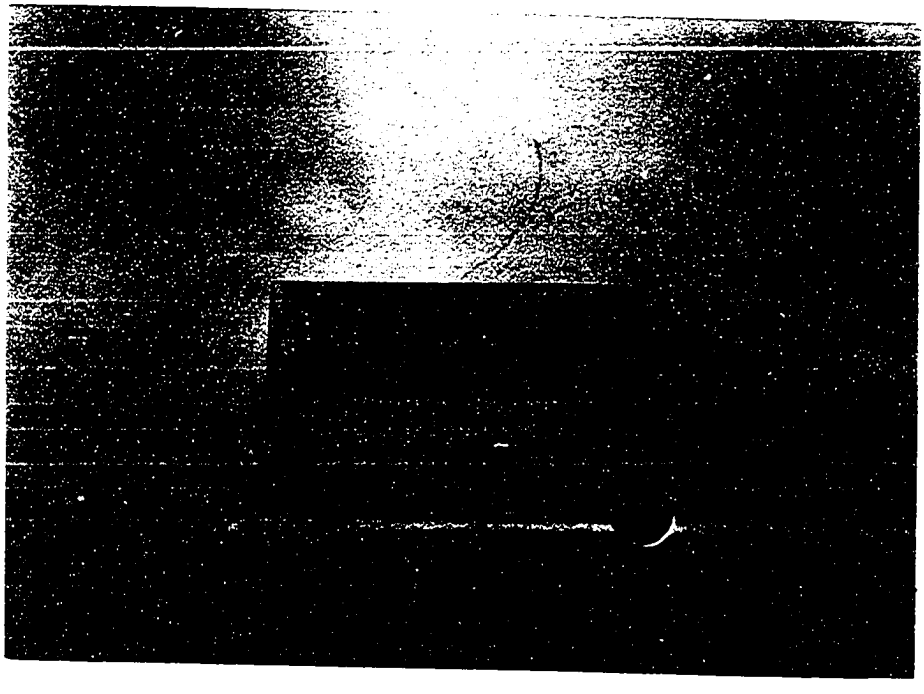

Figure 5.17 Striation marks generated by a discontinuous jet.

at a normal cutting condition but the abrasive were blocked inside the mixing chamber for two very short instances and no jet comes out from the nozzle. Two special striation marks were generated because of the discontinuity in jet pressure and the changes of the jet geometry.

In the past study of the surface spectral analysis, no significant effect of the jet pressure fluctuation on the surface waviness was found. The reason of this most probably is that the jet pressure fluctuation at the Ingersoll-Rand intensifier (about ± 5% of the operating pressure) is small related to other disturbances and does not affect substantially the jet velocity and the geometry of the jet. The fluctuation of the jet pressure has a smaller effect on the striation formation. The mixing of abrasive particles inside the mixing chamber is also one of the important factors determining the particle velocity [32, 33, 34, 35]. If the mixing is sufficient, the velocity of the abrasive particles is determined by the water velocity and the effect of the water pressure variation on the surface waviness will be stronger.

5.5 Effects of Material Properties on Surface Spectra

In this experiment, six different materials were cut at identical cutting parameters in both X and Y directions. The materials composition and the mechanical properties are given in Tables 5.2 and 5.3. The composition of the magnesium alloy was not available.

The photographs and the corresponding surface spectra of the generated surfaces are shown in Figures 5.18 - 5.21. The surface spectra of these materials were plotted in two different scales, since the value of the power spectral density functions can be roughly divided between two spans. The first group includes glass, aluminum and magnesium, easy-to machine materials having ranges of the amplitude from 0 to 4.5e-3. The second group contains hard-to-machine materials (titanium, steel and stainless-

steel) having an amplitude from 0 to 1.0e-2. The following conclusions can be drawn from the presented figures:

1. The periodical striation marks appears during cutting hard-to-machine materials as well as the easy-to-machine materials.

2. Hard-to-machine materials always have larger striation amplitude at the bottom of the generated surface.

3. The amplitude of the striation marks at any given level increases with distance from the top the cut for all the materials subjected to AWJ machining, but the hard-to-machine materials have a higher rate of increase of the striation marks than the easy-to-machine materials. The easy-to-machine materials have almost no changes in the dominant striation amplitude down to a depth of 12 mm.

4. The spectra of easy-to-machine materials show more small peaks than the spectra of hard-to-machine materials and these small peaks show a random characteristic in frequency. We believe that this is because the fracture energy of easy-to-machine materials are lower than that of hard-to-machine materials. The abrasive particles in the boundary of the jet cut the kerf edge and make small striation on the kerf edge when the workpiece material is easy-to-machine.

Table 5.2 List of chemical compositions of the materials.

ELEMENT	TYPE	CHEMICAL COMPOSITIONS (%)
Steel	AISI 1018	0.15-0.2 C; 0.6-0.9 Mn; 0.4 P; 0.05 max S; Fe
Aluminum	Al6061-T6	1.0 Mg; 0.6 Si; 0.2 Cr; 0.27 Cu; Al
Titanium	Ti-GR2	0.03 N; 0.1 max C; 0.015 max H_2; 0.3 max Fe; 0.25 max O_2; Ti
Stainless Steel	SS403	0.15 max C; 11.5-13.0 Cr; 1.0 max Mn; 0.04 max P; 0.03 max S; 0.5 max Si; Fe
Glass		80.3 SiO_2; 2.8 Al_2O_3;12.3 B_2O_3; 4.0 Na_2O; 0.4 K_2O

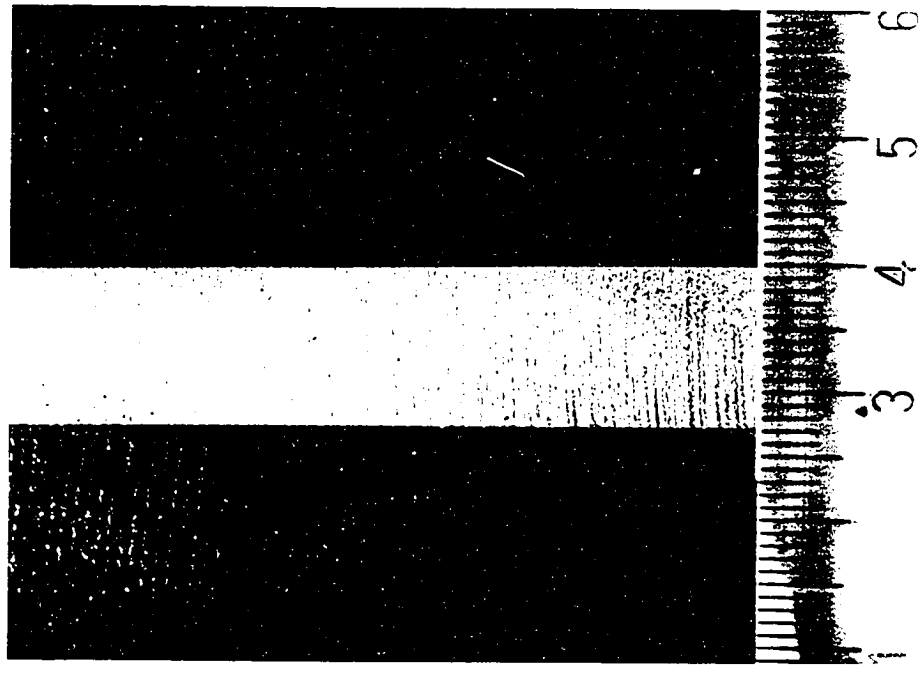

(a)

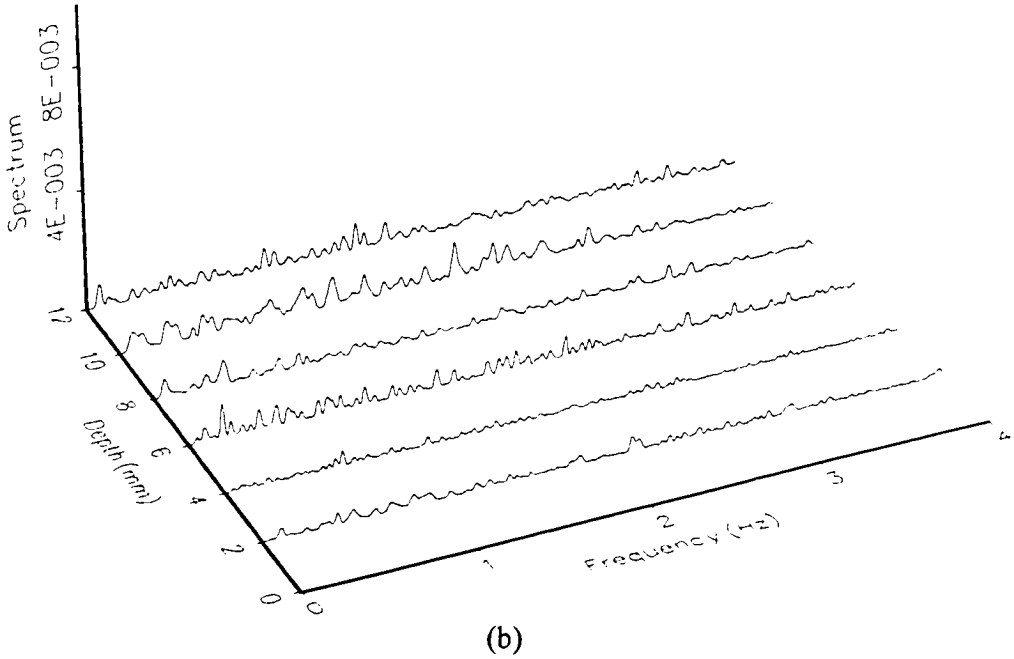

(b)

Figure 5.18 (a) Photograph of the sample, and (b) power spectral densities measured at different depths. (Steel. F=60 mm/min., Ma=226g/min., Po=345MPa, Do=0.254mm, Dt=0.838mm, X-axis.)

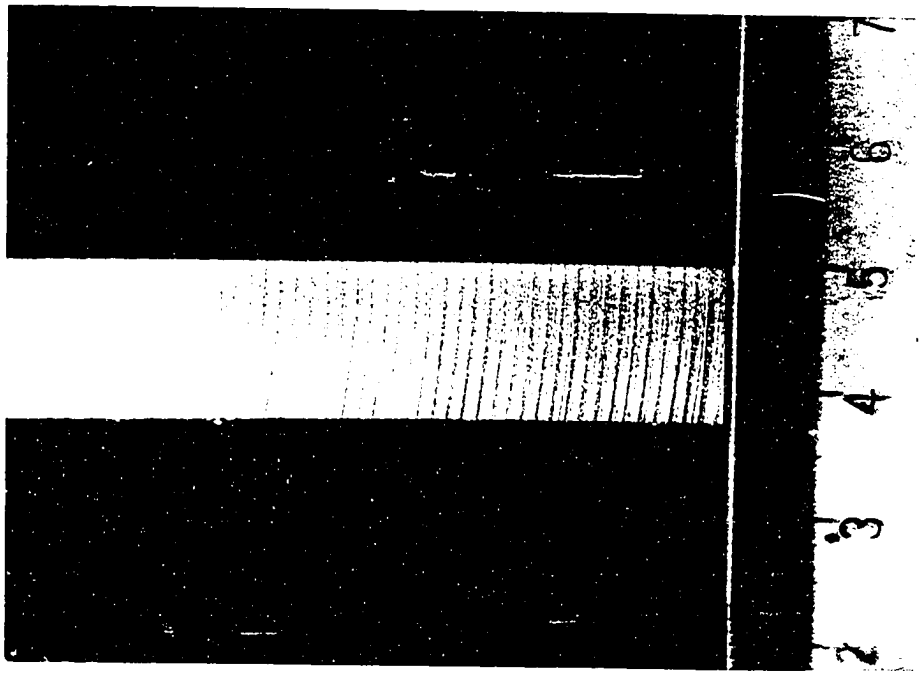

(a)

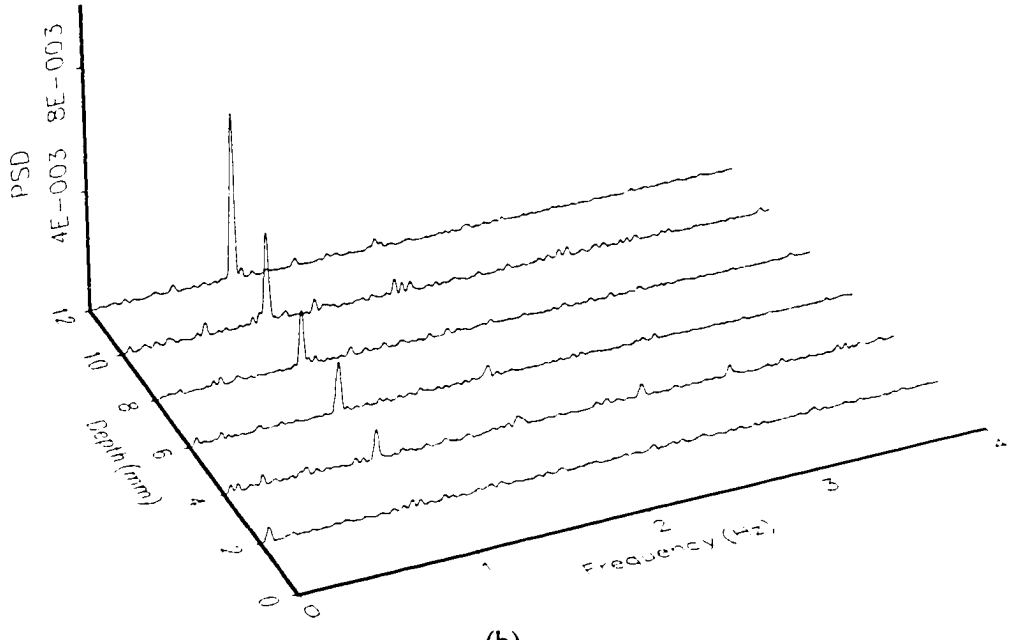

(b)

Figure 5.19 (a) Photograph of the sample, and (b) power spectral densities measured at different depths. (Steel. F=60 mm/min., Ma=226g/min., Po=345MPa, Do=0.254mm, Dt=0.838mm, Y-axis.)

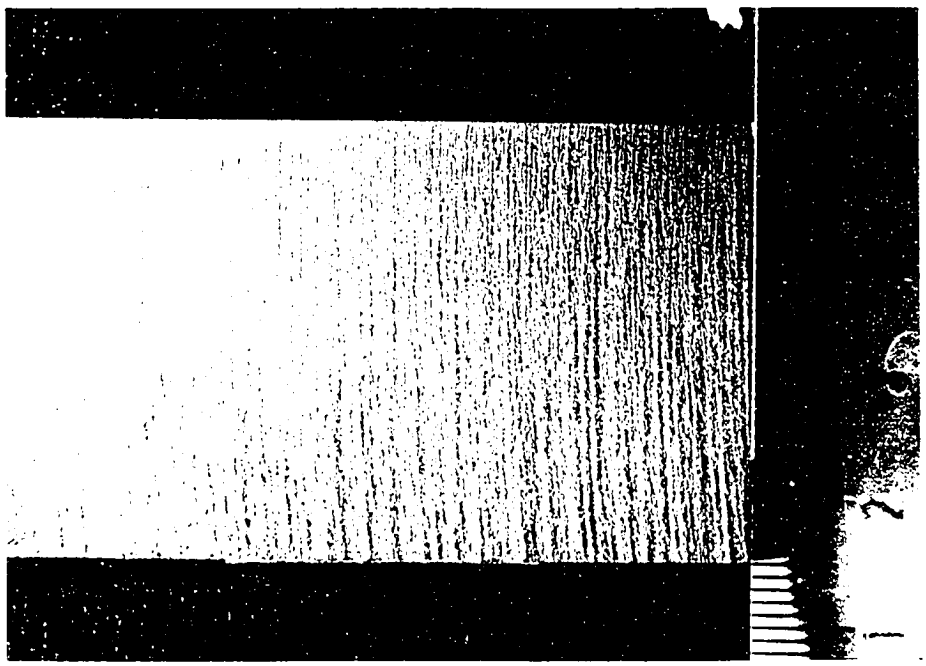

(a)

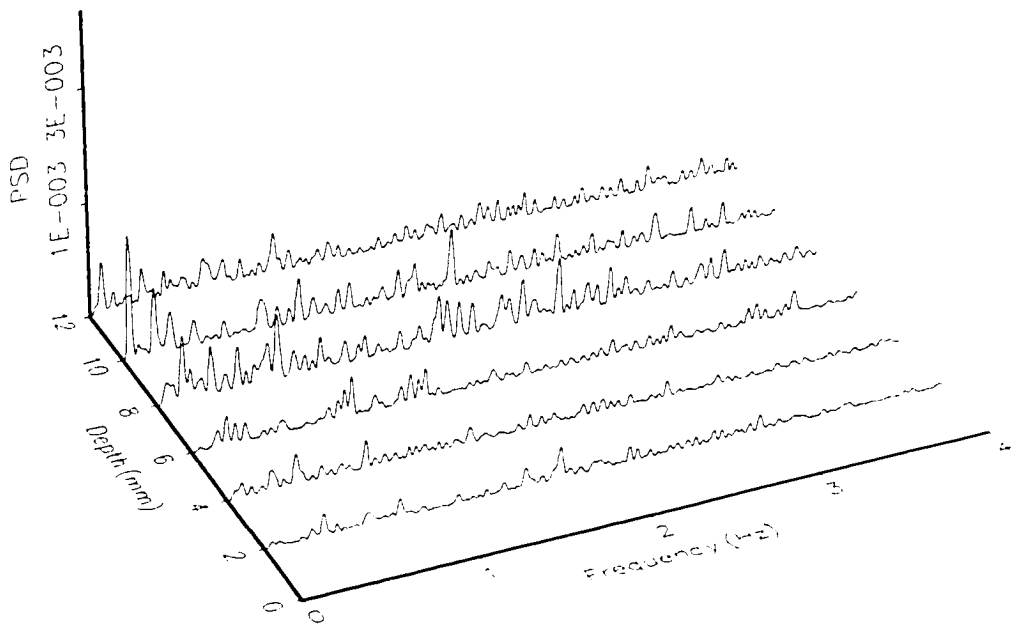

(b)

Figure 5.20 (a) Photograph of the sample, and (b) power spectral densities measured at different depths. (Magnesium. F=60 mm/min., Ma=226g/min., Po=345MPa, Do=0.254mm, Dt=0.838mm, X-axis.)

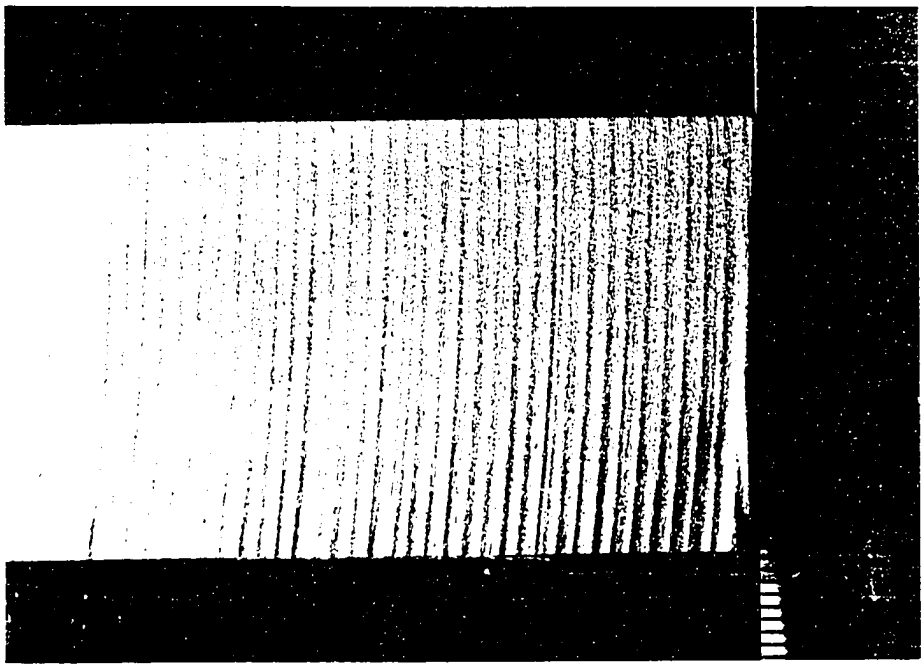

(a)

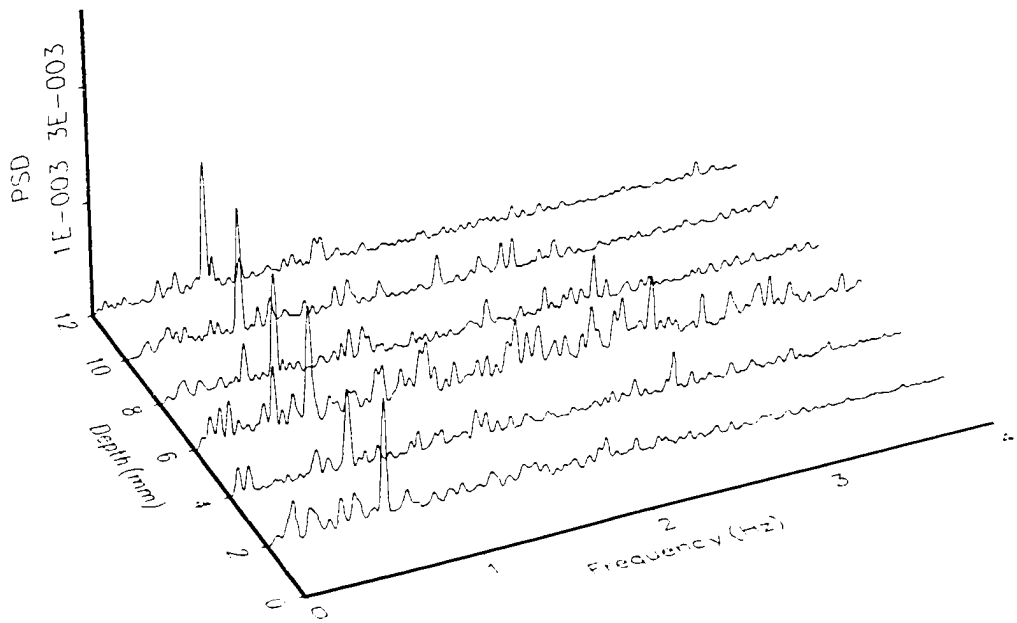

(b)

Figure 5.21 (a) Photograph of the sample, and (b) power spectral densities measured at different depths. (Magnesium. F=60 mm/min., Ma=226g/min., Po=345MPa, Do=0.254mm, Dt=0.838mm, Y-axis.)

Table 5.3 Mechanical properties of the materials.

Material	Tensile Strength (MPa)	Yield Strength (MPa)	Elongation (% in 2 in.)	Vickers Hardness
AISI 1018	450	330	36	131
AL6061-T6	310	275	17	111
TI-GR2	345	275	20	
SS403	517	276	30	
Magnesium	255	200	8	

5.6 Energy Dissipation During Waterjet Cutting Process

During abrasive waterjet cutting, as the jet penetrates deeper into the material, the jet energy dissipates thereby producing the cutting efficiency. The energy dissipates during the cutting process, thus the material removal rate decreases and the spent water flows to the back.

An important question to address is why the striations occur only will below surface. To understand this, consider that sometimes the vibration amplitude is so small that striations would not be expected to be visible. This small amplitude case corresponds to the smooth zone striation. However, deep enough in the material the spent water flows back along the already cut channel. When there is vibration, there is a sideways velocity component added to the forward motion of the moving jet. Thus the spent water has a sideways component which cuts into the side wall.

The expected result that the striation is in-phase with the amplitude of the vibration at the top and in-phase with the velocity at the bottom of the side wall and deeper, is borne outing Figure 5.22, where the non-vertical nature of the striation shows clearly.

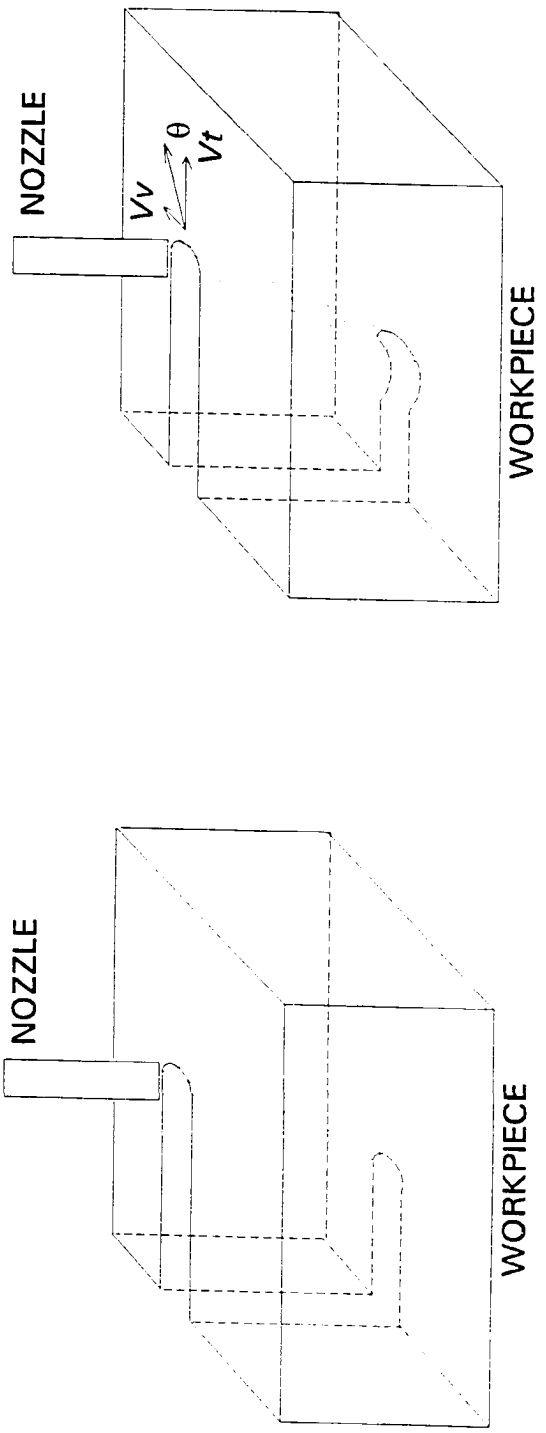

Figure 5. 22 (a) The cutting process with no vibration, and (b) cutting process with cross vibration.

The surface spectra of different materials generated at identical cutting conditions can be used to study the energy dissipation phenomena during the cutting process. For example, for hard-to-machine material, the rate of the amplitude changes along the penetration direction should be much larger than that of easy-to-machine material because the fracture energy of the hard-to-machine material is larger than the easy-to-machine material.

5.7 Effect of Jet Instability on Surface Waviness

Figure 5.23 shows a sequence of jet photographs that were shot by a high speed movie camera (filming speed 8000 frames/sec.). The white portion at the center of the jet body is the core of the jet which mainly determines material cutting. The dark portion is the boundary of the jet. The picture demonstrates the periodical flow discontinuities and variation of the jet boundary. However, the frequency of these changes is much higher then the frequency of the striation marks. We concluded that the jet instability has no effect on the striation formation.

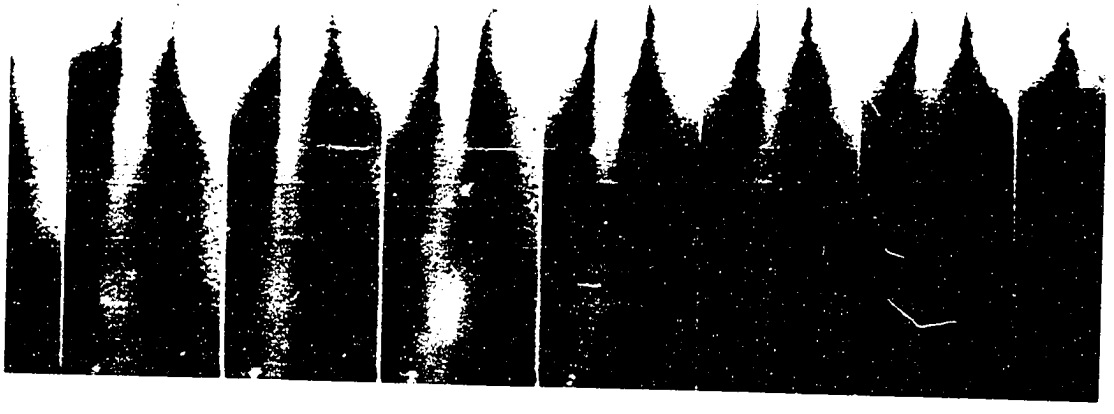

Figure 5.23 Sequence of jet pictures(filming frequency 8000 frames/sec.).

5.8 Study of Surface Profile Generated by Pure Waterjet

The surfaces generated by pure waterjet also show the striation marks on the cutting kerf edge, although the mechanism of the material removal in the pure waterjet cutting is different from that during the abrasive waterjet cutting. The obtained experimental results were used to identify the effects of the dynamic parameters on the surface generation during the waterjet cutting.

The surface spectra show multi-peaks when the cutting was carried out in the Y direction (Figure 5.24). Thus the mechanism of the striation formation in the course of pure waterjet cutting is more complicated than during abrasive waterjet cutting. The obtained results show that the fluctuation of the jet pressure has a larger effect on the surface waviness than during AWJ cutting.

The frequency of the jet pressure fluctuation measured by counting the strokes of the intensifier pump is around 0.5 Hz and is almost equal to the observed frequency of the surface spectra. For the cutting speed of 60 mm/min., the fluctuation of the jet pressure seems to be the most important factor in the striation generation because a strong peak at 0.5 Hz is observed from the surface spectra which matches the intensifier frequency. It can also be noticed that this frequency shows a very high damping ratio. This was determined by noting the bandwidth of the frequency component.

This damping factor is due to the friction between the jet and the workpiece. The appearance of the first and second harmonics of the fundamental frequency also observed from the surface spectra, means that the geometry of the jet changes (not a pure sine wave) and has a large effect on the surface waviness during the pure waterjet cutting.

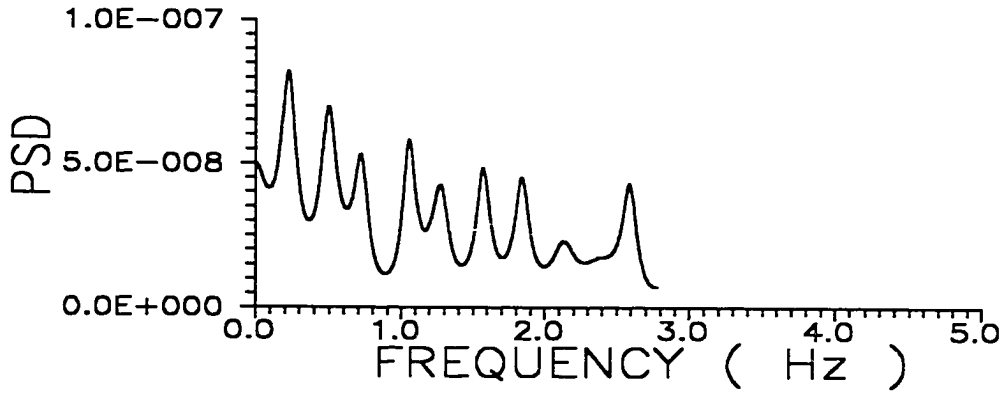

(a)

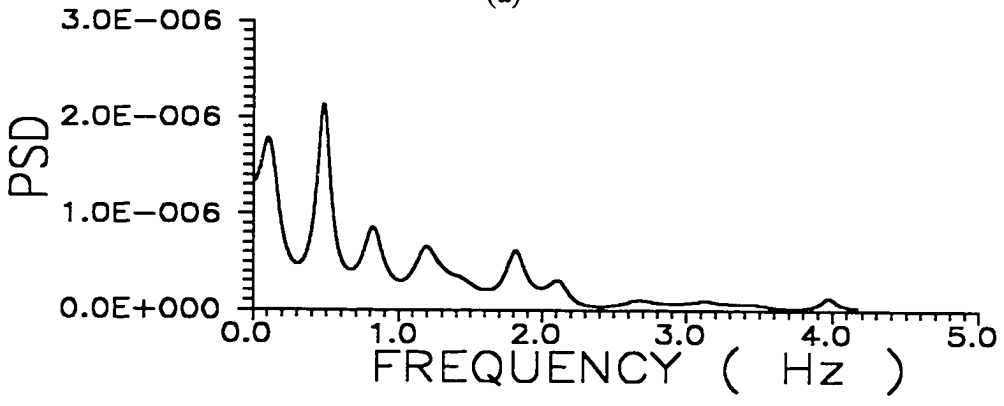

(b)

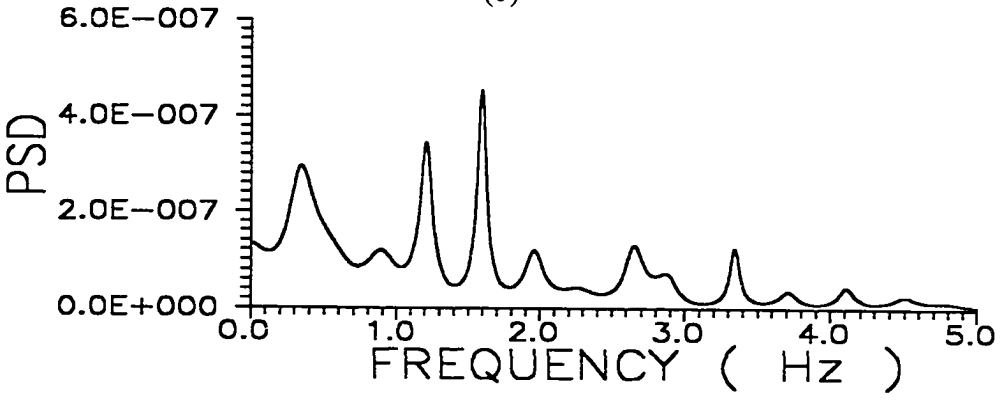

(c)

Figure 5.24 Surface spectra of aluminum plate cutting by pure waterjet at (a) 40 mm/min. (b) 60mm/min. (c) 80 mm/min.

CHAPTER 6

A MODEL OF THE KERF GEOMETRY FOR ABRASIVE WATERJET MACHINING

6.1 Introduction

Several models for prediction of the kerf geometry and the depth of cut have been constructed [1, 6, ,8, 19, 36, 37, 38, 39, 40, 41, 42, 43]. Because the knowledge of the AWJ cutting process on the microscopic level is not sufficient, most of these models were semi-empirical models. Works in [8], [19], [36], [37], and [43] concentrated on construction of models for the kerf geometry prediction. All other works were concerned with the prediction of the depth of cut. In [1] and [39], regression models for the prediction of the surface roughness were suggested. In [36], kerf shape and size were predicted by using the linear relationship between the volume removed and the kinetic energy of a single particle. However, only works [8] and [19] were concerned with surface waviness prediction. As was already discussed in Chapter 2, the physical base has not been sufficient.

The results of the previous chapter show strong correlation between the surface profiles and the nozzle vibrations. Based on these results, a model for simulation of the kerf geometry was constructed accounting for the nozzle cross vibration.

6.2 Model Development

The volume eroded by a single particle has been found to have a strong correlation with the kinetic energy of the particle [15, 16]. This relationship can be represented by the equation:

$$\delta v = c \cdot e_k \tag{6.1}$$

where δv is the volume removed by a single particle, e_k is the kinetic energy of a particle. Equation (6.1) enables us to assume that the depth of cut by a single particle is also proportional to its kinetic energy. For the erosion by a particle stream, [44] and [43] claimed that it has the same characteristics as the erosion by a single particle. Therefore, the actual material removal by a stream of particles can be approximated through the superposition of the material removal by individual particles. This assumption was demonstrated in [45]. The depth of cut by N particles during a time interval t is given by :

$$z = k \cdot N \cdot t \cdot e_k \tag{6.2}$$

where t is the duration of the particles impacting on a unit area, N is the amount of particles impinging a unit area in a unit time, given by:

$$N = \frac{M_a}{\pi \cdot R_j^2 \cdot 60} \tag{6.3}$$

where M_a is the abrasive mass flow rate (g/min.), R_j is the jet radius.

Now considering as the jet moves forward a distance Δx, the sideways velocity V_y due to the vibration causes the jet moves a distance along the Y-direction as shown in Figure 6.1. The distance $n \cdot \Delta y$ is given as follows:

$$n \cdot \Delta y = V_y \cdot \Delta t = V_y \cdot \frac{\Delta x}{F} \tag{6.4}$$

The coordinate of the jet center moves from $(x_c,\ y_c)$ to $(x_c + \Delta x,\ y_c + n \cdot \Delta y)$ during the time interval Δt, and the depth of cut within the jet effective zone increases by Δz. The Δz is given as:

$$\Delta z = k \cdot N \cdot \Delta t \cdot e_z \tag{6.5}$$

where e_z is energy involved in the material erosion by a single abrasive particle at the depth z.

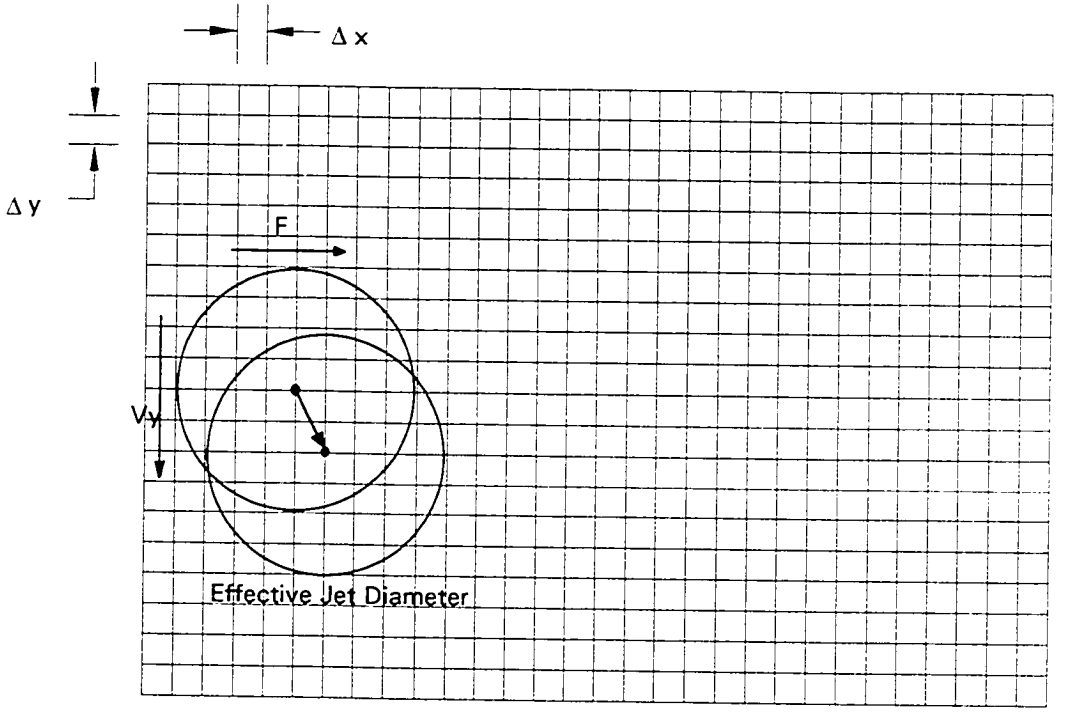

Figure 6.1 Meshes of the target material and effective jet diameter

The energy dissipation of a penetrating jet is a complex phenomenon that has not been completely investigated and understood yet, and therefore can not be represented by a physical model. A function $\eta(z)$ can be used to describe the energy dissipation phenomenon which is due to the interaction among particles, and the influence of the turbulent flow. The function is given as:

$$\eta(z) = \frac{1}{1+z} \tag{6.6}$$

It can be seen that $\eta(z)$ is a monotone decreasing function. At z=0, $\eta(z)$ is 1. The energy involved in the material removal e_z can be related to the particle kinetic energy at the nozzle exit e_k. Equation (6.5) can be written as:

$$\Delta z = k \cdot N \cdot \Delta t \cdot \eta(z) \cdot e_k \tag{6.7}$$

The new depth of cut inside the effective jet diameter is $z(x, y)+\Delta z$. Figure 6.2 shows the simulation flow chart. The result of the process modeling using the constructed equation is depicted in Figure 6.3.

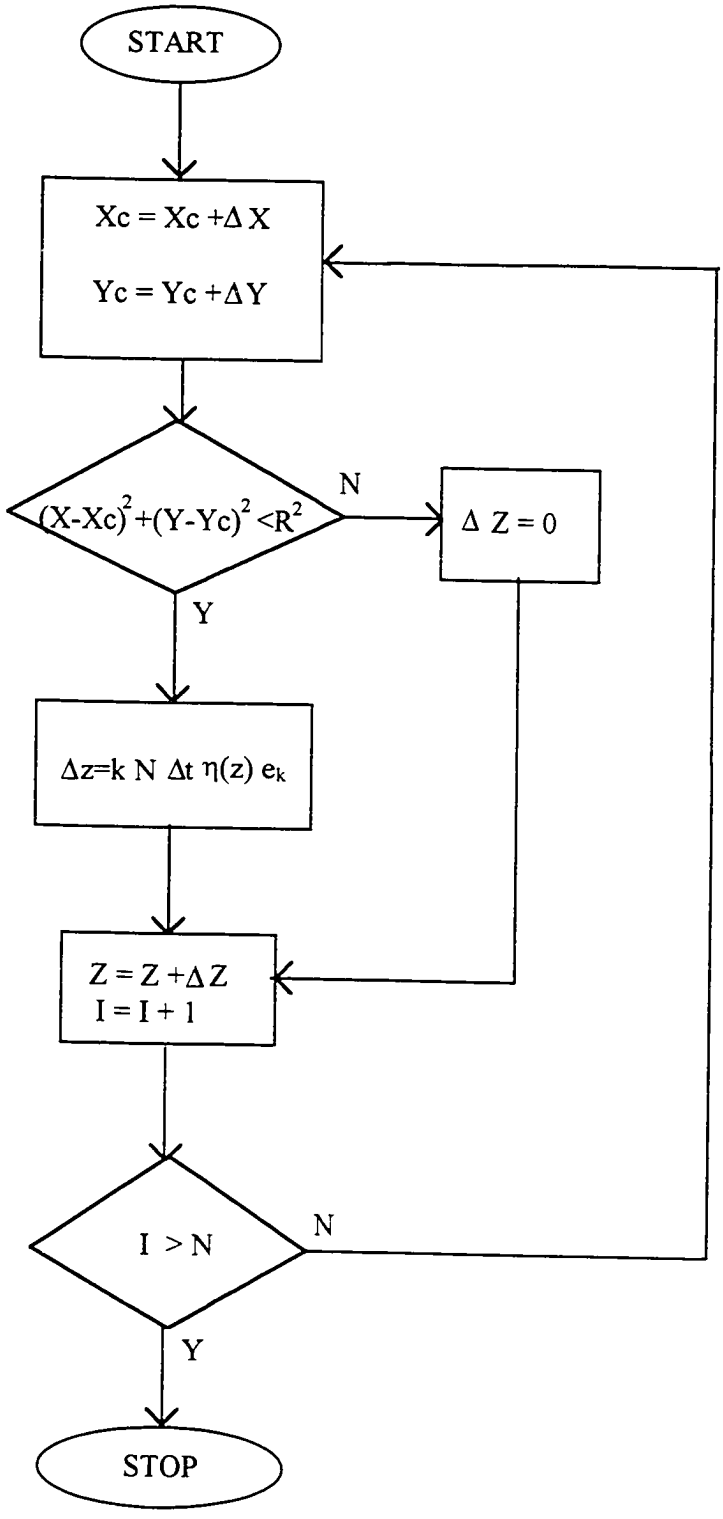

Figure 6.2 Simulation flow chart.

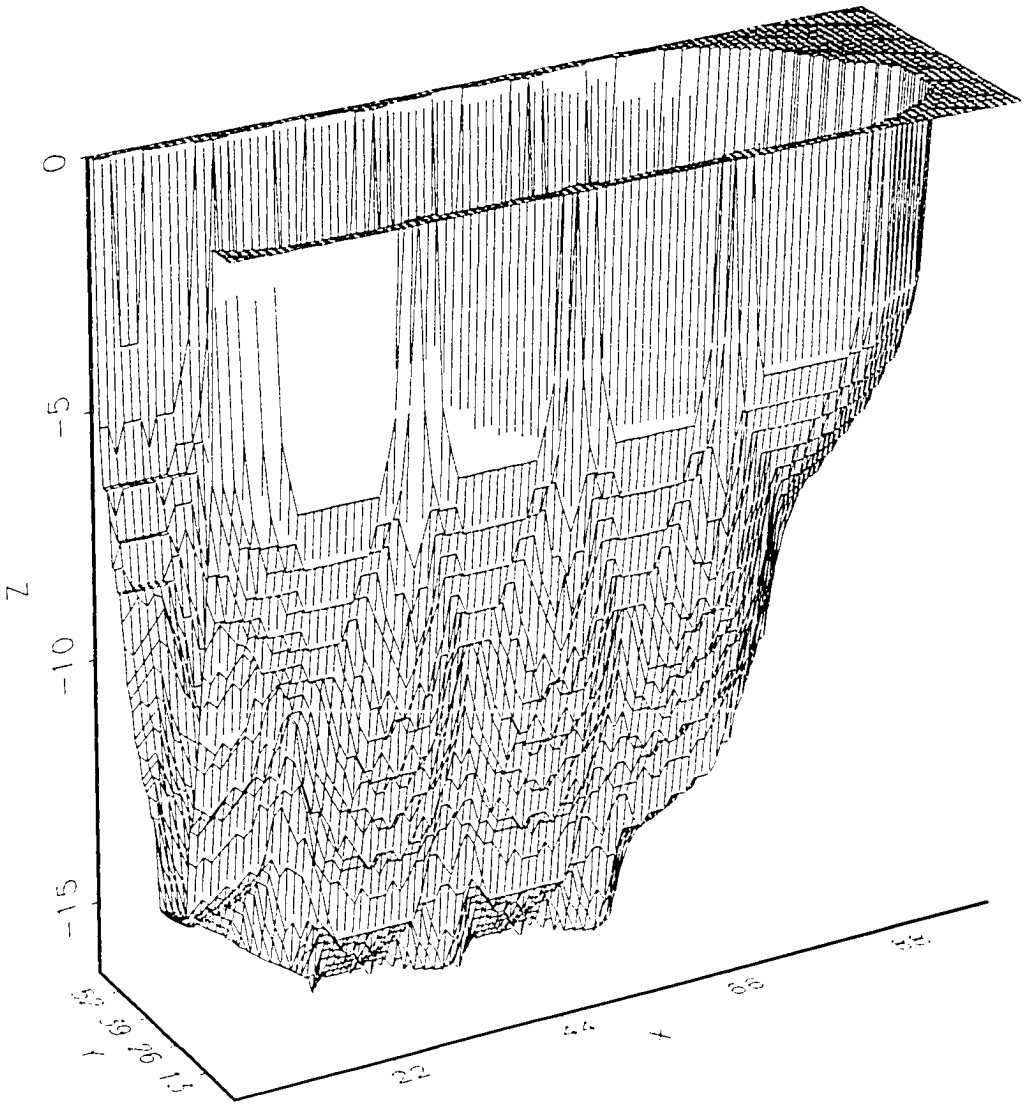

Figure 6.3 Kerf geometry in AWJ machining.

CHAPTER 7

CONCLUSIONS AND RECOMMENDATIONS

7.1 Conclusions

The spectral analysis of the topography of the surface generated by AWJ determines the frequency characteristics of these surfaces. The AWJ generated surface may not contain distinctive regions. The differences between various regions are qualitative. The surface spectra show strong correlation with the structure dynamics of the traverse system. The jet-induced waviness has not been observed in our study. The amplitude of the striation marks is a second-degree polynomial function of the distance from the top of cut and is also a function of speed.

The different materials cut with the abrasive waterjet under identical cutting conditions show different surface spectra. For the hard-to-machine materials, the surface topography is smoother but larger in amplitude than that of the easy-to-machine material.

The effect of the jet pressure fluctuation on the surface topography is insignificant, because the pressure variation is small for our condition. The mixing of abrasive particles inside the mixing chamber is also one of the important factors determining the particle velocity. If the mixing is sufficient the velocity of the abrasive particles is determined by the water velocity and the effect of the water pressure variation on the surface waviness will be stronger.

The dynamic test of the traverse system enables us to determine the real dynamic characteristics of the system which are helpful for the understanding of the striation formation in abrasive waterjet machining. The obtained results show that the vibration plays an important role in the striation formation. The driving motors and the gear/pinion transmission system were identified as the vibration sources in the

waterjet machining system. The straightness of the kerf edge is affected by the accuracy of the waterjet machining system. This knowledge of the sources of the cutting head vibration is useful for development of means for vibration reduction, which would lead to suppression of striations and improvement of surface quality.

A three-dimensional cutting kerf geometry is reproduced by a model which assumes that the depth of cut to be proportional to the jet kinetic energy. Due to the existence of the cross vibration, the striation marks appear on the kerf edge.

7.2 Further Research

For a complete understanding of the mechanism of the striation formation in abrasive waterjet machining, the following studies are necessary:

1. The fluctuation of the jet pressure was proved to have less effect on the surface topography because the jet pressure is quite stable in our system. It is necessary to study the effect of jet with larger fluctuation on the surface topography. This can be accomplished by disconnecting the accumulator from the system.

2. The distribution of the abrasive particles.

3. Fluid dynamics of the slurry jet, especially inside the mixing chamber and after the carbide tube.

4. Theoretical study of the mechanism of material removal in AWJ.

7.3 Process Improvement

To remedy the dimensional inaccuracy induced by the traverse system that causes the striation on the kerf edge, the vibration isolation of the cutting head and the redesign of the driving motor's mounting system are necessary. The adaptive control of the nozzle vibration is also an effective way of solving this problem.

APPENDIX I

FORTRAN PROGRAM (DSP) FOR CALCULATING THE POWER SPECTRAL DENSITY FUNCTION

```
      PROGRAM DSP
      DIMENSION Z(550),Z1(550)
      DIMENSION GK(1024),XREAL(2048),XIMAG(2048)
      REAL MEAN,NYQ
      INTEGER DN
C
C     INPUT :
C
C             Z(I)   : SAMPLED FUNCTION
C             ND     : SAMPLE SIZE
C             N      : ANALYSIS SAMPLE SIZE
C             DX     : SAMPLING INTERVAL
C             M      : NUMBER OF FREQUENCY COMPONENTS USED TO
C                      SMOOTHING
C             PP     : THE RATIO OF THE CUT-OFF FREQUENCY TO
C                      NYQUEST FREQUENCY
C             CS     : CUTTING SPEED
C             IFL = 1 : SURFACE PROFILE
C             IFL = 2 : VIBRATION
C
C
C     OUTPUT :
C
C             GK     : AUTO-SPECTRUM
C
C
C     INPUT DATA
C
      PI=3.1415927
      OPEN(10,FILE='data1')
      OPEN(11,FILE='data2')
      OPEN(13,FILE='topo1.dat')
      OPEN(12,FILE='AUTOPSD.DAT')

      READ(10,*)ND,DX,N,IFL,CS,M,PP
      DO 10 I=1,ND
      READ(11,*)Z(I)
10    CONTINUE
      DN=ND-N+1
```

```
      IF (IFL .EQ. 1) THEN
        T=DX*60.0/CS
        DO 12 I=1,ND
12      Z(I)=Z(I)*25.4
      ELSEIF (IFL .EQ. 2) THEN
        T=DX
      ENDIF
C
C     NYQUEST FREQUENCY
C
      NYQ=0.5/T
      CUT=NYQ*PP
      DO 15 I=1,1024
15    GK(I)=0.0

      DO 75 IJK=1,DN
C
C     REMOVE LINEAR TREND USE LEAST SQUARE METHOD
C
      DO 16 I=1,2048
      XREAL(I)=0.0
      XIMAG(I)=0.0
16    CONTINUE

      DO 20 I=1,N
      Z1(I)=Z(IJK+I-1)
20    CONTINUE

      CALL RLT(N,T,Z1,B0,B1)
C     WRITE(*,*)B1,B0

      DO 35 I=1,N
      Z1(I)=Z1(I)-B0-B1*T*FLOAT(I-1)
35    CONTINUE

C     FILT-OUT THE FREQUENCIES ABOVE THE NYQUEST FREQ.

      CALL LOWPASS(Z1,CUT,T,N)

C     ZERO MEAN

      AMOUNT=0.0
      DO 40 I=1,N
      AMOUNT=AMOUNT+Z1(I)
```

```
40   CONTINUE
     MEAN=AMOUNT/FLOAT(N)
     DO 50 I=1,N
     Z1(I)=Z1(I)-MEAN
     WRITE(13,*)DX*(I-1),Z1(I)
50   CONTINUE

C    WINDOWS ( COSINE TAPER DATA WINDOW )

     DO 60 I=1,N
     XREAL(I)=0.0
     IF ( I .LT. N/10 ) THEN
          XREAL(I)=0.5*Z1(I)*(1.0-COS(10.*PI*I/N))
     ELSEIF ( I .GT. 9*N/10 ) THEN
          XREAL(I)=0.5*Z1(I)*(1.0+COS(10.*PI*(I-9*N/10)/N))
     ELSE
          XREAL(I)=Z1(I)
     ENDIF
     XIMAG(I)=0.0
60   CONTINUE

C    FFT

     CALL FFT(XREAL,XIMAG,2048,11)
     DO 70 I=1,1024
     GK(I)=GK(I)+2.0*(XREAL(I)**2+XIMAG(I)**2)*DX/(2048**2/N)
70   CONTINUE
75   CONTINUE
C
C    FREQUENCY SMOOTHING
C
     CALL SMOOTH(GK,1024,M)
C
C    OUTPUT
C
     DO 80 I=1,1024
     FK=(I-1)/(T*2048)
     WRITE(12,*)FK,GK(I)
80   CONTINUE

     CLOSE(10)
     CLOSE(11)
     CLOSE(12)
     STOP
     END
```

```
      SUBROUTINE RLT(N,DX,Z1,B0,B1)
      REAL Z1(1),NU
      U=0.0
      NU=0.0
      DO 10 I=1,N
      U=U+Z1(I)
      NU=NU+I*Z1(I)
   10 CONTINUE
      B0=(2.0*(2.0*N+1.0)*U-6.0*NU)/(N*(N-1.0))
      B1=(12.0*NU-6.0*(N+1)*U)/(DX*N*(N-1)*(N+1))
      RETURN
      END

      SUBROUTINE FFT(XREAL,XIMAG,N,NU)
      DIMENSION XREAL(1),XIMAG(1)
      N2=N/2
      NU1=NU-1
      K=0
      DO 30 L=1,NU
   10   DO 20 I=1,N2
        P=IBITR(K/2**NU1,NU)
        ARG=6.283185*P/FLOAT(N)
        C=COS(ARG)
        S=SIN(ARG)
        K1=K+1
        K1N2=K1+N2
        TREAL=XREAL(K1N2)*C+XIMAG(K1N2)*S
        TIMAG=XIMAG(K1N2)*C-XREAL(K1N2)*S
        XREAL(K1N2)=XREAL(K1)-TREAL
        XIMAG(K1N2)=XIMAG(K1)-TIMAG
        XIMAG(K1)=XIMAG(K1)+TIMAG
   20   K=K+1
      K=K+N2
      K=0
      NU1=NU1-1
   30 N2=N2/2
      DO 40 K=1,N
      I=IBITR(K-1,NU)+1
      IF(I.LE.K)GO TO 40
      TREAL=XREAL(K)
      TIMAG=XIMAG(K)
      XREAL(K)=XREAL(I)
      XIMAG(K)=XIMAG(I)
      XREAL(I)=TREAL
      XIMAG(I)=TIMAG
```

```
40   CONTINUE
     RETURN
     END

     FUNCTION IBITR(J,NU)
     J1=J
     IBITR=0
     DO 10 I=1,NU
      J2=J1/2
      IBITR=IBITR*2+(J1-2*J2)
10   J1=J2
     RETURN
     END

     SUBROUTINE LPSB(MM,T,BW,A1,A2,BZERO)
C
C    SINE BUTTERWORTH LOW-PASS FILTER
C
C INPUT:
C    M : THE ORDER OF THE FILTER. 1 < M < 20
C        M = 6
C    T : SAMPLING INTERVAL
C    BW : CUTOFF FREQUENCY. 0 < BW < 1/2T
C
C OUTPUT:
C    A1 :
C    A2 :
C    BZERO :
C
C    Y(I) = -A1*Y(I-1)-A2*Y(I-2)+BZERO*X(I)
C
     REAL A1(11),A2(11)
     FACT=3.14159265*T*BW
     FACT=SIN(FACT)
     F=1.0
     M=MM
     M1=M/2
     M3=M1
     IF ( M1 .EQ. 0 ) GOTO 20
     M2=M
     A=M2
     SECTOR=3.14159265/A
     WEDGE=SECTOR/2.0
     DO 10 I=1,M1
     FN=I-1
```

```
      B=FACT*SIN(FN*SECTOR+WEDGE)
      C=1.0-FACT**2
      D=0.5*(-C+SQRT(C*C+4.0*B**2))
      E=SQRT(D+1.0)+SQRT(D)
      G=2.0*((2.0*B*B/D)-1.0)/(E**2)
      H=-1.0/(E**4)
      F=F*(1.0-G-H)
      A1(I)=-G
      A2(I)=-H
10    CONTINUE
20    IT=M-2*M1
      IF ( IT .EQ. 0 ) GOTO 30
      M3=M1+1
      A=FACT*FACT
      G=2.0*A+1.0-2.0*FACT*SQRT(A+1.0)
      A1(M3)=-G
      A2(M3)=0.0
      F=F*(1.0-G)
30    A=M3
      BZERO=F**(1.0/A)
      RETURN
      END

      SUBROUTINE LOWPASS(Z,BW,T,N)
      REAL Y0(11),Y1(11),A1(11),A2(11),Z(1)
C     INITIALIZATION OF THE FILTER
      M=6
      DO 10 I=1,11
      Y0(I)=0.0
      Y1(I)=0.0
10    M2=M-M/2
      CALL LPSB(M,T,BW,A1,A2,BZERO)
      DO 30 I=1,N
      Y0(1)=Z(I)
      DO 20 J=1,M2
      K1=J+1
      YI=BZERO*Y0(J)-A1(J)*Y0(K1)-A2(j)*Y1(K1)
      Y1(K1)=Y0(K1)
20    Y0(K1)=YI
30    Z(I)=YI
      RETURN
      END

      SUBROUTINE SMOOTH(GK,N,M)
      REAL PSD(1024),GK(N)
```

```
      K=(M-1)/2
      DO 5 I=1,K
      PSD(N-I+1)=GK(N-I+1)
5     PSD(I)=GK(I)
      DO 10 I=K+1,N-K
      PSD(I)=GK(I)/M
      DO 10 J=1,K
10    PSD(I)=PSD(I)+(GK(I-J)+GK(I+J))/M
      DO 20 I=1,N
20    GK(I)=PSD(I)
      RETURN
      END
```

APPENDIX II

MAIN PROGRAM FOR CALCULATING THE AUTO-SPECTRUM, CROSS-SPECTRUM, AND COHERENCE FUNCTION.

```
      PROGRAM DSP
      DIMENSION X1(512),Y1(512)
      DIMENSION AUTOX(1024),CROSSGK(1024),AUTOY(1024),COHER(1024)
      DIMENSION XREAL(2048),XIMAG(2048),YIMAG(2048),YREAL(2048)
      REAL NYQ
C
C     INPUT :
C
C              Z(I)   : SAMPLED FUNCTION
C              ND     : SAMPLE SIZE
C              N      : ANALYSIS SAMPLE SIZE
C              DX     : SAMPLING INTERVAL
C              M      : NUMBER OF FREQUENCY COMPONENTS USED TO
C                       SMOOTHING
C              PP     : THE RATIO OF THE CUT-OFF FREQUENCY TO
C                       NYQUEST FREQUENCY
C              CS     : CUTTING SPEED
C              IFL = 1 : SURFACE PROFILE
C              IFL = 2 : VIBRATION
C
C
C     OUTPUT :
C
C              AUTOX  : AUTO-SPECTRUM OF X
C              AUTOY  : AUTO-SPECTRUM OF Y
C              CROSS  : CROSS-SPECTRUM
C              COHER  : COHERENCE OF X AND Y
C
C
      OPEN(10,FILE='CROSS1')
      OPEN(11,FILE='CROSS2')
      OPEN(12,FILE='CROSS3')
      OPEN(13,FILE='AUTOX.DAT')
      OPEN(14,FILE='CROSS.DAT')
      OPEN(15,FILE='H.DAT')
      OPEN(16,FILE='COHER.DAT')
      OPEN(17,FILE='AUTOY.DAT')
```

```
      READ(10,*)DX,N,CS,PP,IFLAG
      DO 10 I=1,N
      READ(11,*)X1(I)
      READ(12,*)Y1(I)
10    CONTINUE
      IF (IFLG .EQ. 1) THEN
          T=DX*60.0/CS
      ELSEIF (ILFG .EQ. 2) THEN
          T=DX
      ENDIF
      NYQ=0.5/T
      CUT=NYQ*PP
      CALL PSD(X1,N,T,CUT,XREAL,XIMAG)
      DO 20 I=1,1024
      AUTOX(I)=2.0*(XREAL(I)**2+XIMAG(I)**2)/(T*1024*64)
20    CONTINUE
      CALL PSD(Y1,N,T,CUT,YREAL,YIMAG)
      DO 30 I=1,1024
      CROSSGK(I)=2.0*(XREAL(I)*YREAL(I)+XIMAG(I)*YIMAG(I))/
     & (T*1024*64)
      AUTOY(I)=2.0*(YREAL(I)**2+YIMAG(I)**2)/(T*1024*64)
      COHER(I)=CROSSGK(I)**2/(AUTOX(I)*AUTOY(I))
30    CONTINUE
      DO 80 I=1,1024
      FK=(I-1)/(T*2048)
      WRITE(13,*)FK,AUTOX(I)
      WRITE(14,*)FK,CROSSGK(I)
      WRITE(15,*)FK,AUTOY(I)/AUTOX(I)
      WRITE(16,*)FK,COHER(I)
      WRITE(17,*)FK,AUTOY(I)
80    CONTINUE
      CLOSE(10)
      CLOSE(11)
      CLOSE(12)
      STOP
      END
```

APPENDIX III

PROGRAM FOR CALCULATING THE KERF GEOMETRY

```
      PROGRAM JET
      REAL Z(101,61)
      INTEGER IPX,IPY
      OPEN (10,FILE='LEADING.DAT')
      OPEN (11,FILE='JET.DAT')
      ICX=1
      ICY=31
      R=0.5
      DX=0.025
      SCALE=10.0
      IPX=INT(R/DX)
      IPY=IPX
      DO 10 I=1,101
      DO 10 J=1,61
         Z(I,J)=0.0
10    CONTINUE
      CALL LEADING(Z,IPX,IPY,R,ICX,ICY)
      DO 20 J=1,61
      DO 20 I=1,101
20    WRITE(10,*)I,J,-Z(I,J)
      CLOSE (10)
         ICX1=ICX
         ICY1=ICY
      DO 30 IT=1,75
         ICX=ICX1+IT
         ICY=ICY1+INT(SCALE*SIN(6.2832*FLOAT(IT)/20.0))
30       CALL ZINC(Z,IPX,IPY,ICX,ICY,R,DX)
      DO 40 I=1,61
         DO 40 J=2,101
40        WRITE(11,*)J,I,-Z(J,I)
      CLOSE (11)
      STOP
      END

      SUBROUTINE LEADING(Z,IPX,IPY,R,ICX,ICY)
      REAL Z(101,61)
      DO 20 IY=ICY-IPY,ICY+IPY
         Y=R*FLOAT(ICY-IY)/FLOAT(IPY)
         IF (ABS(Y) .GT. R) THEN
          C0=0.0
```

```
      ELSE
       C0=SQRT(R*R-Y*Y)
      ENDIF
      IIX=ICX-IPX
      IF (IIX .LT. 1) THEN
       IIX=1
      ENDIF
      DO 10 IX=IIX,ICX+IPX
       X=R*FLOAT(IX-1)/FLOAT(IPX)
       IF ((C0-X) .LE. 0.0) THEN
        Z(IX,IY)=0.0
        GOTO 10
       ELSE
        C1=4.0*(150.*(C0-X))+1.0
        C2=SQRT(C1)
        Z(IX,IY)=(C2-1.0)*0.5
       ENDIF
10    CONTINUE
20  CONTINUE
    RETURN
    END

    SUBROUTINE ZINC(Z,IPX,IPY,ICX,ICY,R,DX)
    REAL Z(101,61)
    REAL DZ(101,61),R,DX
    INTEGER IPX,IPY,ICX,ICY
    DO 10 I=1,101
    DO 10 J=1,61
       DZ(I,J)=0.0
10  CONTINUE
    DO 30 IY=ICY-IPY+1,ICY+IPY
       Y=R*FLOAT(IY-ICY)/FLOAT(IPY)
       IIX=ICX-IPX
       IF (IIX .LT. 1) THEN
        IIX=1
       ENDIF
       DO 20 IX=IIX+1,ICX+IPX
        X=R*FLOAT(IX-ICX)/FLOAT(IPX)
        IF ((X*X+Y*Y-R*R) .GT. 0.00000) THEN
         DZ(IX,IY)=0.0
         GOTO 20
        ELSE
         DZ(IX,IY)=150.0*DX/(1+Z(IX,IY))
        ENDIF
        Z(IX,IY)=Z(IX,IY)+DZ(IX,IY)
```

```
20      CONTINUE
30    CONTINUE
      RETURN
      END
```

APPENDIX IV

PHOTOGRAPHS OF SAMPLES AND SURFACE PROFILE SPECTRA

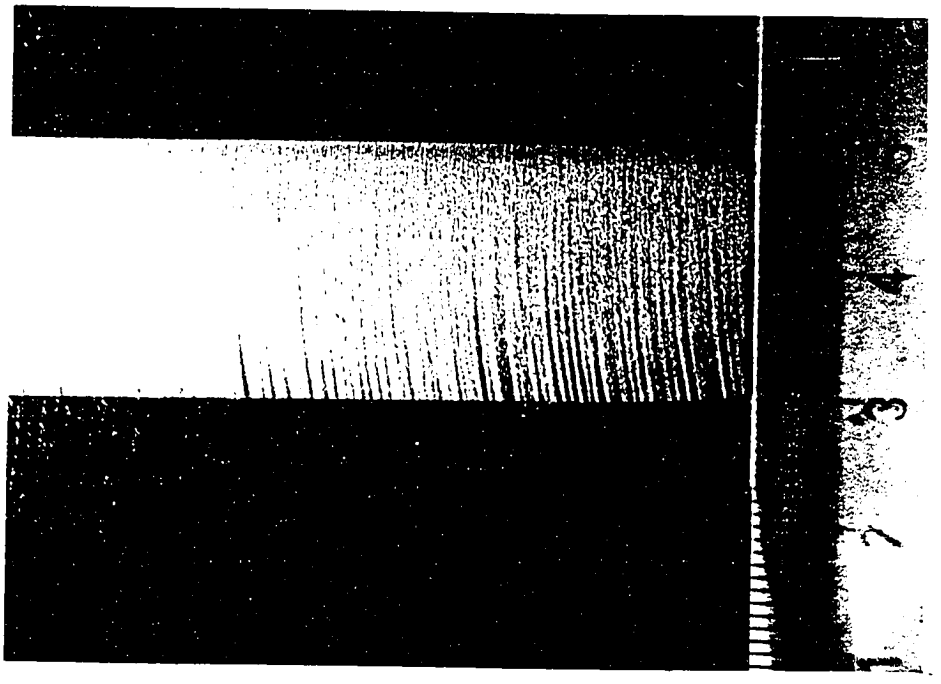

(a)

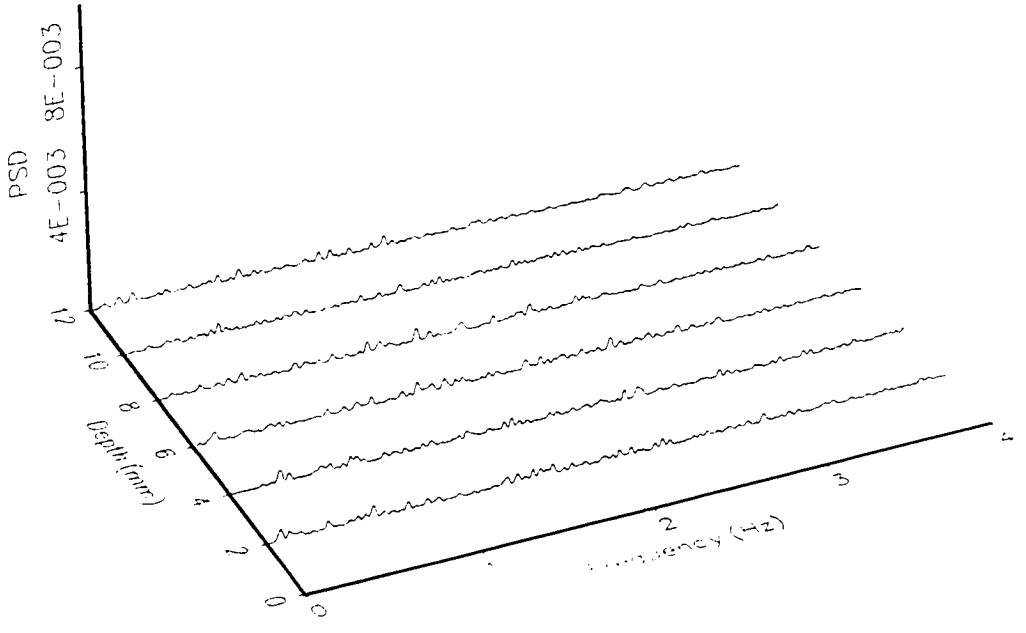

(b)

Figure A.1 (a) Photograph of the sample, and (b) power spectral densities profiles measured at different depths. (Titanium. F=60 mm/min., Ma=226g/min., Po=345MPa, Do=0.254mm, Dt=0.838mm, X-axis.)

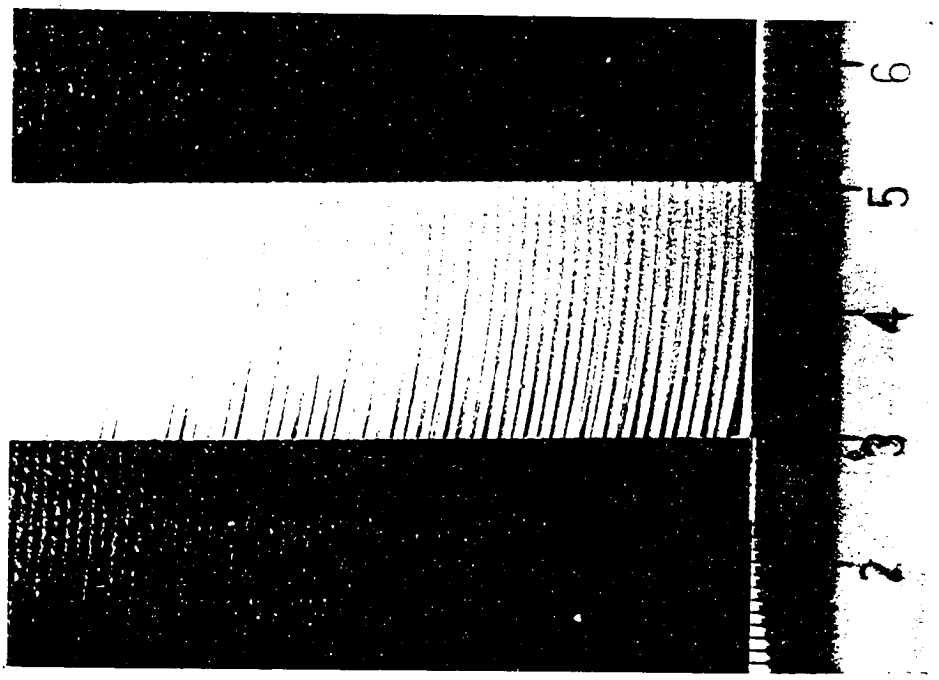

(a)

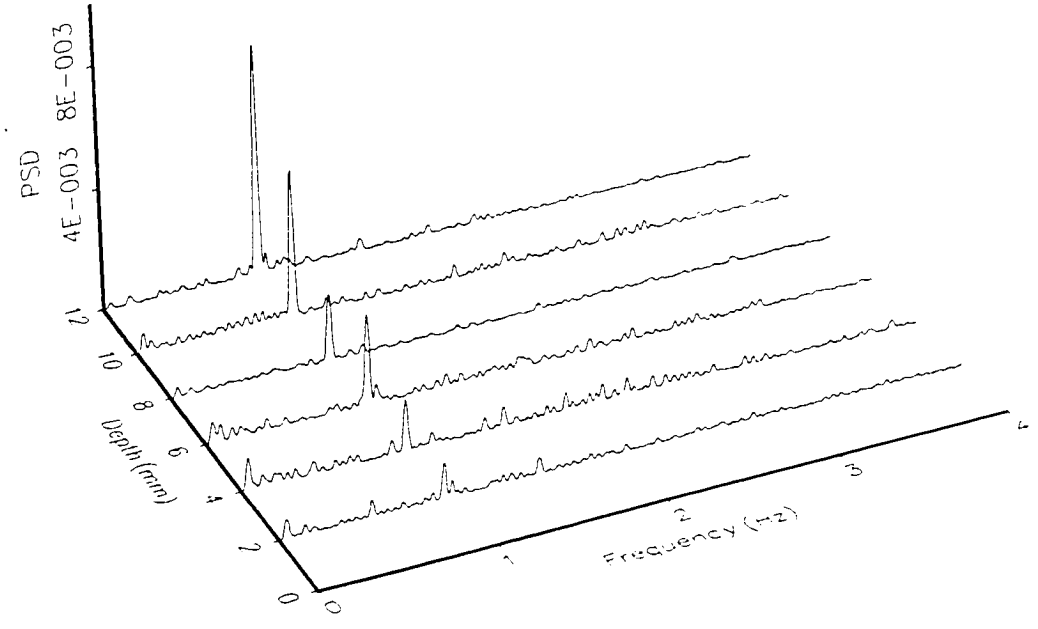

(b)

Figure A.2 (a) Photograph of the sample, and (b) power spectral densities profiles measured at different depths. (Titanium. F=60 mm/min., Ma=226g/min., Po=345MPa, Do=0.254mm, Dt=0.838mm, Y-axis.)

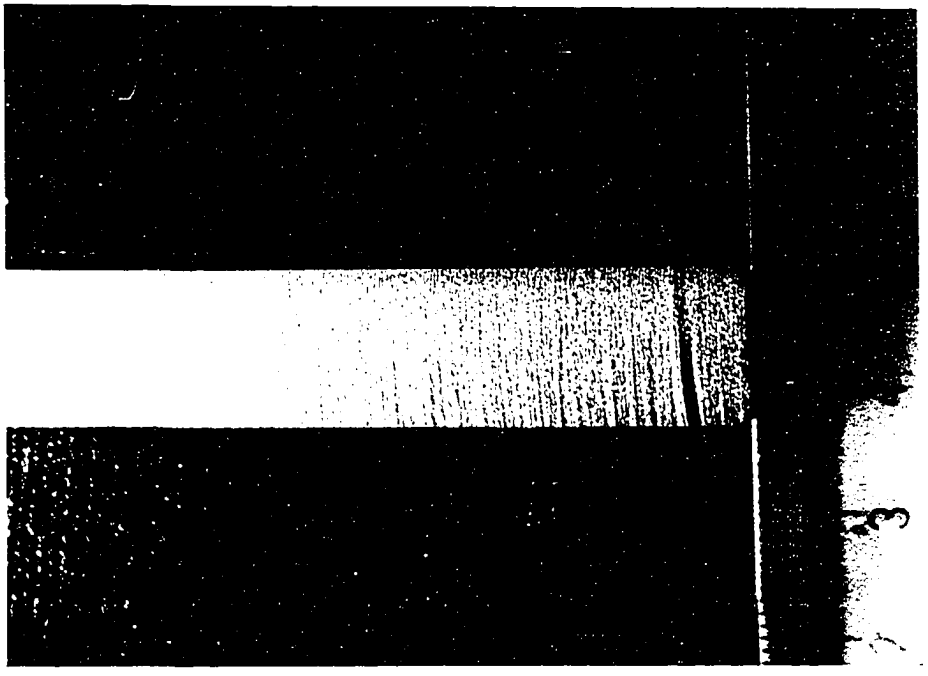

(a)

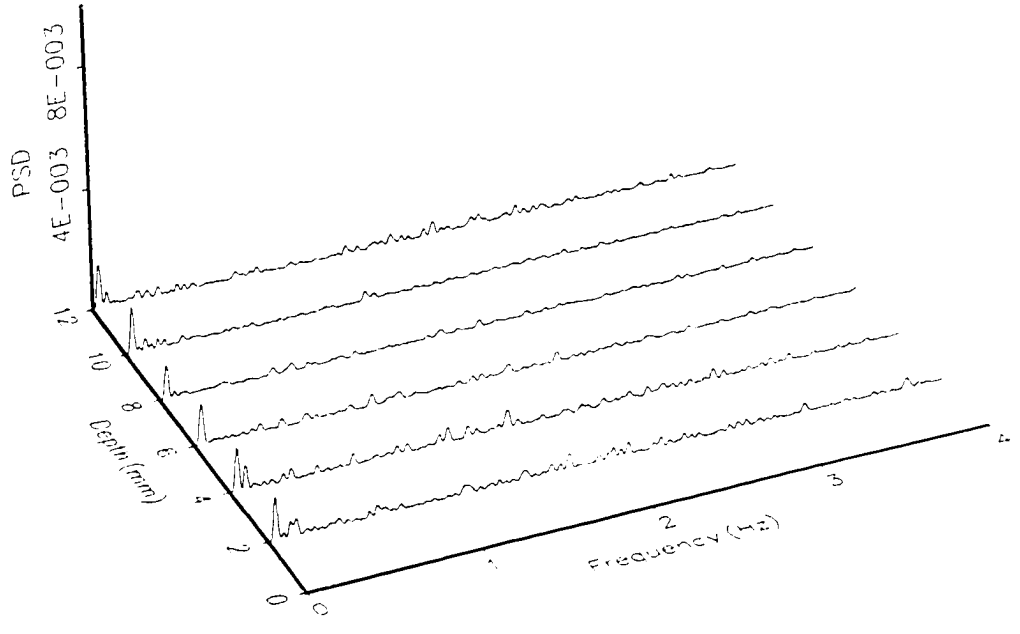

(b)

Figure A.3 (a) Photograph of the sample, and (b) power spectral densities measured at different depths. (Stainless steel. F=60 mm/min., Ma=226g/min., Po=345MPa, Do=0.254mm, Dt=0.838mm, X-axis.)

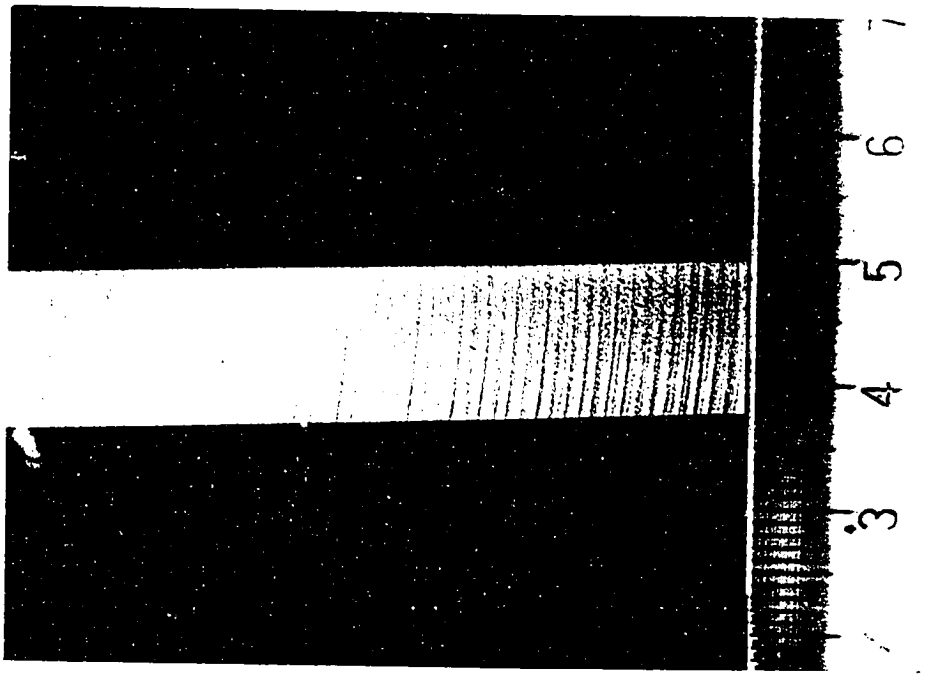

(a)

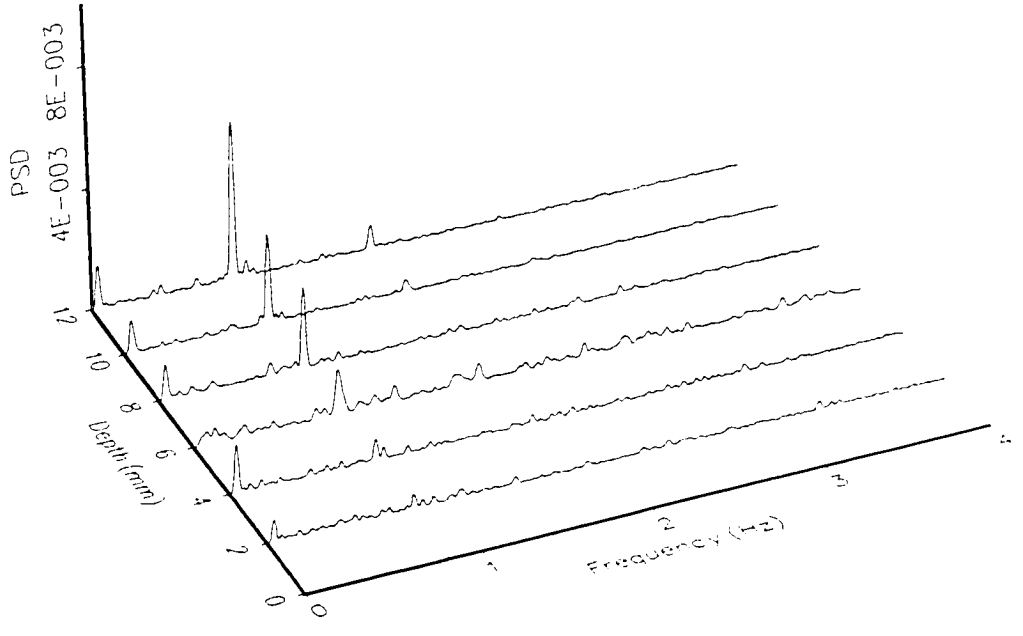

(b)

Figure A.4 (a) Photograph of the sample, and (b) power spectral densities measured at different depths. (Stainless steel. F=60 mm/min., Ma=226g/min., Po=345MPa, Do=0.254mm, Dt=0.838mm, Y-axis.)

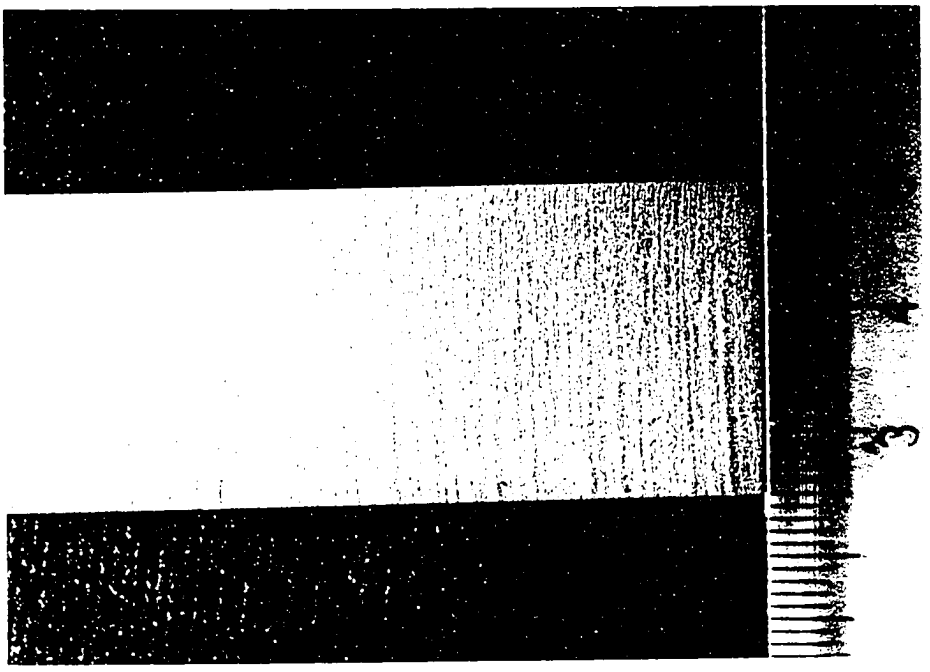

(a)

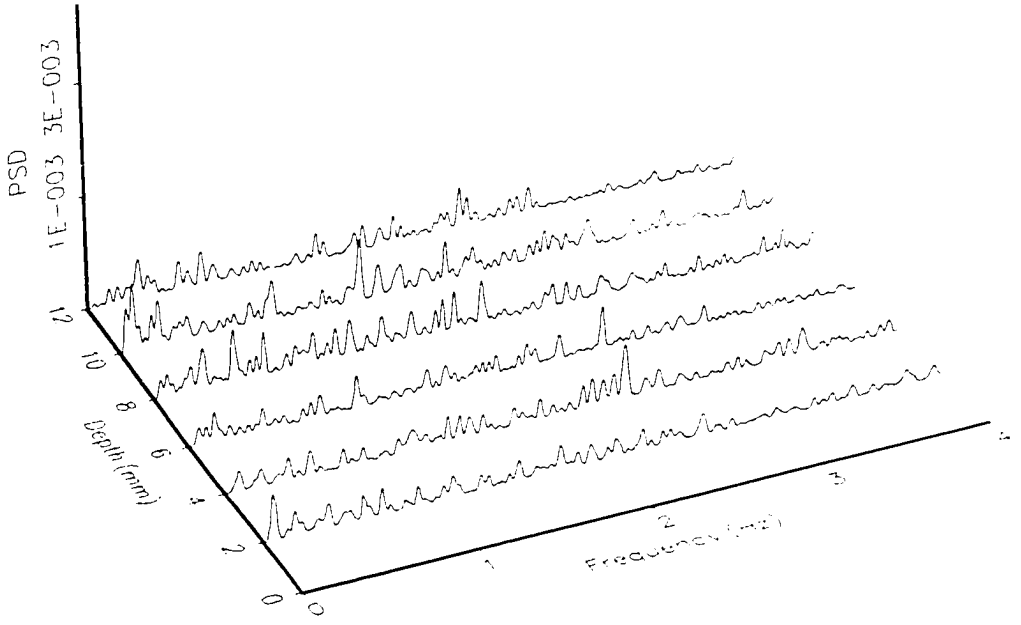

(b)

Figure A.5 (a) Photograph of the sample, and (b) power spectral densities measured at different depths. (Aluminum. F=60 mm/min., Ma=226g/min., Po=345MPa, Do=0.254mm, Dt=0.838mm, X-axis.)

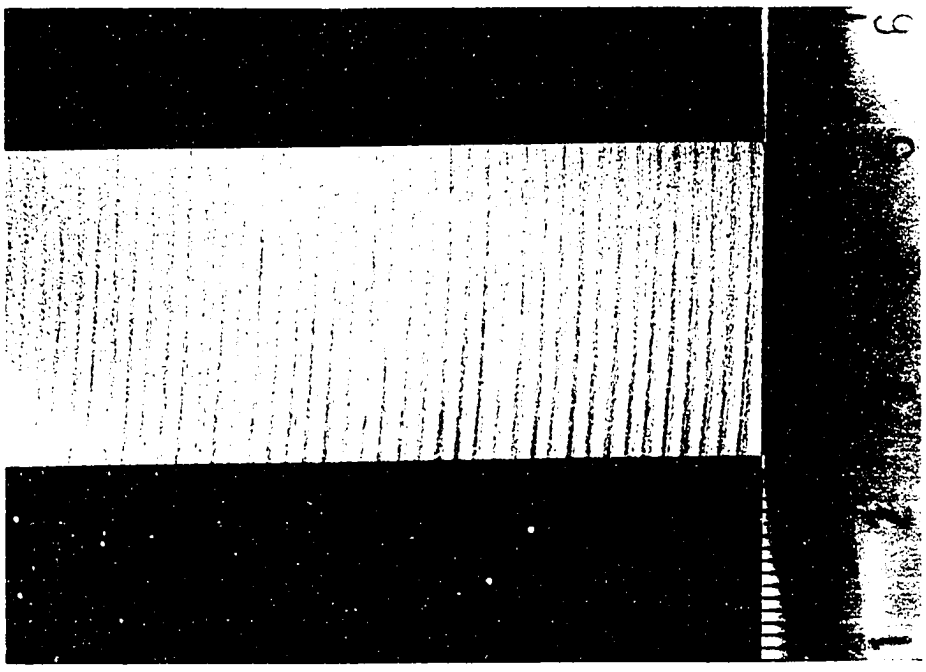

(a)

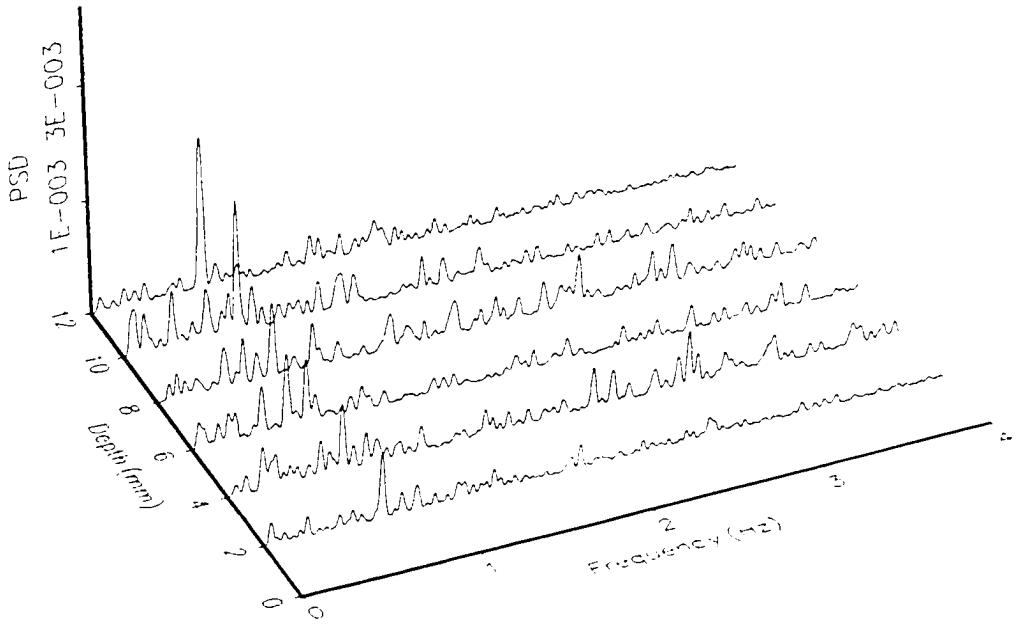

(b)

Figure A.6 (a) Photograph of the sample, and (b) power spectral densities measured at different depths. (Aluminum. F=60 mm/min., Ma=226g/min., Po=345MPa, Do=0.254mm, Dt=0.838mm, Y-axis.)

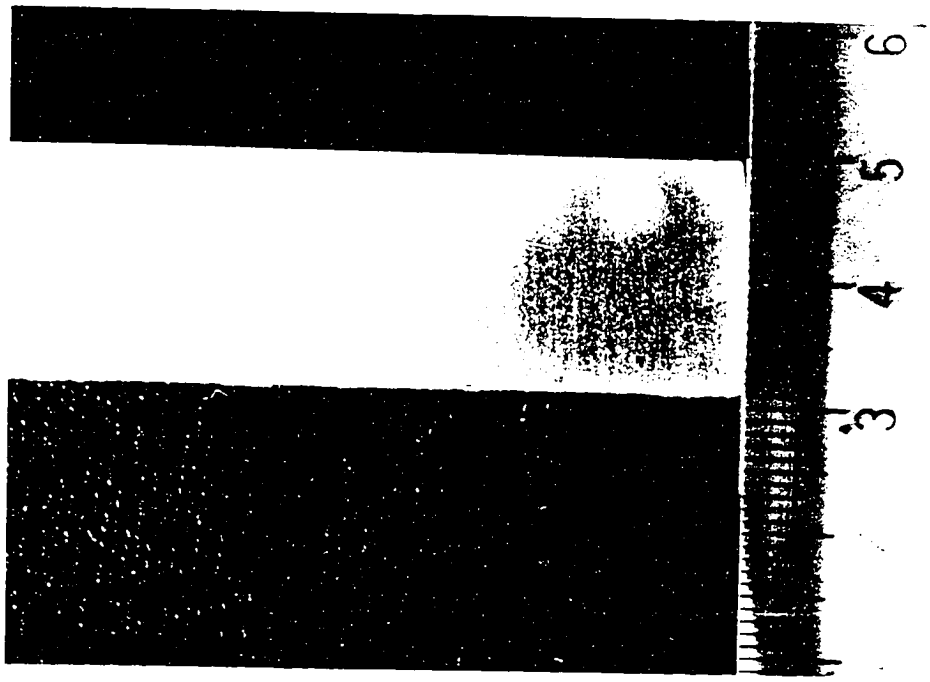

(a)

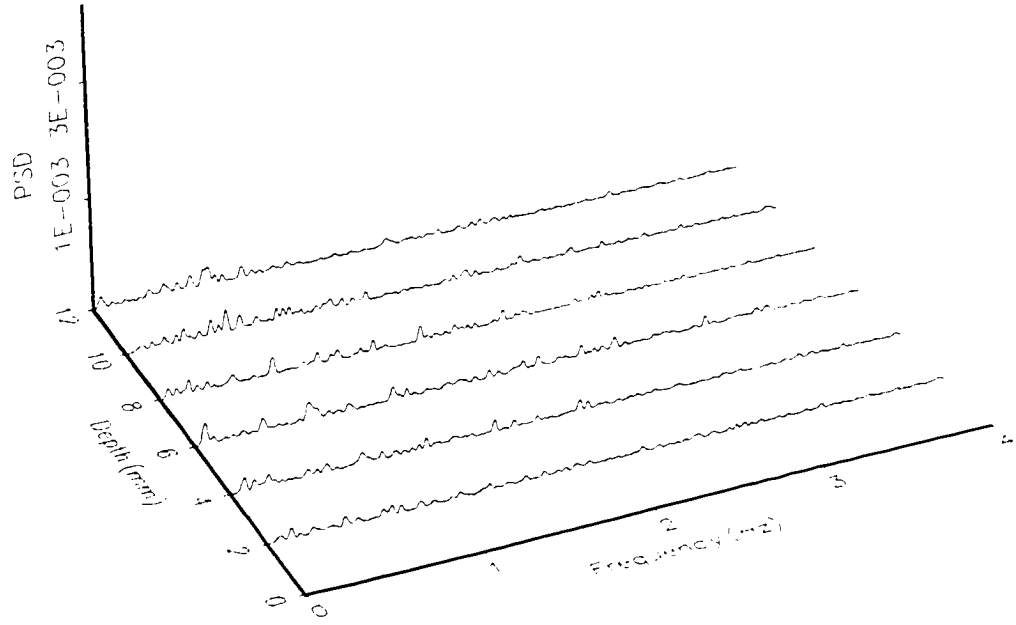

(b)

Figure A.7 (a) Photograph of the sample, and (b) power spectral densities measured at different depths. (Glass. F=60 mm/min., Ma=226g/min., Po=345MPa, Do=0.254mm, Dt=0.838mm, X-axis.)

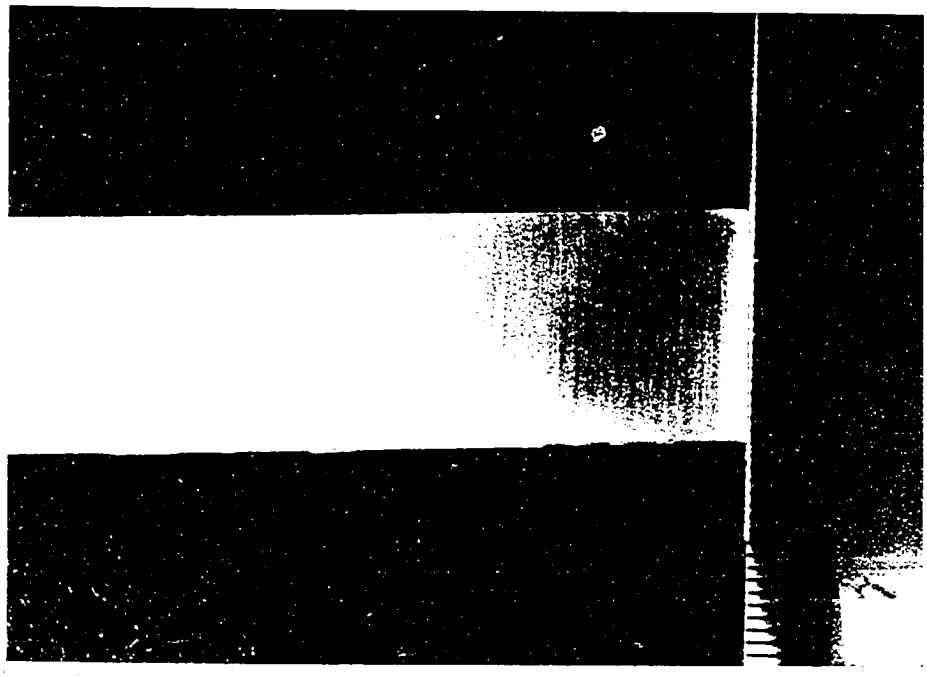

(a)

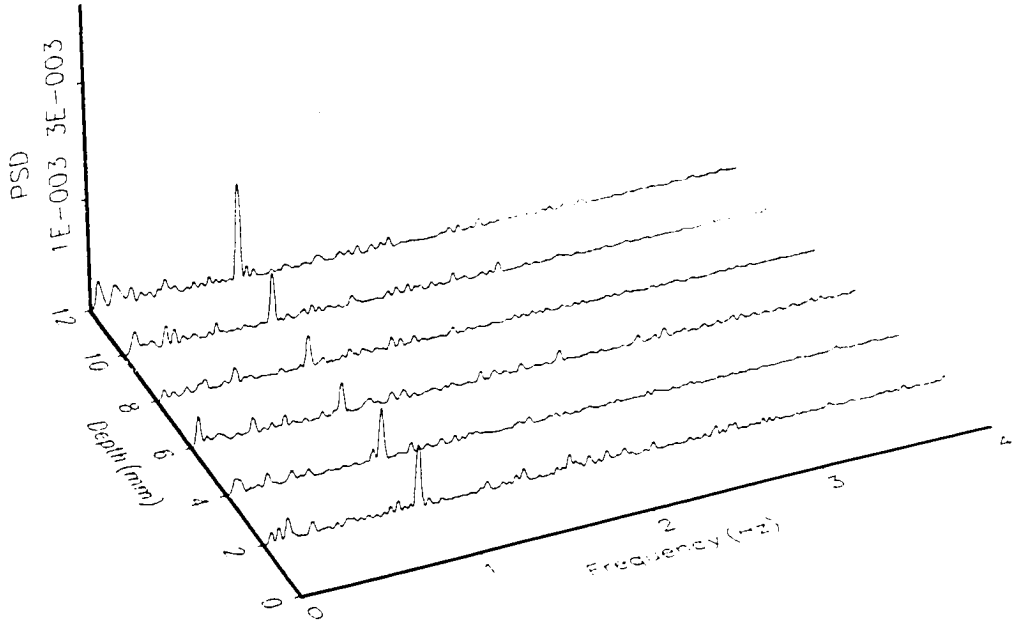

(b)

Figure A.8 (a) Photograph of the sample, and (b) power spectral densities measured at different depths. (Glass. F=60 mm/min., Ma=226g/min., Po=345MPa, Do=0.254mm, Dt=0.838mm, Y-axis.)

WORKS CITED

1. Blickwedel, H., N. S. Guo, H. Haferkampf, and H. Louis. "Prediction of Abrasive Jet Cutting Efficiency and Quality." *Proceedings of the 10th. Int. Symp. on Jet Cutting Technology*, Amsterdam (1990).

2. Hunt, C. D., T. J. Kim, and M. Reuber. "Surface Finish Optimization for Abrasive Waterjet Cutting." *Proceedings of the 9th. Int. Symp. on Jet Cutting Technology*, Sendai, Japan (1988).

3. Matsui, S., H. Matsumura, Y. Ikemoto, K. Tsujita, and H. Shimizu. "High Precision Cutting Method for Metallic Materials by Abrasive Waterjet." *Proceedings of the 10th. Int. Symp. on Jet Cutting Technology,* Amsterdam (1990) Paper No. G3.

4. Souda, V. *Implementation of an Integrated High Energy Beam Workcell.* Master Thesis, New Jersey Institute of Technology, Newark, NJ (1990).

5. Zhou, G., M. Leu, E. Geskin, Y. Chung, and J. Chao. "Investigation of Topography of Waterjet Generated Surfaces." *Proceedings of ASME Winter Annual Meeting,* LA (1992).

6. Hashish, M. "A Model Study of Metal Cutting With Abrasive Waterjets." *ASME Journal of Engineering Materials and Technology*, 106 (1984): 88-100.

7. Hashish, M. "Visualization of the Abrasive-Waterjet Cutting Process." *Experimental Mechanics,* (1988): 159-169.

8. Tan, D. K. M. "A Model for the Surface Finish in Abrasive Waterjet Cutting." Proceedings of the 8th. Int. Symp. on Jet Cutting Technology, Durham (1986): 309-313.

9. Hashish, M. "Characteristics of Surfaces Machined With Abrasive-Waterjets." *ASME Journal of Engineering Materials and Technology*, 113 (1991): 354-362.

10. Arata, Y., H. Maruo, I. Miyamoto, and S. Takeuchi. "Dynamic Behavior in Laser Gas Cutting of Mild Steel." *Trans. JWSI*, Vol. 8, No. 8 (1979): 15-26.

11. Powell, J., T. G. King, and I. A. Menzies. "Cut Edge Quality Improvement by Laser Pulsing." *Proceedings of the 2nd. Int. Conf. on Lasers in Manufacturing*, Birmingham (1985): 37-45.

12. Powell, J., T. G. King, I. A. Menzies, and K. Frass. "Optimization of Pulsed Laser Cutting of Mild Steels." *Proceedings of the 3rd. Int. Conf. on Lasers in Manufacturing*, Paris (1986): 67-75.

13. Olsen, F. O. "Cutting Front Formation in Laser Cutting." *Annals of CIRP*, 38/1 (1989): 215-218.

14. Finnie, I. "The Mechanism of Erosion of Ductile Metals." *Proceedings of the 3rd. National Congress of Applied Mechanics*, (1958): 527-532.

15. Bitter, J. G. A. "A Study of Erosion Phenomena - Part I." *Wear*, 6 (1963): 5-21.

16. Bitter, J. G. A. "A Study of Erosion Phenomena - Part II." *Wear*, 6 (1963): 169-190.

17. Hashish, M. "On the Modeling of Abrasive Waterjets Cutting." *Proceedings of the 7th. Int. Symp. on Jet Cutting Technology*, (1984).

18. Hashish, M. "A Model for Abrasive-Waterjet (AWJ) Machining." *ASME Journal of Engineering Materials and Technology*, 111 (1989): 154-162.

19. Hashish, M. "On the Modeling of Surface Waviness Produced by Abrasive-Waterjets." *Proceedings of the 11th. Int. Symp. on Jet Cutting Technology*, London (1992): 17-34.

20. Hunt, C. D., C. D. Burnham, and T. J. Kim. "Surface Finish Characterization in Machining Advanced Ceramics by Abrasive Waterjet." *Proceedings of the 4th. American Water Jet Conference*, (1987).

21. Burnham, C. D., and T. J. Kim. "Statistical Characterization of Surface Finish Produced by Abrasive Waterjet." *Proceedings of the 5th. American Water Jet Conference*, (1989).

22. ElMaraghy, H. A., and B. Johnson. "An Investigation Into the Compliance of SCARA Robots. Part II: Experimental and Numerical Validation." *ASME Journal of Dynamic Systems, Measurement, and Control*, 110 (1988): 23-30.

23. Bendat, J. S., and A. G. Piersol. *Random Data: Analysis and Measurement Procedures*. New York: John Wiley & Sons Inc. (1971).

24. Ewins, D. J. *Modal Testing: Theory and Practice*. New York: John Wiley & Sons Inc. (1984).

25. Ber, A., and S. Braun. "Spectral Analysis of Surface Finish." *Annals of the CIRP*. 16 (1968): 53-59.

26. Marple, S. L. *Digital Spectral Analysis: With Applications.* Englewood Cliffs, New Jersey: Prentice-Hall, (1987).

27. Pandit, S. M., and S. M. Wu. *Time Series and System Analysis With Applications.* New York: John Wiley & Sons Inc. (1983).

28. DeVor, R. E., and S. M. Wu. "Surface Profile Characterization by Autoregressive-Moving Average Models." *ASME Journal of Engineering for Industry*, (1972): 825-832.

29. Schwarz, G. "Estimating the Dimension of a Model." *The Annals of Statistics*, Vol. 6. No. 2 (1978): 461-464.

30. Zeng, J., R. Heines, and T. Kim. "Characterization of Energy Dissipation Phenomenon in Abrasive Waterjet Cutting." *Proceedings of the 6th. American Water Jet Conference*, Houston (1991): 163-177.

31. Nadeau, E., G. D. Stubley, and D. J. Burns. "Prediction and Role of Abrasive Velocity in Abrasive Water Jet Cutting." *International Journal of Water Jet Technology*, Vol. 1, No. 3 (1991): 109-116.

32. Himmelreich, U., and W. Riess. "Laser-Velocimetry Investigations of the Flow in Abrasive Water Jets with Varying Cutting Head Geometry." *Proceedings of the 6th. American Water Jet Conference*, Houston (1991): 355-369.

33. Chen, W., and E. S. Geskin. "Correlation Between Particle Velocity and Conditions of Abrasive Waterjet Formation." *Proceedings of the 6th. American Water Jet Conference*, Houston (1991): 305-313.

34. Miller, A. L., and J. H. Archibald. "Measurement of Particle Velocities in an Abrasive Jet Cutting System." *Proceedings of the 6th. American Water Jet Conference, Houston* (1991): 291-304.

35. Neusen, K. F., T. J. Gores, and T. J. Labus. "Measurement of Particle and Drop Velocities in a Mixed Abrasive Water Jet Using a Forward-Scatter LDV System." *Proceedings of the 11th. Int. Symp. on Jet Cutting Technology*, London (1992): 63-73.

36. Capello, E., and R. Groppetti. "On an Energetic Semi-empirical Model of Hydro-abrasive Jet Material Removal Mechanism for Control and Optimization." *Proceedings of the 11th. Int. Symp. on Jet Cutting Technology*, London (1992): 101-120.

37. Corcoran, M., M. Mazurkiewicz, and P. Karlic. "Computer Simulation of an Abrasive Waterjet Cutting Process." *Proceedings of the 9th. Int. Symp. on Jet Cutting Technology*, Sendai, Japan, Paper B1. (1988).

38. Chung, Y. *Development of Prediction Technique for the Geometry of the Abrasive Waterjet Generated Kerf.* Ph. D. Dissertation, New Jersey Institute of Technology, Newark, NJ, (1992).

39. Kovacevic, R. "Surface Texture in Abrasive Waterjet Cutting." *Journal for Manufacturing Systems*, Vol. 10, No. 1 (1991): 32-40.

40. Matsui, S., H. Matsumura, Y. Ikemoto, Y. Kumon, and H. Shimizu. "Prediction Equations for Depth of Cut Made by Abrasive Waterjet." *Proceedings of the 6th. American Water Jet Conference*, Houston (1991): 31-41.

41. Burnham, C. D., and T. J. Kim. " Statistical Characterization of Surface Finish Produced by a High Pressure Abrasive Waterjet." *Proceedings of the 6th. American Water Jet Conference*, Toronto, Canada (1989): 165-175.

42. Zeng, J., and T. J. Kim. "Development of an Abrasive Waterjet Kerf Cutting Model for Brittle Materials." *Proceedings of the 9th. Int. Symp. on Jet Cutting Technology*, London (1992): 483-501.

43. Geskin, E. S., W. L. Chen, S. S. Chen, F. Hu, M. E. U. Khan, S. Kim, P. Singh, and P. Ferguson. "Investigation of Anatomy of Abrasive Waterjet." *Proceedings of the 5th. American Water Jet Conference*, Toronto (1989): 217-231.

44. Neilson, J. H., and A. Gilchrist. "Erosion by a Stream of Solid Particles." *Wear*, Vol. 11 (1968): 111-122.

45. Hu, F., Y. Yang, E. S. Geskin, and Y. Chung. "Characterization of Material Removal in the Course of Abrasive Waterjet Machining." Proceedings of the 6th. American Water Jet Conference, Houston (1991): 17-29.